Remote Sensing and Modeling of Stressed Aquifer Systems and the Associated Hazards

by

Megan Marie Miller

A Dissertation Presented in Partial Fulfillment
of the Requirements for the Degree
Doctor of Philosophy

Approved April 2018 by the
Graduate Supervisory Committee:

Manoochehr Shirzaei, Chair
Stephen Reynolds
James Tyburczy
Steven Semken
Susanna Werth

ARIZONA STATE UNIVERSITY

August 2018

ABSTRACT

Aquifers host the largest accessible freshwater resource in the world. However, groundwater reserves are declining in many places. Often coincident with drought, high extraction rates and inadequate replenishment result in groundwater overdraft and permanent land subsidence. Land subsidence is the cause of aquifer storage capacity reduction, altered topographic gradients which can exacerbate floods, and differential displacement that can lead to earth fissures and infrastructure damage. Improving understanding of the sources and mechanisms driving aquifer deformation is important for resource management planning and hazard mitigation.

Poroelastic theory describes the coupling of differential stress, strain, and pore pressure, which are modulated by material properties. To model these relationships, displacement time series are estimated via satellite interferometry and hydraulic head levels from observation wells provide an in-situ dataset. In combination, the deconstruction and isolation of selected time-frequency components allow for estimating aquifer parameters, including the elastic and inelastic storage coefficients, compaction time constants, and vertical hydraulic conductivity. Together these parameters describe the storage response of an aquifer system to changes in hydraulic head and surface elevation. Understanding aquifer parameters is useful for the ongoing management of groundwater resources.

Case studies in Phoenix and Tucson, Arizona, focus on land subsidence from groundwater withdrawal as well as distinct responses to artificial recharge efforts. In Christchurch, New Zealand, possible changes to aquifer properties due to earthquakes are investigated. In Houston, Texas, flood severity during Hurricane Harvey is linked to subsidence, which modifies base flood elevations and topographic gradients.

DEDICATION

This dissertation is dedicated to my parents, Carol & Craig Miller, and my 'Academic Father' and mentor, Manoochehr Shirzaei. Thank you for believing in me.

ACKNOWLEDGMENTS

This work is funded by the National Science Foundation (NSF) and National Aeronautics and Space Administration (NASA).

The following opus is possible because of the invaluable support, encouragement, and collaboration of the following people: The Remote Sensing and Tectonic Geodesy Lab (RaTLab): Dr. Manoochehr Shirzaei (graduate advisor and dissertation committee chair), Guang Zhai, Mostafa Parham Khoshmanesh, Dr. Jennifer Weston-Roebuck, Zac Yung-Chun Liu, Dr. Chandrakanta Ojha, and Grace Carlson. My dissertation committee members: Stephen Reynolds, Steven Semken, Jim Tyburczy, Susanna Werth, and exam committee member, Dan Shim. My co-author, collaborator Donald Argus at JPL. Arizona Department of Water Resources (ADWR), Arizona Geological Survey (AZGS) and Arizona Land Subsidence Group (AzLSG), especially Brain Conway for welcoming me into the community. Simon Cox at GNS Science for advising the EAPSI project, showing me the South Island, and taking me to the Follow-Me Ski School. Phil and Clair Scadden for having me in their beautiful Dunedin home.

Of course, all my friends from SESE, rock climbing, trail running, and my housemates: Heather Meyer, Julie Mitchell, Alli Severson, Taisiya Kopytova, Alana Williams and Lucia Perez, Jeff Smith and Ashley Jenkins, the Goon Squad.

Finally, thank you, Mom, for fostering my interest in science, Dad, for helping me with my math homework, and my generous hardworking sister, Carolyn!

TABLE OF CONTENTS

CHAPTER Page

LIST OF TABLES

Table Page

LIST OF FIGURES

Figure Page

Figure Page

CHAPTER 1: INTRODUCTION

1.1. Overview

Freshwater availability is increasingly important as the climate changes and global population increases [*Vörösmarty et al.*, 2000]. The world's largest accessible freshwater resource is hosted by aquifers; however, groundwater reserves are declining in many places causing decreased well yields, increased pumping costs, and diminishing water quality [*Konikow and Kendy*, 2005]. Groundwater overdraft occurs when water removed is not replenished in an aquifer system. Many regions are threatened by a changing climate, which can exacerbate overdraft in drought scenarios when surface water is scarce, accelerating depletion of the groundwater supply [*Aeschbach-Hertig and Gleeson*, 2012]. Groundwater exploitation can also lead to irreversible land subsidence and altered topography [*Poland and Davis*, 1969].

The surface of the earth deforms due to stresses stemming from natural and/or anthropogenic forces. Subtle, widespread surface deformation occurs when large volumes of fluid are withdrawn from or reintroduced to underground reservoir systems [*Fielding et al.*, 1998; *Holzer and Galloway*, 2005]. Land subsidence, in particular, is documented in a growing number of cities throughout the United States including: Houston-Galveston, Texas [*Holzer*, 1981], southern New Jersey [*Sun et al.*, 1999], the San Joaquin Valley, California [*Holzer and Galloway*, 2005], the Antelope Valley, California [*Galloway et al.*, 1998], and the Santa Clara Valley, California [*Schmidt and Bürgmann*, 2003]. The arid southwestern United States is especially susceptible to subsidence with notable examples in Las Vegas, Nevada [*Amelung et al.*, 1999], Phoenix, Arizona [*Casu et al.*, 2005; *Galloway and Burbey*, 2011] and Tucson, Arizona [*Carruth et al.*, 2005; *Kim et al.*, 2015].

1.2. Aquifer System and Poroelastic Primer

Aquifer system deformation is governed by the principle of effective stress, σ', which is the foundation of the coupled relationship of changes in hydraulic head levels and deformation in one dimension (Equation 1.1) [*K. Terzaghi*, 1925].

$$\sigma' = \sigma - p \tag{1.1}$$

where σ is total overburden stress and p is pore pressure. Assuming constant overburden stress, changes in pore pressure Δp and hydraulic head Δh are related by: [*Poland and Davis*, 1969]

$$\Delta p = -\Delta\sigma' = \Delta h \rho_w g \tag{1.2}$$

Where ρ_w is the density of water, g is gravitational acceleration and $\Delta\sigma'$is the change in effective stress. The equation for aquifer compressibility α includes vertical deformation, given by:

$$\alpha = -\frac{\Delta b}{\Delta\sigma' b_o} = \frac{\Delta b}{\Delta h \rho_w g b_o} \tag{1.3}$$

where Δb is compaction and b_o is initial thickness [*Jacob*, 1940]. Specific storage of a confined aquifer, S_s, is the amount of water produced as pore pressure declines, as the aquifer system compresses, and water expands [*Theis*, 1935; *Jacob*, 1940; *Burbey*, 2001a];

$$S_s = \rho_w g(\alpha + n\beta) \tag{1.4}$$

Where β is water compressibility and n is porosity. By incorporating Equation (1.4) with Equation (1.3) and assuming water compressibility β is negligible relative to aquifer system deformation:

$$S_k = S_s b_o = \frac{\Delta b}{\Delta h} \tag{1.5}$$

The storage coefficient S_k, which is dimensionless, describes the volume of fluid released from an aquifer system area with a change in hydraulic head level. At the surface, the poroelastic response to groundwater withdrawal is detected as depression of the land surface, either elastic/recoverable or inelastic/permanent [*Poland and Ireland*, 1988]. The skeletal storage can be separated into elastic S_{ke} and inelastic S_{kv} skeletal storage coefficients based on whether effective stress is greater than a pre-consolidation stress σ'_{max} threshold [*Hoffmann et al.*, 2003b]:

$$S_k = S_{ke} + S_{kv},$$

$$S_k = \begin{cases} S_{ke} \text{ for } \sigma' < \sigma'_{max} \\ S_{kv} \text{ for } \sigma' \geq \sigma'_{max} \end{cases} \tag{1.6}$$

The dimensionless elastic storage coefficient S_{ke} represents the elastic behavior of both the aquifer and aquitard units [*Hoffmann et al.*, 2001; *Liu and Helm*, 2008]. It is an important parameter for groundwater flow models [*Riley*, 1969; *Green and Wang*, 1990] and describes the volume of fluid removed or retained as the hydraulic head levels fluctuate.

$$S_{ke} = \frac{\Delta b_p}{\Delta h_p} \tag{1.7}$$

where Δb_P and Δh_P are the elastic, seasonal components of the vertical displacement and water level time series, respectively. The dimensionless inelastic skeletal storage coefficient S_{kv} describes the volume of fluid slowly expelled due to permanent compaction of an aquitard volume [*Hoffmann et al.*, 2003a]. The temporal lag is described by a compaction time constant, τ, which represents delayed equilibration of aquitard head levels to neighboring aquifer head levels;

$$\frac{\Delta b_l}{\Delta h_l} = S_{kv}\left(1 - \frac{8}{\pi^2} e^{\frac{-\pi^2 t}{4\tau}}\right) \tag{1.8}$$

where Δb_l and Δh_l are the inelastic, long-term vertical surface deformation and hydraulic head level time series. The inelastic skeletal storage coefficient can be several orders of magnitude greater than the elastic storage coefficient [*Burbey*, 2001b].

Slow draining aquitard materials and residual compaction are characterized by modeling the vertical deformation time series Δb as an exponential function of time, t [*K. Terzaghi*, 1925; *Buisman*, 1936; *Chaussard et al.*, 2014];

$$\Delta b = M(e^{(Bt)}-1) \tag{1.9}$$

where M is the coefficient of the magnitude of aquifer response (subsidence $M>0$, uplift $M<0$) and B is the coefficient of decay [-1,0]. If pore pressure is regained by natural or artificial aquifer recharge, a similar exponential decay pattern in the elastic relaxation of the matrix can occur and result in uplift; this is referred to as poroelastic rebound [*Amelung et al.*, 1999; *Schmidt and Bürgmann*, 2003]. Aquifer parameters and coefficient values describe coupled aquifer system responses to changes in head levels and surface topography. To understand and model system behavior and porous medium flow, defining aquifer parameters is a priority.

1.3 Organization

Subtle surface deformation is difficult to detect. Various, often complementary, geodetic techniques are used to measure deformation at a range of temporal and spatial scales. Geodetic leveling surveys provide highly accurate and precise measurements of localized areas by comparing the height difference between two points [*Dokka*, 2006]. Global Positioning System (GPS) stations offer nearly continuous temporal data at selected points [*Mossop and Segall*, 1997]. Interferometric Synthetic Aperture Radar (InSAR) covers a broad area at repeated intervals [*Ferretti et al.*, 2000; *Dixon et al.*, 2006]. To provide a robust evaluation, a multi-disciplinary approach is advantageous, including in situ, remote sensing, and field observations.

In this dissertation, five projects related to anthropogenic and natural surface deformation of aquifer systems are presented:

1) Land subsidence occurrences in Phoenix, Arizona, where InSAR is used to investigate ground displacement time series from 1992-2010. Three zones of subsidence with unique deformation patterns and characteristics, as well as a broad uplift zone coinciding with recharge well locations are identified. Observation wells provide an in situ, independent dataset of hydraulic head level time series. Continuous wavelet transform is implemented to isolate long-term and seasonal trends for aquifer parameter estimation. Deformation and well level time series are used to estimate elastic storativity, inelastic storativity, and the compaction time constant. These parameters describe the storage response of the aquifer system.

2) Time series of volumetric strain is modeled in the subsidence zones of the Phoenix, Arizona aquifer system. An inversion is constrained with the line-of-sight interferometric displacement time series from 2004-2010, solving for deforming triangular prism volumes from the surface to a depth of 900m. Within each prism, volume strain is assumed constant and due only to vertical deformation of a horizontal plane, buried in a homogenous, isotropic elastic half-space. The model is used to solve for the stress tensor near the surface. The ratio of minimum principal stress and tensile strength of the aquifer material is used to identify locations where earth fissures are likely to form.

3) Aquifer overdraft also causes subsidence in Tucson, Arizona, where groundwater is a critical water resource. From 1990 to 2015, long time series of surface deformation are generated from InSAR and extensometer/well sites, validated by GPS. Aquifer parameters

are estimated, including elastic storativity, inelastic storativity, and the compaction time constant as with Phoenix, as well as vertical hydraulic conductivity. Recharge efforts have slowed subsidence to a near halt, likely reducing hazards associated with earth fissuring and infrastructure damage.

4) The 2010 to 2011 Canterbury earthquake sequence in Christchurch, New Zealand, caused unprecedented liquefaction and unusual groundwater fluctuations. Groundwater systems exhibit complex responses to static and dynamic stresses associated with earthquakes. Poroelastic theory describes the coupling of differential stress, strain, and pore pressure, which are modulated by material properties, including the elastic storage coefficient. Elastic storativity is estimated by comparing seasonal vertical deformation data and hydraulic head levels. This study explores possible changes to aquifer properties because of the earthquake sequence.

5) Following rapid intensification, Hurricane Harvey stalled over Texas and caused a rare, 9000-year extreme precipitation event in August 2017. The spatial extent of flooding due to the cyclone is observed through analysis of backscatter properties of satellite radar imagery. Also, coastal flooding due to storm tide is modeled on a high-resolution Light Detection and Ranging (LIDAR) digital elevation model (DEM). Land subsidence is detected for the years preceding the cyclone using InSAR and a chi-squares goodness of fit test to determine the significance of the correlation between flooded and subsiding areas. Scenarios of future coastal flood patterns by 2100 are explored using projections of sea level rise, continued subsidence, and storms.

CHAPTER 2: SPATIOTEMPORAL CHARACTERIZATION OF SUBSIDENCE AND UPLIFT IN PHOENIX USING INSAR TIME SERIES AND WAVELET TRANSFORMS

Abstract: The effects of land subsidence pose a significant hazard to the environment and infrastructure in the arid, alluvial basins of Phoenix, Arizona. Improving our understanding of the source and mechanisms of subsidence is important for planning and risk management. Here we employ multitemporal interferometric analysis of large synthetic aperture radar data sets acquired by ERS and Envisat satellites to investigate ground deformation. The ERS data sets from 1992 to 1996 and Envisat, 2003–2010, are used to generate line of sight (LOS) time series and velocities in both the ascending and descending tracks. The general deformation pattern is consistent among data sets and is characterized by three zones of subsidence and a broad zone of uplift. The multitrack Envisat LOS time series of surface deformation are inverted to obtain spatiotemporal maps of the vertical and horizontal deformation fields. We use observation wells to provide an in situ, independent data set of hydraulic head levels. Then we analyze vertical interferometric synthetic aperture radar and hydraulic head level time series using continuous wavelet transform to separate periodic signal components and the long-term trend. The isolated signal components are used to estimate the elastic storage coefficient, the inelastic skeletal storage coefficient, and compaction time constants. Together these parameters describe the storage response of an aquifer system to changes in hydraulic head and surface elevation. Understanding aquifer parameters is useful for the ongoing management of groundwater resources.

2.1 Background

The Phoenix valley was dominated by agriculture in the first half of the twentieth century and relied heavily on groundwater for irrigation. After World War II, the population increased rapidly and many agricultural areas transformed to urban and suburban areas. By the 1970s, drawdown exceeded 100 meters in many wells and land subsidence up to six meters was recorded in some areas [*Anderson*, 1995; *Galloway et al.*, 1999; *Tillman and Leake*, 2010]. Arizona passed legislation in 1980 to authorize the Arizona Department of Water Resources (ADWR) to regulate groundwater depletion, allocate resources, and minimize overdraft with the goal of eliminating overdraft by 2025. In particular, Active Management Areas (AMA) with significant prior drawdown, were heavily regulated [*Tillman and Leake*, 2010; *Galloway and Burbey*, 2011]. Because of the law, surface water was supplied to the city by the Central Arizona Project canal and groundwater pumping was reduced. Nonetheless, subsidence and earth fissuring continued in the Phoenix AMA [*Casu et al.*, 2005; *Galloway and Burbey*, 2011], as well as several other locations in Arizona: the Avra Valley and Tucson [*Schumann and Andserson*, 1988], Casa Grande [*Jachens and Holzer*, 1982], and Eloy [*Epstein*, 1987]. The most recent deformation observations are collected by ADWR with an ongoing land subsidence monitoring program using InSAR [*Conway*, 2013] and updated earth fissure maps are maintained by the Arizona Geological Survey (AZGS) [*Arizona Geological Survey*, 2015].

Phoenix, Arizona is situated in the Basin and Range Province, which formed in two phases of Tertiary crustal extension. First, low-angle normal detachment faults trending northeast-southwest accommodated much of the extension. Next, high-angle normal faults trending southeast-northwest formed steep basin bounding ranges, rotating and tilting along the décollement [*Jenny and Reynolds*, 1989]. The impermeable, tilted igneous or metamorphic bedrock eroded over time, filling the basins with sediment. These consolidated and unconsolidated alluvial sediments are hosts to Phoenix AMA groundwater systems. [*Anderson*, 1995; *Reynolds and Bartlett*, 2002].

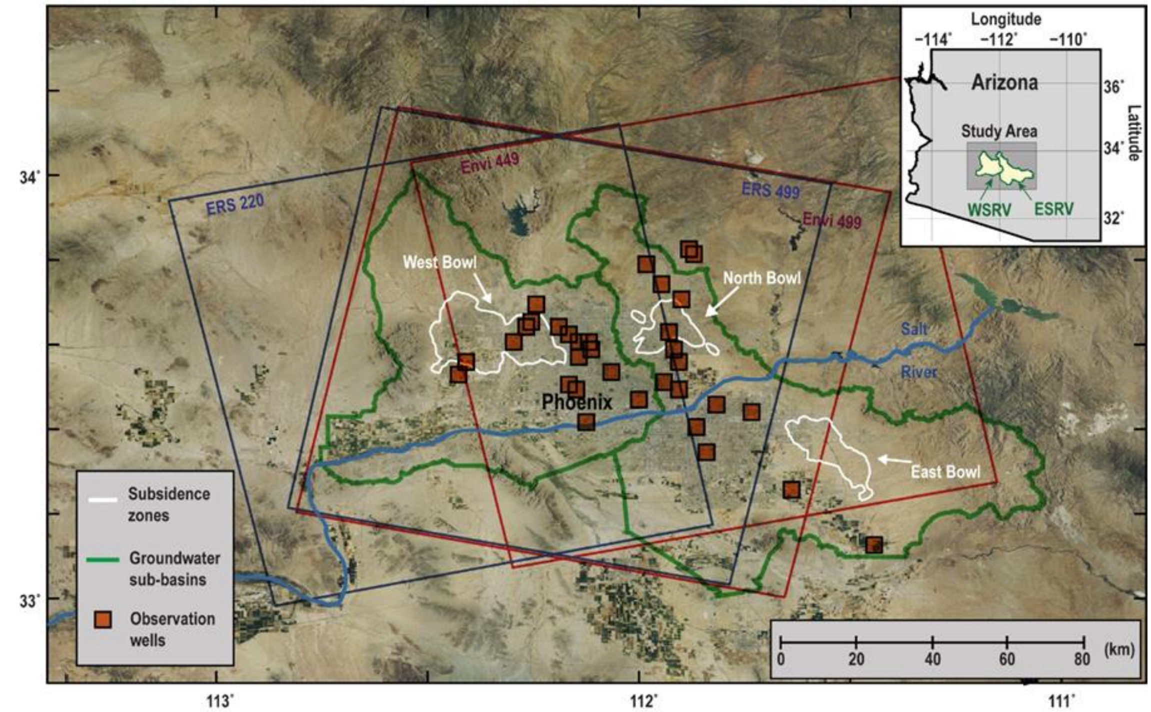

Figure 2.1. Phoenix Study Area. ERS and Envisat satellite footprints are shown with blue and red boxes, respectively. Orange boxes are observation wells for hydraulic head time series analysis. White outlines mark known subsidence zones recognized by ADWR, and green polygons outline the ADWR East Salt River Valley and West Salt River Valley groundwater sub-basins, which are distinct hydrologic units. Aerial photography (1-m resolution) composite from National Agriculture Imagery Program.

ADWR divides the Phoenix AMA into sub-basins that act as distinct, independent hydrologic basins [*Freihoefer et al.*, 2009]; the East Salt River Valley (ESRV) and West Salt River Valley (WSRV) sub-basins encompass the study area of this paper (Figure 2.1). Sediment stratigraphy is similar between sub-basins and is broken into three spatially varying units. The youngest, upper alluvial unit is composed of sand, gravel, and some fine-grained silts, representing recent floodplain deposits. The middle basin-fill unit consists of interbedded sands and gravels with an increasing number and thickness of fine-grained layers of clay, silt, and mudstones. The lower alluvial unit overlies, or is in fault contact with, the bedrock and consists of conglomerate and gravel near the basin margins, grading into mudstones towards the basin center [*Corkhill et al.*, 1993; *Dubas*, 2010].

Most aquifer-bearing units are contained within the middle unit and are considered unconfined, with lenses of finer-grained material acting as confining layers. Depth to bedrock ranges from a few hundred to more than 3000 meters and the basement surface is uneven. The WSRV is host to a thick salt body, is generally deeper, and has a thicker middle alluvial unit compared to the ESRV [*ADWR*, 1999]. Sub-basin stratigraphy and bedrock topography both affect the spatiotemporal evolution of surface deformation in the valley.

Previous work by *Casu et al., 2005* measured land subsidence in Phoenix, Arizona with InSAR time series from the descending track of ERS satellites. Here, synthetic aperture radar (SAR) images are acquired in ascending and descending tracks of ERS, and Envisat satellites from 1992-2011. Through multitemporal interferometric processing of these data sets, the spatiotemporal evolution of the surface deformation is constrained. Multi-track data are combined to obtain vertical and horizontal (east-west) displacement time series components. Next, hydraulic head data from observation wells, provided by ADWR, are used to form a time series at 33 locations. Wavelet decomposition is applied to the time series of vertical surface deformation data and hydraulic head levels to construct the time-frequency representation of the signal. The elastic components are then isolated from the inelastic trend. The availability of elastic and inelastic components at selected period durations allows for the estimation of mechanical properties of the aquifer system, including, the elastic storage coefficient, the inelastic skeletal storage coefficient, and the compaction time constant [*Hoffmann et al.*, 2003a; *Wang and Kümpel*, 2003]. These parameters are important for groundwater management, modeling, and effective urban planning.

2.2. Data, Methods, and Results

2.2.1 InSAR Time Series Methods

With broad spatial coverage and frequent repeat intervals, InSAR is well suited for studying land subsidence. To measure the time-dependent surface deformation across the Phoenix valley, a multitemporal SAR interferometric approach, the Wavelet-Based InSAR (WabInSAR) algorithm is implemented [*Shirzaei*, 2013; *Shirzaei and Bürgmann*, 2013]. A large set of SAR images acquired from similar radar viewing geometry are precisely co-registered to the same master image. WabInSAR generates a large set of interferograms with respect to predefined perpendicular and temporal baseline thresholds. The flat earth effect and topography are removed using a reference digital elevation model and satellite ephemeris data [*Franchioni and Lanari*, 1999]. The algorithm then applies a statistical framework for identifying elite (i.e. less noisy) pixels based on the complex phase noise that is estimated using wavelet analysis of the interferometric dataset. WabInSAR then implements a variety of wavelet-based filters for correcting the effects of topography correlated atmospheric delay [*Shirzaei and Bürgmann*, 2012] and orbital errors [*Shirzaei and Walter*, 2011]. Through a reweighted least square approach, WabInSAR inverts the interferometric data set and generates a uniform time series of the line-of-sight (LOS) surface deformation and uses these values to fit a linear velocity. The effect of the temporally uncorrelated atmospheric delay is then removed using a high pass filter. The WabInSAR algorithm is thoroughly tested and validated in a variety of settings for measuring deformation associated with volcanic [*Shirzaei et al.*, 2013a] and faulting processes [*Shirzaei and Bürgmann*, 2013]. WabInSAR is applied to ascending and two descending tracks of the C-band ERS and Envisat satellites, spanning periods 1992-1996 and 2003-2010, respectively. ERS satellites acquired data until 2010, however, some of the scenes acquired following 1996 do not cover the entire study area. Commonly, InSAR deformation estimates are validated by independent data, such as GPS. Due to the unavailability of GPS data coinciding with InSAR, in this chapter, the redundancy of measurements between the four datasets: ERS and Envisat, ascending and descending tracks, which show similar velocities and deformation patterns are presented for validation.

In areas with overlapping spatiotemporal Envisat coverage, multi-track acquisition geometries are used to reconstruct deformation in two dimensions and improve the temporal resolution of the datasets. Combined processing techniques cannot be implemented for ERS due to fewer acquisitions, long temporal baselines, and large gaps. Furthermore, there is less spatial overlap between ERS track footprints, resulting in limited coverage of the west and north features. Therefore, the Envisat time series is decomposed into vertical and horizontal (east-west) deformation fields by jointly inverting the LOS deformation time series obtained from ascending and descending tracks [*Samsonov and d'Oreye*, 2012]. First, co-located unique, elite pixels are identified by resampling the descending track onto the ascending track by the nearest pixel, provided the distance is also less than a ground pixel resolution (~100 m). The previously estimated LOS displacement time series, velocity, and variance of each track for each pixel are used going forward. To estimate the uncertainty of the obtained vertical and horizontal components, the concept of error propagation is employed [*Mikhail et al.*, 1978]. Given the 3D displacement field (dx, dy, dz), the LOS displacement is defined as;

$$LOS = S_x dx + S_y dy + S_z dz,$$

$$S_x = -\sin(\theta) * \sin(\propto -270°)$$

$$S_y = -\sin(\theta) * \cos(\propto -270°)$$

$$S_z = \cos(\theta) \tag{2.1}$$

Where, S_x, S_y, and S_z are LOS unit vectors that are a function of the heading angle α and incidence angle θ (for angle values, see Table 2.1), projecting the 3D displacement field onto LOS direction [*Hanssen*, 2001]. An assumption must be made that the contribution of the north-south component of the deformation is negligible. This is a valid assumption, owing to the polar orbit of the SAR satellites and that the nature of the investigated signal is dominantly vertical. This simplifies the mathematical relations linking ascending LOS_A and descending LOS_D observations with directional displacement to;

$$LOS_A = S_{x_A} dx + S_{z_A} dz \ , \qquad \Omega_A$$

$$LOS_D = S_{x_D} dx + S_{z_D} dz \ , \qquad \Omega_D \tag{2.2}$$

where, Ω represents the observation variance-covariance matrix [*Hanssen*, 2001]. Given that the ascending and descending data are not acquired at the same time, acquisitions are interpolated into an evenly spaced time series, which may smooth out fluctuations that occurred during that timeframe. To minimize this effect, only acquisitions separated by a few days are selected. Considering Equation (2.2) in a matrix form;

$$\begin{bmatrix} LOS_A \\ LOS_D \end{bmatrix} = \begin{bmatrix} S_{x_A} & S_{z_A} \\ S_{x_D} & S_{z_D} \end{bmatrix} \begin{bmatrix} d_x \\ d_z \end{bmatrix}, \qquad \boldsymbol{\Omega} = \begin{bmatrix} \Omega_A \\ \Omega_D \end{bmatrix}^{-1}$$

$$\boldsymbol{L} = \boldsymbol{AX}, \qquad \boldsymbol{\Omega} \tag{2.3}$$

where $\boldsymbol{L}$ is the estimated LOS displacements**,** $\boldsymbol{A}$ is the design matrix including unit vectors, $\boldsymbol{X}$ is the vector of unknowns, the estimated directional components of the displacement, and the variance $\boldsymbol{\Omega}$ is estimated by propagating the error from individual interferograms to the final time series (see equation 9 in Shirzaei [2013]). The average standard deviation is estimated to be ~5 mm, which is also confirmed through validation against continuous GPS data [*Shirzaei*, 2013]. To calculate the variance covariance matrix of the horizontal and vertical components $\boldsymbol{Q}$;

$$\boldsymbol{Q} = (\boldsymbol{A}'\boldsymbol{P}\boldsymbol{A})^{-1},$$

$$\boldsymbol{X} = (\boldsymbol{A}'\boldsymbol{P}\boldsymbol{A})^{-1}\boldsymbol{A}'\boldsymbol{P}\boldsymbol{L},$$

$$\boldsymbol{P} = \sigma_o{}^2\boldsymbol{\Omega}^{-1} \tag{2.4}$$

where $\boldsymbol{A}'$ is the transpose matrix of $\boldsymbol{A}$, $\boldsymbol{P}$ is the weight matrix, $\sigma_o{}^2$ is the primary variance factor, assumed to be 1 and is updated following the inversion to obtain the secondary variance factor [*Mikhail et al.*, 1978].

Table 2.1. Phoenix Satellite Information. Ascending and descending ERS and Envisat data

Satellite	ERS		Envisat	
	Ascending	Descending	Ascending	Descending
Track No.	220	499	449	499
Heading Angle	350°	192°	350°	192°
Incidence Angle	23°	23°	23°	23°
No. of Images	6	12	29	50
No. of Interferograms	7	25	239	423
Earliest Image	1992-6-21	1992-7-10	2005-03-25	2004-02-02
Latest Image	1996-4-10	1996-4-28	2010-10-15	2010-10-18

2.2.2 InSAR Time Series Results

ERS satellites provide the earliest C-band SAR data from June 1992 to April 1996; satellite acquisition geometry, the number of images, and interferograms generated are detailed in Table 2.1. Ascending interferograms do not cover the entire study area but provide good coverage of the western valley. Figure 2.2a is an example of a wrapped interferogram from June 06, 1993 to April 25, 1995. One phase cycle, or fringe, represents 28 mm displacement in LOS direction. The example contains many noisy pixels due to the

Table 2.2. Line-of-sight and Vertical Velocities

Zone	ERS LOS		Envisat LOS		Envisat
	Ascending	Descending	Ascending	Descending	Vertical
West Valley	−1.23	− 1.40	−1.30	− 1.28	-1.39
North valley	− 1.09	− 0.71	− 0.67	− 0.80	0.75
East valley	n/a	− 0.18	− 1.81	− 1.56	-1.83
Zone of uplift	1.01	0.75	0.53	0.61	0.60

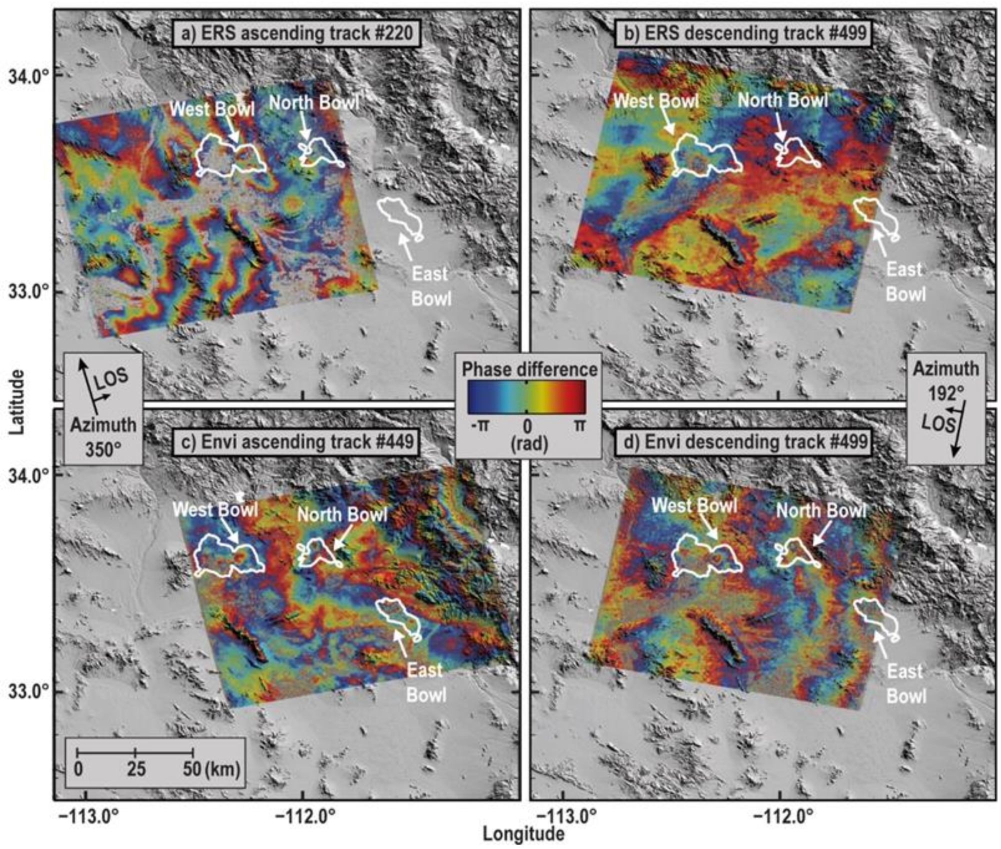

Figure 2.2 Wrapped Interferograms. (a) Ascending ERS #220 (1993-06-06 to 1995-04-25) (b) descending ERS #499 (1996-02-18 to1996-04-28) (c) ascending Envisat #449 (2006-02-03 to 2007-08-17), and (d) descending Envisat #499 (2004-07-26 to 2006-06-26). One color cycle is 28 mm displacement. Increasing phase is motion away from the satellite.

the long duration between acquisitions, partially obscuring the subsidence feature. Compare this to an example from the ERS descending track spanning Feb-18-1996 to Apr-28-1996 (Figure 2.2b), where there is less noise and clear subsidence in the west valley. The Envisat mission provides numerous images of Phoenix, yielding a robust picture of deformation

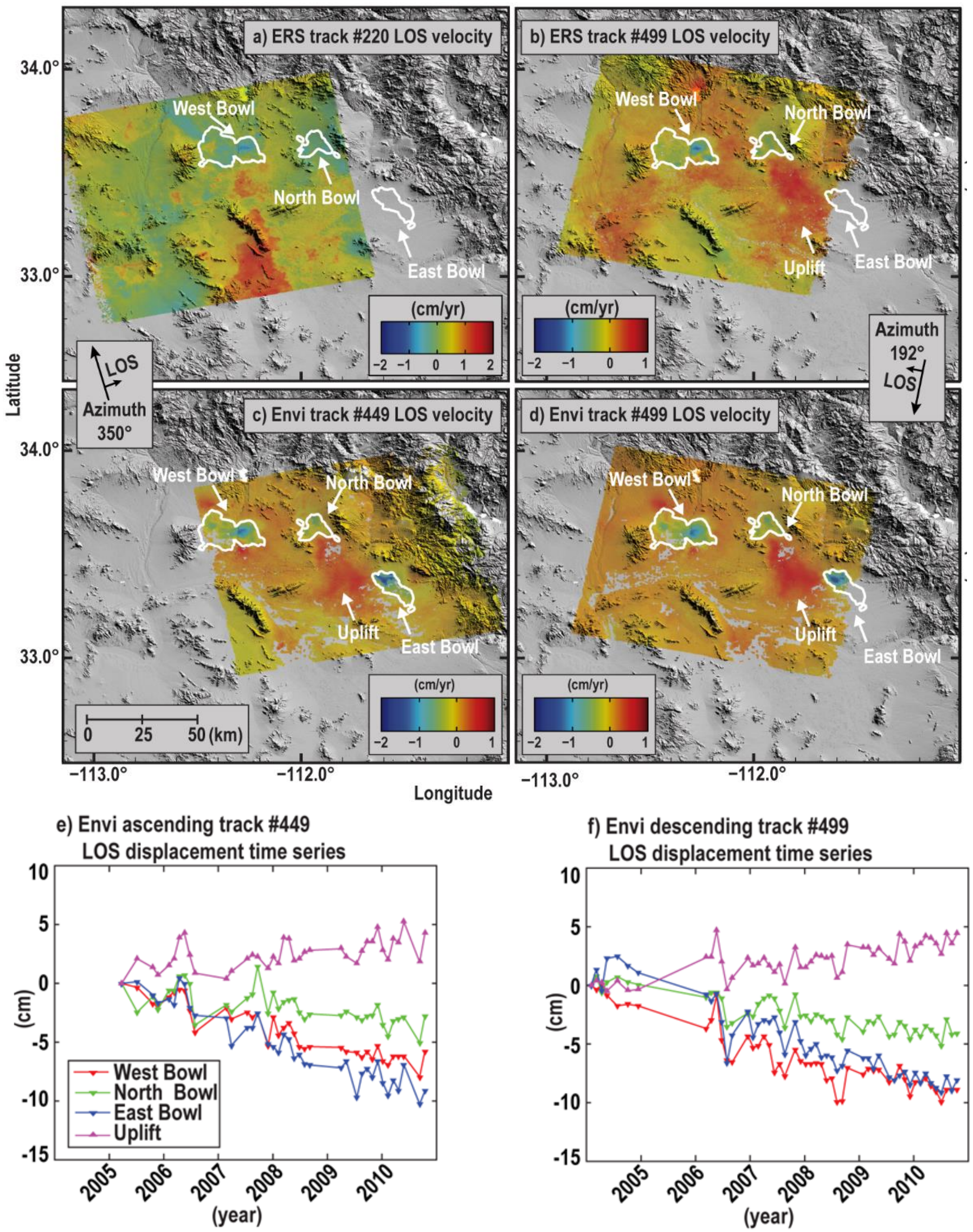

Figure 2.3. Line of Sight Velocity Maps and Time Series. The magenta circle is the stable reference pixel used in InSAR processing. LOS velocities for (a) ERS ascending Track 220, (b) ERS descending Track 499, (c) Envisat ascending Track 449, and (d) Envisat descending Track 499. The LOS displacement time series for Envisat (e) ascending and (f) descending are pixels with maximum subsidence or uplift. Location of pixels for time series shown in e) and f) are: West Bowl (-112.30, 33.61), North Bowl (-111.94, 33.68), East Bowl (-111.60, 33.37), Uplift (-111.83, 33.39).

spanning February 2004 to October 2010 and details are listed in Table 2.1. An ascending wrapped interferogram from Feb-3-2006 to Aug-17-2007 (Figure 2.2c) shows clear deformation fringes for three features labeled West Bowl, North Bowl, and East Bowl. A descending example from Jul-26-2004 to Jun-26-2006 (Figure 2.2d) displays comparable deformation patterns.

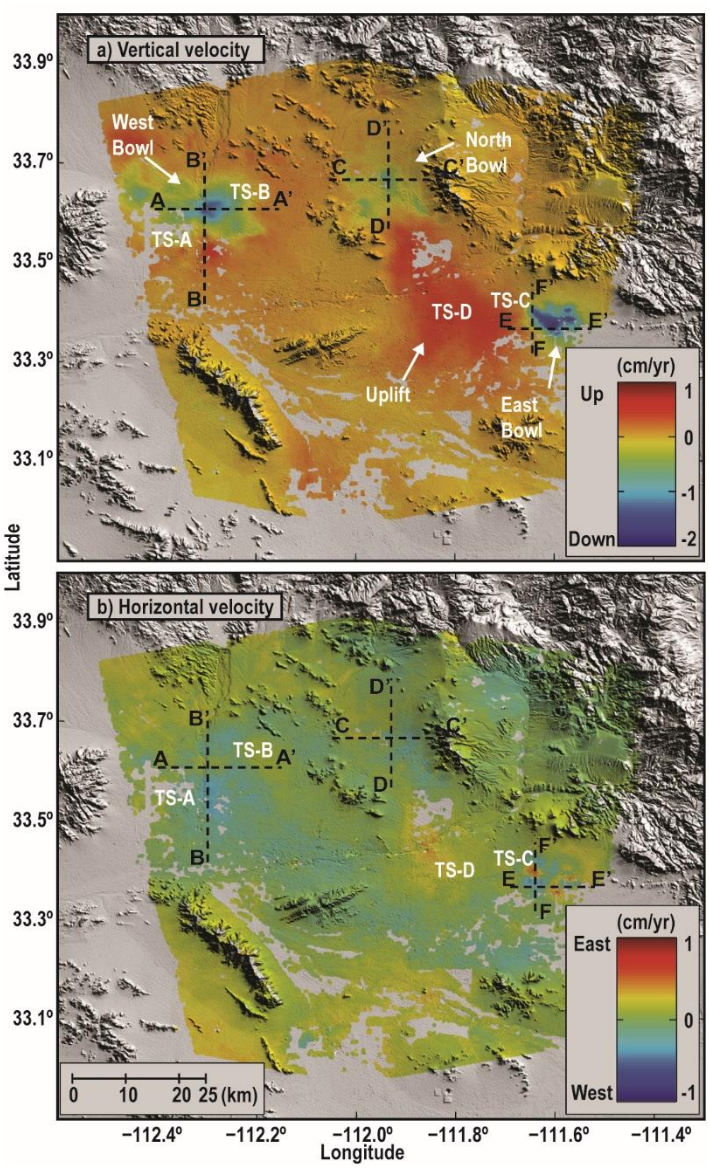

Figure 2.4. Vertical and Horizontal Velocity Maps from Combined Envisat Datasets. Displacement time series profiles from A-A' to F-F' (detailed in Fig. 2.5.) and locations of wells referenced in Figs. 2.7, 9, & 10 are TS-A to TS-D.

The estimated velocity fields for each dataset are compared to verify consistent patterns between datasets (Table 2.2). The ERS velocity fields (Figure 2.3a & b) reveal two zones of subsidence, labeled West Bowl and North Bowl. The eastern valley, where a known subsidence zone is located, is outside of the ERS footprints. Envisat velocities (Table 2.2) and deformation feature locations (Figure 2.3c & d) agree well with ERS and capture all three zones of subsidence, including the East Bowl. The LOS subsidence rates in the East Bowl are -1.81 cm/yr. from ascending, and -1.56 cm/yr. from descending tracks.

The locations of subsiding zones in Envisat data agree with those independently identified in InSAR by ADWR [*Conway*, 2013]. The sensitivity of InSAR to vertical motion and the similarity of deformation rates for each track lead to the conclusion that the vertical component of displacement is dominant [*Bürgmann et al.*, 2000]. The LOS time series at four locations (West, North, and East Bowls and Uplift) are detailed in Figure 2.3e & f. There is an agreement between the long-term trends at each location in both tracks.

Envisat datasets are combined (Equation 2.3) to estimate the vertical and horizontal velocity. Vertical velocities range from -1.83 cm/yr. subsidence to +0.60 cm/yr. uplift with a standard variance of 0.85 mm/yr. The velocity field for elite pixels is displayed in Figure 2.4a & b.

Vertical velocities are comparable to LOS rates (Table 2.2), as are the feature locations (Figure 2.4a). Horizontal velocities range from 0.77 eastward cm/yr. to 0.53 westward cm/yr. with a standard variance of 0.15 mm/yr. The horizontal velocity field (Figure 2.4b) exhibits a nearly valley-wide westward trend, which coincides with the direction of groundwater flow in existing groundwater models, except for eastward motion near the Uplift zone and complex behavior near the East Bowl.

Deformation profiles through time are examined for each subsiding feature in the valley (locations identified in Figure 2.4). The West Bowl profiles are characterized by steady subsidence next to a smaller zone of uplift to the south (Figure 2.5a-d, A-A' & B-B'). Comparatively, the North Bowl profiles feature less cumulative subsidence and are made up of discontinuous subsidence bowls (Figure 2.5e-h, profiles C-C' & D-D').

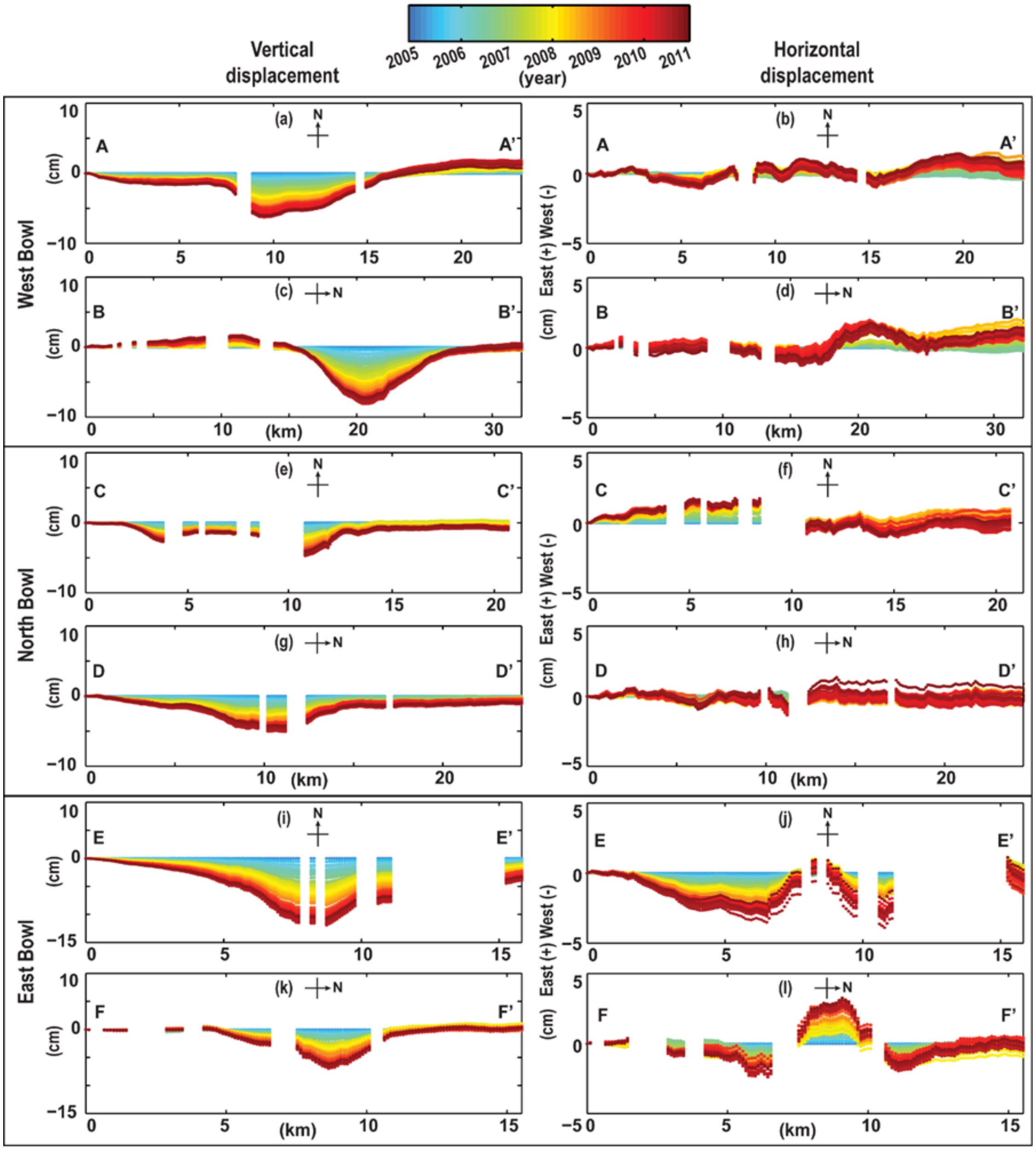

Figure 2.5: Profiles of InSAR Vertical and Horizontal Displacement Time Series. Profiles are marked from A-A' to F-F' in Figure 2.4; gaps occur where noise is statistically significant throughout the interferograms and the pixel is excluded.

Horizontal displacement along cross-section C-C' is unique in that the eastern side of the transect oscillates, while the western side shows relatively steady eastern motion. The East Bowl (Figure 2.5i-l, profiles E-E' & F-F') is asymmetric with a steep vertical subsidence progression next to a relatively stable area in the northwest section of the feature. Horizontal displacement also shows interesting patterns from F-F', with westward motion to the north and south and eastward motion in the center. Hypotheses for this observed behavior, including various possible aquifer system heterogeneities and structural controls, are discussed in Section 2.6.

2.2.3 Hydraulic Head Level Time Series

Hydraulic head levels from observation wells provide direct measurements of the fluid pressure at depth. Pumping, recharge, intra-basin transfer, and stress affect groundwater levels and changes can take place over a range of time scales [*Galloway and Burbey*, 2011]. Challenges can arise with these observations; they may only represent nearby conditions, may be affected by proximate pumping, or represent multiple aquifer-aquitard units. The Groundwater Site Inventory (GWSI) Database maintained by ADWR provides observation well locations, measurements, and information on well status. ADWR wells with three or more measurements coinciding with the InSAR data time series are identified in Figure 2.6 with circles [*Davis et al.*, 2014]. Observation wells previously used by the USGS to identify regional groundwater level trends [*Tillman and Leake*, 2010], that also have 25 or more measurements coinciding with Envisat are identified in Figure 2.6 with boxes. In the Phoenix metropolitan area, 33 wells were suitable for CWT time series analysis using the chosen methodology described in Section 2.2.4. These wells are scattered around the valley and not necessarily located near zones of maximum subsidence or uplift.

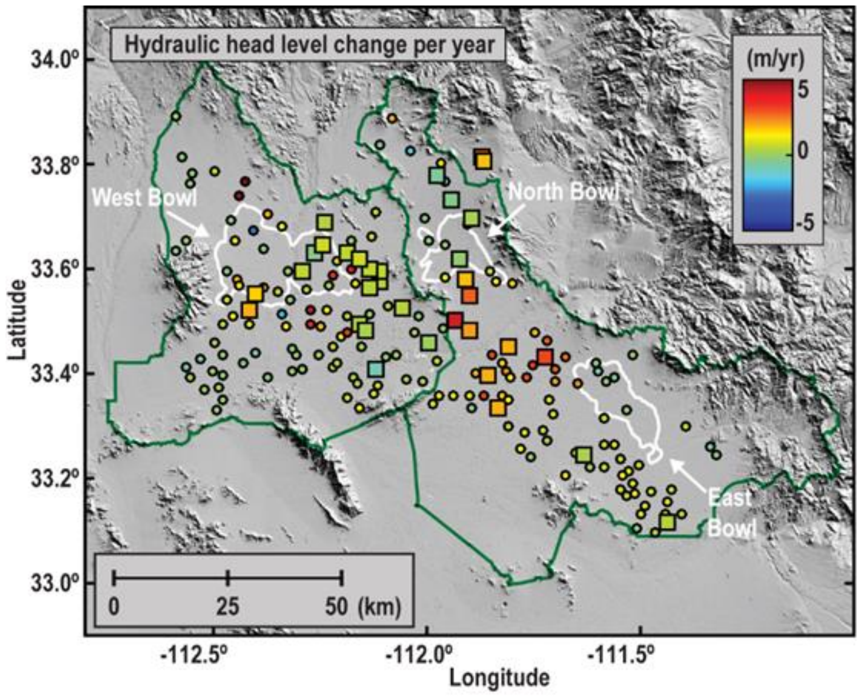

Figure 2.6. Hydraulic Head Levels. Colored boxes and dots show the average yearly change in hydraulic head levels from 2003-2012. Boxes are wells used in time series analysis.

To examine head level data in conjunction with InSAR vertical displacement data, a group of pixels is selected coinciding with observation well locations. Examples of this comparison are shown in Figure 2.7, and the locations of the sites are shown with the prefix TS- in Figure 2.4. For wells near the west valley subsidence feature (Figure 2.7a & b, TS-A & TS-B), head levels trend upward from 2003 to 2012 by tens of meters, in contrast to ongoing subsidence. As discussed in Section 2.3-4, this deformation behavior is likely due to the slow draining of aquitard lenses. A different trend is observed in wells located near the uplifting zone (Figure 2.7c & d, TS-C & TS-D), where there is a correlation between increasing head levels and uplift. This contrast suggests there are significant heterogeneities throughout the valley in the spatial distribution of aquifer and aquitard units. Where interesting deformation patterns occur in the east valley, there are no nearby observation wells with sufficient data to form a time series.

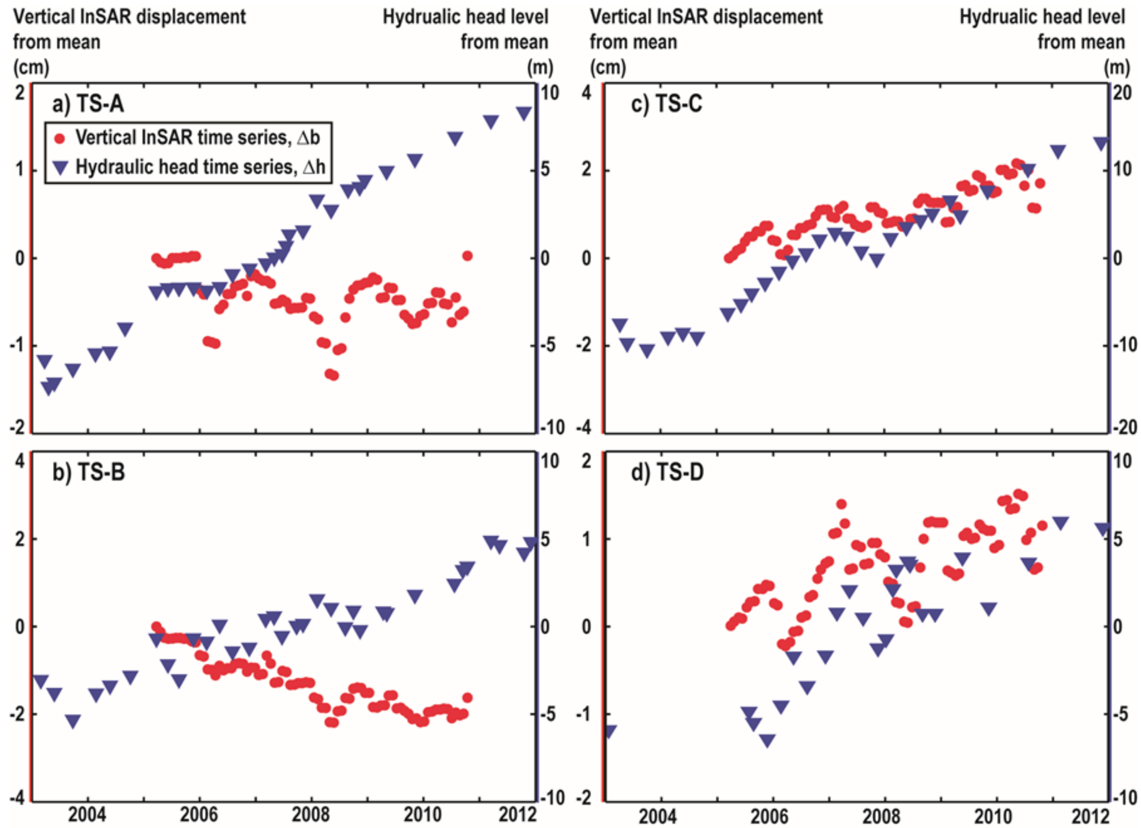

Figure 2.7. Deformation Near Wells. The difference from the mean value for each dataset: hydraulic head level time series, Δh, and nearby pixels of the vertical InSAR time series, Δb. Locations of pixels/wells are indicated in Figure 2.4. Note that observation wells record increasing hydraulic heads both in proximity to subsidence features (TS-A & TS-B) and the uplift zone (TS-C & TS-D).

Residual compaction of slow draining aquitard layers and the effect of poroelastic rebound can both be characterized by modeling vertical deformation as an exponential function of time [*K. Terzaghi*, 1925; *Buisman*, 1936; *Chaussard et al.*, 2014]. To test if this delayed behavior is present in vertical deformation time series, the following equation is used;

$$\Delta b = M(e^{(Bt)}\text{-}1) \tag{2.5}$$

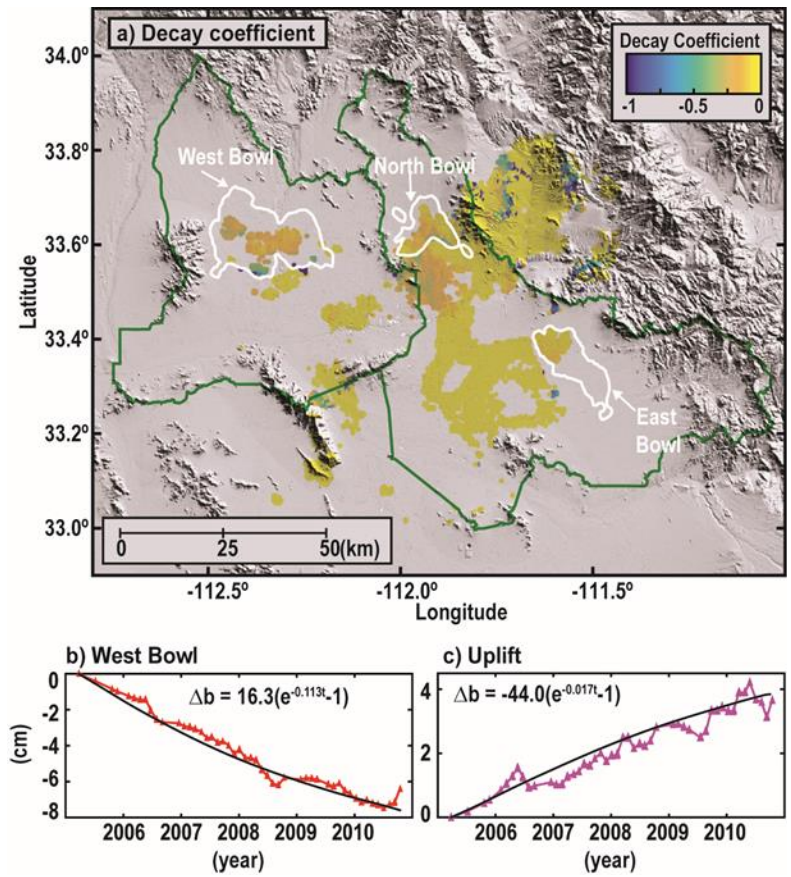

Figure 2.8. Residual Compaction. Decay coefficients are estimated for each pixel, Δb, using a genetic algorithm that passes the chi-squares 95% test. Examples of this relationship are shown for the (b) west valley and the uplift zone (c).

Where Δb is the vertical deformation time series, M is the coefficient representing the magnitude of aquifer response (subsidence M>0, uplift M<0), B is the coefficient of decay [-1,0], and t is the time of the observations. The coefficients are estimated using a genetic algorithm, which is a random, iterative optimization technique based on the principles of natural selection [*Haupt and Haupt*, 2004; *Shirzaei and Walter*, 2009] to identify the optimum M and B. Equation (2.5) is defined as the cost function. Next, an initial population is generated, and through random operations such as pairing and mutation, the algorithm minimizes the cost function and eventually, converges to a set of coefficients. Next, a chi-squares test is performed to include only those pixels where the fit passes at the 95% confidence level (Figure 2.8a). Examples of this analysis are shown for the west valley and the uplift zone (Figure 2.8b & c). Higher decay coefficient values are found in and near subsidence features and lower values characterize the uplift zone. However, delayed compaction and poroelastic rebound do not exhibit strong exponential behavior. It is possible that the observation period is not long enough, or the aquifer system response to changes in pore pressure is not at a delayed stage. In future work, a poroelastic model will be used in conjunction with a longer observation period to further explore this relationship.

2.2.4 Signal Decomposition via Wavelet Transform

Decomposition of a time series into short-term, elastic and long-term, inelastic components are necessary to synthesize deformation and hydraulic head data to estimate aquifer parameters. Earlier studies have applied principal component analysis (PCA), to separate seasonal and long-term components of surface deformation and hydraulic head level changes [*Chaussard et al.*, 2014]. Despite its advantages for signal decomposition, PCA does not provide a significant spectral resolution suitable for dealing with signals of low amplitude [*Rencher*, 2002]. The Fourier transform of the time series signal will identify relevant frequencies, yet does not describe when it occurs in the series. A windowed Fourier transform can provide the time-frequency representation, but the selection of a window size limits the resolution of either the time or frequency components.

To overcome these limitations, continuous wavelet transform (CWT) is applied. CWT offers a time-frequency representation of the time series signal. With this method, the CWT of a time series, $X(n) = \{x_n\}_{n=1 \ldots N}$, which in this study is the InSAR and hydraulic head level time series, along with time step, δt, can be defined via convolution with a scaled and normalized wavelet function, ψ_o, as follows [*Christopher Torrence*, 1998];

$$W(a,n) = \psi^T(n,a)^* X(n) \tag{2.6}$$

$$\psi(n,a) = \left(\frac{\delta t}{a}\right)^{1/2} \psi_o\left(\frac{n\delta t}{a}\right)$$

Where a is a scaling parameter, ^{T} is the complex conjugate, and * is the convolution operator. The time resolution increases with a decreasing scale size, while the frequency resolution decreases with a decreasing scale size. CWT can be evaluated using the convolution theorem in the Fourier domain [*Christopher Torrence*, 1998]. The global wavelet spectrum, G, at scale a is defined as;

$$G(a) = \frac{1}{N}\sum_{n=1}^{N}(W(a,n))^2 \qquad (2.7)$$

Using linear algebra, Equation (6) can be re-written in the following form;

$$W(a,n) = \Psi(n,a)X(n) \qquad (2.8)$$

Where Ψ is a n x n circulant matrix, ψ is the first row of Ψ and each row vector is rotated by one element forward relative to the preceding one. Here, the derivative of a Gaussian (DOG) wavelet function is used with degree m, which is dependent on a non-dimensional time parameter η and is defined as follows:

$$\psi_o(\eta) = \frac{(-1)^{m+1}}{\sqrt{\Gamma(m+\frac{1}{2})}}\frac{d^m}{d\eta^m}(e^{-\frac{\eta^2}{2}}) \qquad (2.9)$$

Providing a high spectral resolution suitable to identify high frequency, *m*=30, low amplitude signals within the time series. Since the time series are padded with zeroes, a cone of influence (COI) needs to be defined to identify the region of the wavelet spectrum, which is affected significantly by the edge effect. To identify these areas, an e-folding time ($\sqrt{2}a$) is used for the autocorrelation of the wavelet spectrum at each scale [*Christopher Torrence*, 1998]. This selection assures that the wavelet spectrum for the discontinuity at the edge drops by a factor of e^{-2} and thus the edge effects are negligible beyond this point.

Recently wavelets have been applied to a variety of SAR applications for data analysis and interpretation. This includes precise orbital error correction [*Shirzaei and Walter*, 2011], topography correlated atmospheric delay reduction [*Shirzaei and Bürgmann*, 2012], differential interferogram inversion and time series generation [*Hetland et al.*, 2012], a new approach for multitemporal InSAR analysis [*Shirzaei and Bürgmann*, 2013], and analysing dense InSAR time series to extract components due to aseismic faulting processes [*Shirzaei et al.*, 2013a]. CWT avoids data shrinkage and provides a large spectral resolution suitable for extracting non-stationary signal components with small amplitude [*Christopher Torrence*, 1998]. One consideration before implementing CWT is to ensure the time steps are consistent when comparing different datasets. Hydraulic head levels are interpolated in this study to coincide with the previously generated InSAR time series. Another step before decomposing the signal is to remove the long-term trend from both the InSAR and hydraulic head level time series. Next, the wavelet power spectrum is generated for the vertical and horizontal components of InSAR and the hydraulic head level time series. In the vertical InSAR and hydraulic head time series, the short-term component is isolated by the period range between 0.5 to 1 years. Periods less than a half year are unreliable due to the repeat interval of satellite data and the assumption that a physical deformation in response to pore pressure change is delayed.

This range is reconstructed into a time series including short-term components reflecting recoverable, elastic deformation and seasonal variations of the hydraulic head levels. This reconstructed short-term signal is subtracted from the original time series to identify the remaining long-term signal components, which are akin to inelastic, irrecoverable compaction and multi-year trends in the water table level.

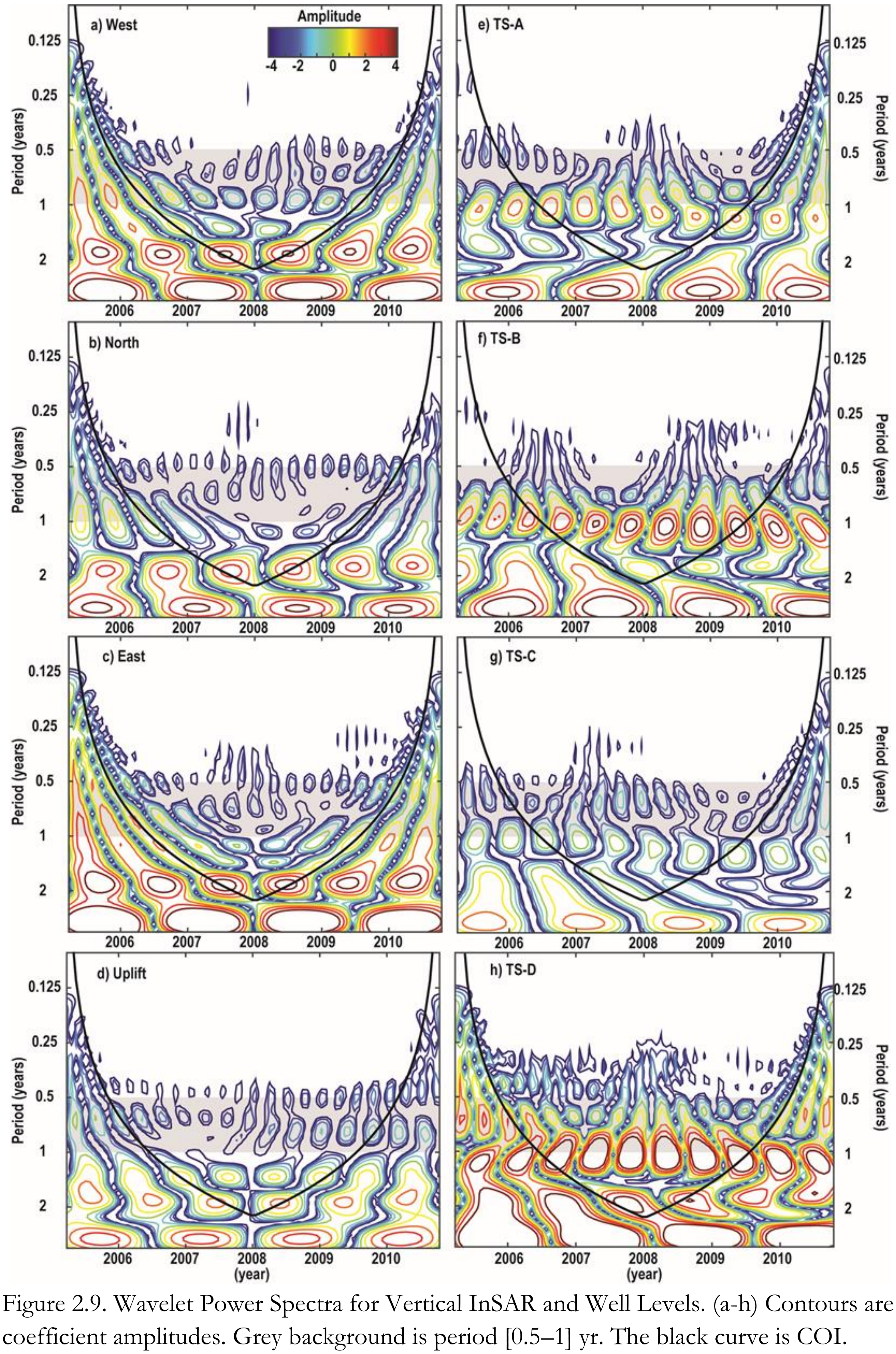

Figure 2.9. Wavelet Power Spectra for Vertical InSAR and Well Levels. (a-h) Contours are coefficient amplitudes. Grey background is period [0.5–1] yr. The black curve is COI.

Separating the short-term and long-term signal components in vertical InSAR and hydraulic head level time series is needed to estimate aquifer system parameters. The wavelet power spectrum (WPS) shows the distribution of a frequency component with respect to the time and is shown for selected InSAR pixels and observation wells in Figure 2.9. Each WPS contains a black curve, the Cone of Influence (COI) that marks the boundary of where signal decomposition is influenced significantly by edge effects. Since the time series is padded with zeroes in CWT, regions outside the COI are not reliable and are identified with a grid pattern. The West Bowl (Figure 2.9a) and East Bowl (Figure 2.9c) have high rates of subsidence and less short-term periodicity than the north valley (Figure 2.9b) or the uplift zone (Figure 2.9d). Overall, the vertical InSAR WPS are lower in amplitude than the hydraulic head WPS, which varies by data type and the strength of the seasonal response. Each observation well WPS (Figure 2.9e-h) contains a significantly short period signal [0.5–1 yr.], but the amplitude varies between the wells. Wells TS-A and TS-B are located adjacent to, yet on opposite sides of, the west valley subsidence feature; TS-B has a higher amplitude signal than TS-A. Well TS-D (Figure 2.9h) is in the uplift zone and shows the strongest amplitude signal component; this is in stark contrast to TS-C, which is west of the eastern subsidence feature and features weaker amplitude. Long-term trends, which have low frequency and are outside of the COI, are better observed upon time series reconstruction.

After WPS formation, shorter periods from [0.5-1] year are isolated and reconstructed into a separate, seasonal time series ($\Delta b_p, \Delta h_p$). The remainder ($\Delta b_l, \Delta h_l$) is dominated by long-term components (Figure 2.10). The results of wavelet analysis are used as inputs to the equations detailed in Section 2.3-4 to determine the elastic storage coefficients, inelastic skeletal storage coefficients, and the compaction time constants.

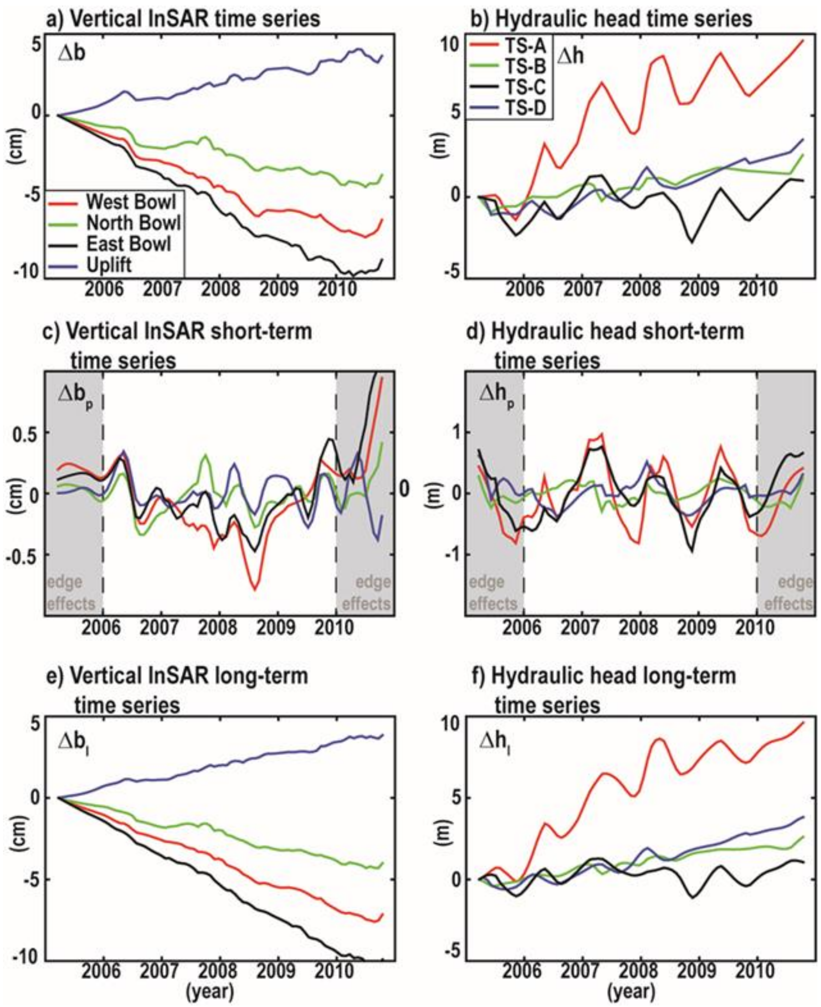

Figure 2.10. Original, Seasonal, and Long-term Time Series. Raw time series for (a) vertical InSAR, Δb, and (b) for hydraulic heads, Δh. Isolated seasonal time series (period 0.5 to 1 year), which are elastic signal components for (c) InSAR, Δb_p, and (d) heads Δh_p. First and last years are excluded to minimize edge effects. The remaining signal components for (e) InSAR, Δb_l, and (f) heads Δh_l represent inelastic signal components.

2.3 Aquifer Parameter Estimation

Aquifer and aquitard behaviors are described by several parameters, including the elastic storage coefficient, S, the inelastic skeletal storage coefficient, S_{sk}, and the compaction time constants, τ. These parameters detail the poroelastic response of aquifer systems to changes in pressure as the water table changes [*Skopp*, 1999]. These parameters can be calculated in laboratory experiments, or derived from known intra-parameter relationships and observations. In this section, a brief description of each parameter is provided along with the methodological framework used for estimating these parameters.

The dimensionless elastic storage coefficient S, or elastic storativity, represents the volume of fluid released or absorbed, per change in the hydraulic head level of an aquifer system area, provided head fluctuations remain above the previous lowest level. For semi-confined aquifer systems, elastic storativity is given by [*Green and Wang*, 1990; *D.M. et al.*, 2011];

$$S_k = S_S b + S_g \tag{2.10}$$

where, S_S is the average elastic specific storage, b is the cumulative thickness of the saturated confined/confining layers, and S_g is specific yield of the saturated, unconfined layers. Specific yield is the volume of fluid that drains from an aquifer volume due to gravitational effects. There is also a component of elastic storage attributed to elastic deformation of aquitard layers before breaching the preconsolidation stress threshold. However, the magnitude is small compared to the aquifer unit contributions [*Galloway and Burbey*, 2011]. Elastic storativity for an aquifer system can be estimated from short-term vertical surface deformation data, Δb_p, which is assumed to equal the change in aquifer system thickness, plus hydraulic head levels Δh_p [*Riley*, 1969];

$$\Delta b_p = S_{ke} \Delta h_p \tag{2.11}$$

S_{ke} is solved for without distinguishing between S_S and S_y, as the thicknesses of the unconfined and confined aquifer units require additional data to resolve.

Elastic storativity S_{ke} is the volume of water that an aquifer unit area absorbs or discharges per change in hydraulic head. It is estimated by comparing the reconstructed vertical InSAR periodic time series Δb_p with the reconstructed hydraulic head level periodic time series Δh_p using the linear relationship described in Equation (2.11). InSAR provides a spatially dense dataset compared to the sparsely located wells. To provide adequate coverage

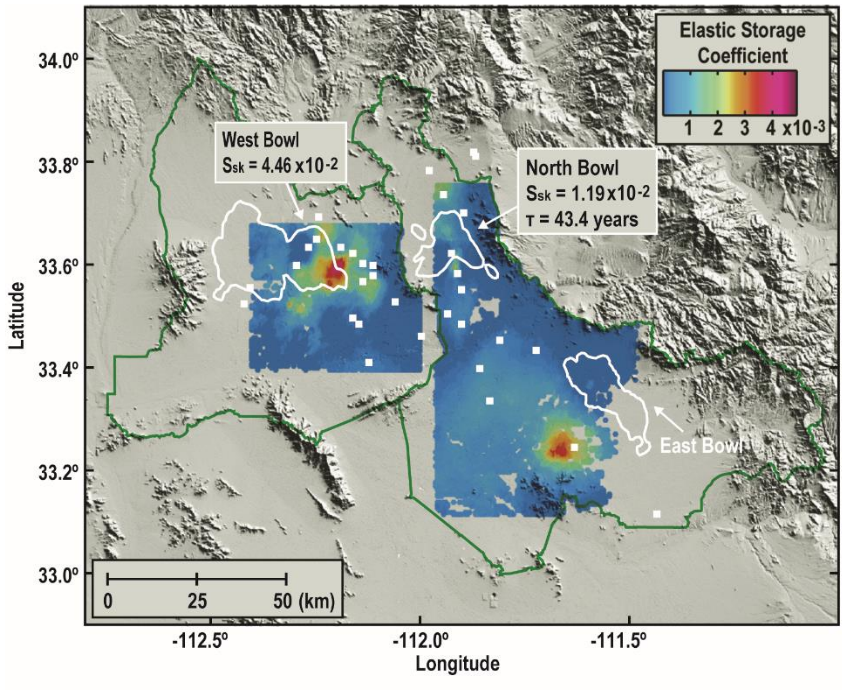

Figure 2.11. Aquifer Parameters. Elastic storativity identified with the colormap. Inelastic skeletal storativity, S_{sk}, and compaction time constant, τ, are shown for features where solvable.

of areas with InSAR data, the hydraulic head data is spatially interpolated using inverse distance for wells <40 km apart in each sub-basin. This distance was selected assuming that lateral changes in unit thicknesses and hydraulic properties are gradual. Inter-basin transfer is assumed to be negligible and the sub-basins act as independent hydraulic units.

The result provides good coverage of the west and north subsiding zones and the uplift zone not the east valley (Figure 2.11). Elastic storativity values in the WSRV range between $5.0\text{x}10^{-6}$ to $4.9\text{x}10^{-3}$, and in the ESRV between $5.0\text{x}10^{-6}$ to $3.8\text{x}10^{-3}$ with error estimates of $1.3\text{x}10^{-6}$. The upper bound of S_{ke} for the WSRV basin is larger than that of the ESRV. The deeper WRSV basin contains a thicker middle basin-fill unit of interbedded sands and fine-grained clays. Since the calculation is for the whole aquifer system column, a thicker middle unit in the WSRV contributes a greater percentage to the column average, accounting for the greater range. The elastic storage coefficient can be used to estimate how much water can be pumped without causing permanent deformation.

The dimensionless inelastic skeletal storage coefficient, S_{Sk}, describes the volume of fluid expelled due to the permanent compaction of an aquitard volume. This occurs when drawdown surpasses the previous lowest level and the preconsolidation stress of an aquifer system is overcome. Residual compaction can occur even after head levels have recovered from prior lows due to the delayed equilibration of aquitard head levels with the neighboring aquifers. The delay can take place many years after hydraulic heads have recovered and is described by the compaction time constant, τ. While elastic deformation is reversible, compaction is irreversible and has a greater magnitude. For cumulative aquitards layers in an aquifer volume, S_{Sk} and τ are found with the following relation [*Hoffmann et al.*, 2003b, 2003a];

$$\frac{\Delta b_l}{\Delta h_l} = S_{sk}\left(1 - \frac{8}{\pi^2}\right)\mathrm{e}^{-\frac{\pi^2 t}{4\tau}} \tag{2.12}$$

Where Δb_l and Δh_l are the inelastic, long-term vertical surface deformation and hydraulic head level time series. Together S, S_{Sk}, and τ describe the storage response of an aquifer system volume to changes in hydraulic head level as the surface deforms. These parameters are found using a genetic algorithm to solve Equation 2.12, inputting the average long-term component of the hydraulic head Δh_l and vertical InSAR time series Δb_l. The coefficients for the north valley feature are: $S_{sk} = 1.19\text{x}10^{-2}$ with a standard deviation of $2.4\text{x}10^{-3}$ and a compaction time constant 43.4 years and 1-sigma confidence interval of [33.1, 53.6]. For the west valley, the inelastic skeletal storage coefficient is $S_{sk} = 4.46\text{x}10^{-2}$ with a standard deviation of $7.0\text{x}10^{-3}$. The compaction time constant could not be resolved for this feature, partly due to ongoing recovery of the aquifer.

2.4 Aquifer System Characterizations

Estimating aquifer parameters from geodetic and hydraulic head level data is an approach that has promise for groundwater modeling. The techniques used in this study can independently verify and improve the spatial distribution and value of conventional MODFLOW input parameters. The distribution of aquifer and interbedded aquitard lenses affects the pattern and mechanics of surface deformation. By estimating the elastic storage coefficients, inelastic storage coefficients and compaction time constants, unit heterogeneities can be identified within and between sub-basins.

The spatial distribution of data can limit estimates, as both hydraulic head levels and deformation data are needed to calculate aquifer system parameters. An example is the scarcity of observation wells with sufficient measurements within or near deformation zones. Even after hydraulic head levels are spatially interpolated, the east valley feature does not have sufficient data to compare with InSAR for elastic storativity estimates (Figure 2.11). Assumptions are made when interpolating sparse points to compare CWT spectra trends with broad deformation data. A gradual gradient of the hydraulic head surface is assumed, which may not be representative of all the aquifer system. Also, spatial interpolation of observation wells is limited to the sub-basin in which they are located. Inter-basin flow is known to occur, but the transfer extent or the effect on hydraulic head levels near the boundaries are unable to be resolved at this stage of research. Another consideration is the depth of observation wells, which may not represent the pore pressure conditions in layers that dominate deformation of the aquifer system.

The elastic storage coefficient is estimated for broad areas of each sub-basin and is assumed to incorporate elastic behavior of both aquifer and aquitard units. Short-term signals are estimated through wavelet analysis in many vertical InSAR pixels and hydraulic head levels, allowing the elastic coefficient to be estimated on a broader scale than the inelastic skeletal storage coefficient. Long-term trends are estimated by subtracting the short-term signal from the original time series and fewer wells are in proximity to deformation zones. The inelastic skeletal storage coefficient is estimated for each subsidence bowl with a detectable long-term subsidence trend and nearby observation well data. A value for the East Bowl could not be estimated, as the nearest observation wells were too far away to reasonably represent the feature for this analysis. Within the subsidence bowls, calculation of compaction time constants is attempted, but given that aquifers are still recovering and the low density of the observation wells, the constant could only be resolved for the north valley feature (Figure 2.11). In future works, using estimated unit thicknesses and hydraulic conductivities, it may be possible to calculate the compaction time constant for all features. This additional data will also specify the vertical distribution of fine-grained interbeds.

2.5 Uplift and Recharge

The broad uplifting zone in the ESRV is characterized by a concurrent increase in hydraulic head levels, which stems from active groundwater management by ADWR. This region has 19 underground storage facilities (USF) managed by ADWR to promote the recovery of the water table. These USF are projected to steadily increase artificial recharge to ESRV aquifer systems from $2.07x10^8$ m^3/yr. in 2005 to $2.54x10^8$ m^3/yr. by 2030 [*Hipke*, 2007]. The total amount of recharge is estimated annually by combining USF, agricultural, and incidental recharge amounts. These estimates are projected into the future by five-year increments and compared to similar projections of estimated future pumping rates. Net recharge estimates were highest for 2005 with $1.67x10^8$ m^3/yr., and decrease each 5-year period through 2020 with an estimated net recharge of $1.73x10^7$ m^3/yr. By the 2025 period, net pumping rates are estimated to be $(1.73x10^7)$ m^3/yr., then $(8.67x10^7)$ m^3/yr. by 2030 [*Hipke*, 2007]. Steady, near linear relationships are observed between hydraulic head levels and combined, vertical InSAR data from 2005-2010 in the uplift zone. If the net recharge projections are accurate, continued uplift of the system is expected for the next decade, followed by subsidence.

2.6 East Valley Deformation Feature

The east valley subsidence feature has the highest deformation rates in the valley and has persisted for decades. A previous USGS estimate of cumulative subsidence measured with repeated leveling surveys between 1933-1980 was 1.58 m [*Carpenter*, 1987]. Although observation well data is lacking in the feature, Envisat ascending and descending coverage allow the retrieval of useful information.

The east valley subsidence feature comprises a unique horizontal displacement pattern during the observation period (Figure 2.12a). The center of the East Bowl moves eastward, while the northern and southern edges of the feature trend westward (Figure 2.12b). Yet there is much agreement in short-term elastic horizontal deformation (0.5-1-year periods) between points in the feature (Figure 2.12c). Although the long-term direction of displacement of point B is opposite of points A & C in Figure 2.12b, the short-term signal components in Figure 2.12c are in the same direction. The horizontal InSAR wavelet power spectra display similar period-amplitude patterns throughout the time series (Figure 2.12d-f). In each power spectra, amplitudes increase for shorter periods towards the end of the time series, regardless of the direction of horizontal motion.

To rule out the possibility that the horizontal deformation pattern is a data artifact effect, the uncertainty of the velocity is estimated (1 mm/yr), and the amplitude of the observed signal is beyond the estimated error in the data. Then, the temporal duration of the ascending and descending datasets is tested as causes to the pattern. To this end, the calculation for vertical and horizontal velocities is rerun for the temporally overlapping period and where both tracks contain nearly the same number of images. The obtained pattern of the horizontal velocities is similar in this analysis and observational errors are not the cause.

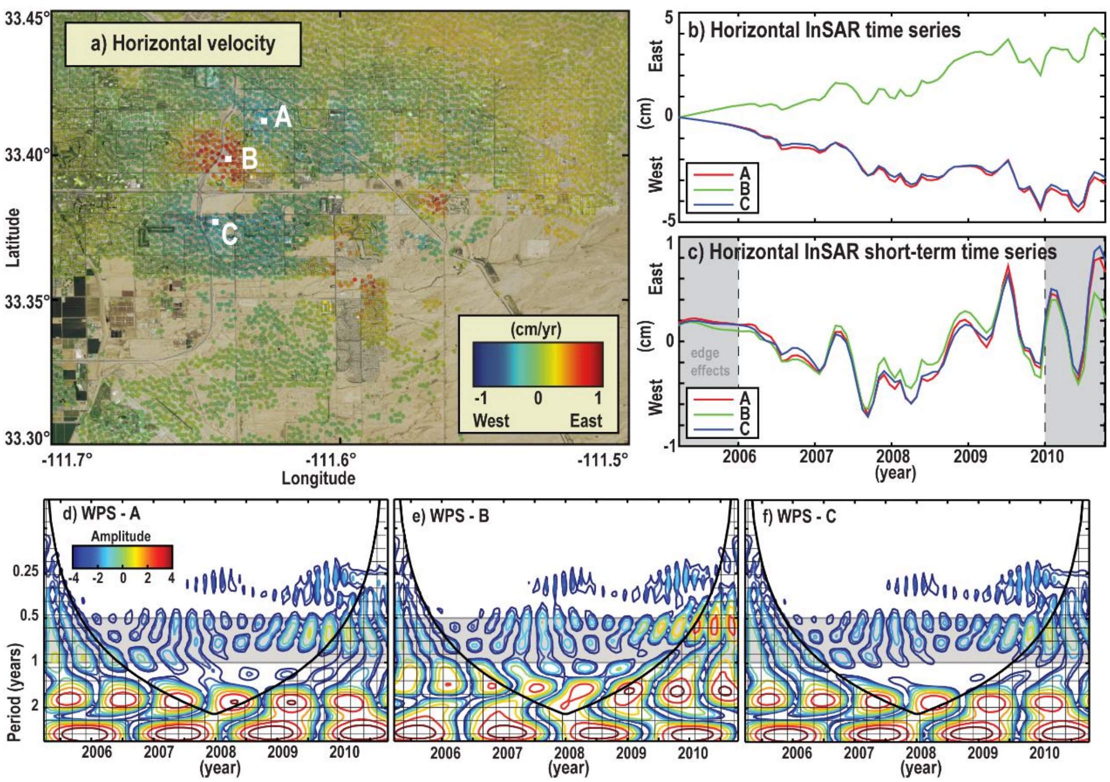

Figure 12. East Valley Deformation. (a) Horizontal velocity of east valley feature atop aerial photo imagery with points A, B &C marking locations for detailed analysis. b) Horizontal time series for each point. Note that the long-term deformation direction of B is opposite of A and C, yet short-term fluctuations appear correlated. c) Reconstructed horizontal time series for short-term signal components highlighting the correlation of all three points. d-f) Wavelet power spectrum for each point.

Several hypothesized models could explain an opposing directional horizontal displacement field. Uneven bedrock topography in the form of a buried impermeable ridge can induce horizontal motion away from the element, or conversely, a bedrock depression induces motion towards the element. Depending on the size of the topographic anomaly, this could also result in differential vertical deformation. The basement topography of the valley is known to be uneven.

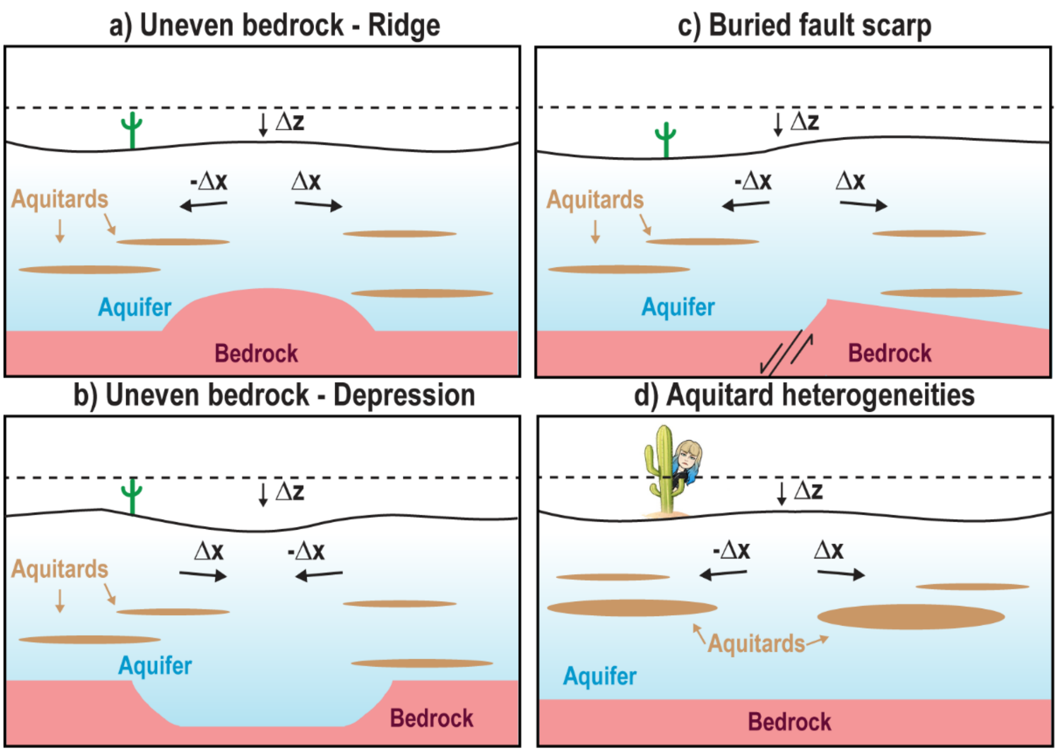

Figure 2.13. East Valley Feature Analysis. Hypothesized models of opposing horizontal displacement and differential compaction by (a) a buried bedrock ridge (b) a bedrock depression, (c) a fault scarp, or (d) aquitard heterogeneities. The dashed black line represents the original surface elevation before deformation.

An impermeable bedrock layer may have experienced significant erosion before burial, leaving a positive or negative topographic feature (Figure 2.13a & b). Another closely related model is a buried fault scarp, which causes draping of the overlying aquifer system layers and subsequent rotations of the beds in opposite directions (Figure 2.13c) [*Sheng et al.*, 2003].

However, if a bedrock feature significantly contributes to this unique deformation pattern, the size and shape of the feature is anomalous. The ADWR groundwater flow model recognizes a steep gradient of cumulative layer thicknesses under this deformation pattern [*Freihoefer et al.*, 2009], but depth to bedrock information is not available at the scale necessary to support a particular model.

To distinguish between these models, detailed measurement of the depth to bedrock under the East Bowl are needed. A third possibility is abrupt, significant differences in aquifer and aquitard thicknesses or spatial distribution, causing differential vertical compaction (Figure 2.13d). This scenario results in horizontal compression towards the higher magnitude compaction zones and horizontal extension where compaction magnitude is lower. This hypothesis alone does not adequately explain the anomaly, as elastic deformation is highly correlated in the short-term (Figure 12c). If the differences in aquifer and aquitard layer thicknesses contributed significantly to the horizontal deformation pattern, the elastic response would vary among locations in the area. To determine which mechanisms, affect this feature, additional data is needed.

2.7 Summary Conclusion

InSAR is useful for examining surface deformation due to groundwater withdrawal and recharge in Phoenix, Arizona. ERS and Envisat satellites provided data used to calculate LOS velocities and the more robust Envisat data from 2003-2010 was used to form ascending and descending time series, which are separated into vertical and horizontal components. Continuous wavelet transform provides a powerful tool for signal decomposition and extracting short-term, elastic and long-term, inelastic components of a time series. Comparing the short-term signal components of hydraulic head and vertical

InSAR data allows for the elastic storage coefficient to be estimated across the Phoenix Valley. The long-term signal components are suitable to estimate the inelastic skeletal storage coefficient for subsidence features with adequate data. Thus, InSAR proves to be an effective tool for analysis of land subsidence and uplift in alluvial basins.

This chapter is adapted from:

M. M. Miller, M. Shirzaei, Spatiotemporal characterization of land subsidence and uplift in Phoenix using InSAR time series and wavelet transforms. *J. Geophys. Res. Solid Earth*. **120**, 5822–5842 (2015).

CHAPTER 3: TIME-DEPENDENT VOLUME STRAIN AND SURFACE FISSURING IN PHOENIX, ARIZONA

Abstract: Significant hazards associated with land subsidence threaten the environment and infrastructure in Phoenix, Arizona. Multitrack Envisat interferometric time series chronicles surface deformation caused by aquifer system compaction due to groundwater extraction. An inversion is constrained with the line-of-sight displacement time series from 2004-2010, solving for deforming triangular prism volumes from the surface to a depth of 900m. Within each prism, volume strain is assumed constant and due only to vertical deformation of a horizontal plane, buried in a homogenous, isotropic elastic half-space. The model is used to solve for the stress tensor near the surface. The ratio of minimum principal stress and tensile strength of the aquifer material is used to identify locations where earth fissures are likely to form. Improving our understanding of the source and mechanisms of subsidence and the resulting stress regime is important for planning and risk management.

3.1 Introduction and Background

Understanding the initiation and propagation of earth fissures due to groundwater exploitation is essential for hazard mitigation in Phoenix and other heavily populated cities atop alluvial aquifers. The fissuring process is directed by movement, subterranean structures, and the in-situ stress field [*Sheng et al.*, 2003]. Poroelastic models allow for an understanding of the stress regime and can be constrained with geodetic observations of surface deformation. In this chapter, time series of InSAR LOS displacements presented in Chapter 2, are inverted to solve for the three-dimensional volumetric strain of subsidence zones (Figure 3.1a). This model is then used to solve for the stress field near the surface and following *Sheng et al., 2003*, the ratio between minor principal stresses and rock tensile strength are calculated to identify areas prone to fissuring.

Existing earth fissures are mapped and described in professional reports [*Arizona Geological Survey*, 2015, 2017] and have been documented in the southwest for decades [*Galloway et al.*, 1999]. Maps specifying the presence of earth fissures (Figure 3.1b) indicate fissures are threatening urban areas with extensive property and infrastructure. Recall from the previous chapter that the Phoenix AMA is divided into sub-basins, ESRV & WSRV, which act as distinct, independent hydrologic basins and have similar sediment stratigraphy [*Freihoefer et al.*, 2009]. Most aquifer-bearing units are considered semi-confined, with lenses of finer-grained material acting as confining layers. Depth to bedrock ranges from a few hundred to more than 3000 meters and the basement surface is uneven. Stratigraphy, bedrock topography, and anomalous features affect the spatiotemporal evolution of deformation and the potential for fissuring.

3.2. Observations and Methods

3.2.1 InSAR Deformation Time Series

InSAR is a valuable tool for studying land subsidence because it has broad spatial coverage and frequent repeat intervals. In *Miller and Shirzaei, [2015],* an advanced multitemporal InSAR algorithm [*Shirzaei*, 2013; *Shirzaei and Bürgmann*, 2013] was applied to sets of 38 and 50 images acquired in ascending and descending orbits of Envisat C-band satellite, spanning the period of 2-Feb-2004 through 18-Oct-2010. Ascending and descending datasets with overlapping spatiotemporal coverage were combined to reconstruct a deformation time series in vertical and horizontal dimensions and improve temporal resolution.

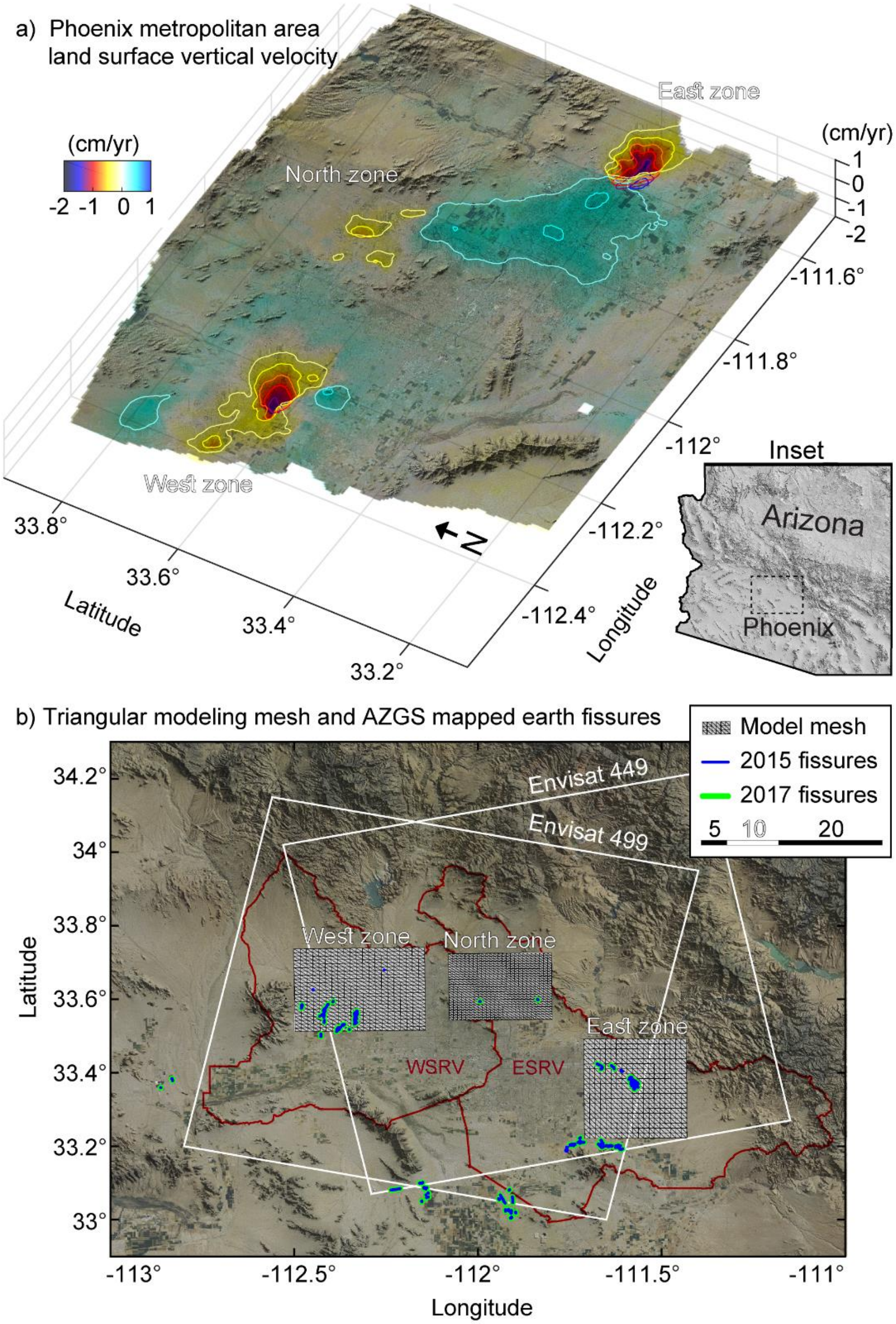

Figure 3.1. Vertical Velocity, Modeling Extent, and Existing Earth Fissures. (a) Phoenix, Arizona vertical velocity map formed from overlapping Envisat satellite frames. (b) SAR frame extent, model mesh for each subsidence zone, and earth fissures as mapped by AZGS. Red polygons outline the ADWR ESRV and WSRV groundwater sub-basins, which are distinct hydrologic units.

Vertical velocities of subsidence up to 1.83 cm/yr were estimated and three zones of subsidence are highlighted, referred to as the West, North, and East 'Bowls' (Figure 3.1a). Image and signal processing, time series and velocity patterns, and long-term and seasonal trends are discussed in detail and the ascending and descending LOS time series obtained in this work are used in the following analysis.

3.2.2 Volumetric Strain Inversion Method

Using a method similar to that of *Mossop and Segall [1999],* an inversion constrained by InSAR displacements is performed to solve for the distribution of volumetric strain caused by aquifer compaction due to water extraction. The deforming volume is discretized into triangular prisms from the surface to a depth of 900-m with depth intervals of 150-m, with an additional interval at 50-m depth to focus on the shallower areas. Within each prism, the volume strain is assumed constant and is only due to the prism vertical deformation [*Mossop and Segall*, 1999]. At the center of each prism $\{\mathrm{X_i}, \mathrm{Y}_i, \mathrm{Z_i}\}$, a horizontal plane is considered to be buried in a homogenous isotropic elastic half-space [*Okada*, 1992]. To solve for volume strain, $u_i(\mathrm{X_i}, \mathrm{Y}_i, \mathrm{Z_i}),\ \mathrm{i} = 1,2,..,\mathrm{m}$, associated with each plane, the *Okada* [1992] Green's functions are modified. Given LOS surface deformation time series, $\mathrm{L} = [\mathrm{L_1}, \mathrm{L_2}, \dots, \mathrm{L_n}]^{\mathrm{T}}$, the following system of equations are solved:

$$\begin{bmatrix} \mathrm{L_1} \\ \cdot \\ \cdot \\ \cdot \\ \mathrm{L_n} \end{bmatrix} = [\mathrm{G_1} \quad \dots \quad \mathrm{G_m}] \begin{bmatrix} u_1 \\ \cdot \\ \cdot \\ \cdot \\ u_m \end{bmatrix} + \begin{bmatrix} \mathrm{r_1} \\ \cdot \\ \cdot \\ \cdot \\ \mathrm{r_n} \end{bmatrix} \quad , \ P = S_0^2 C_{LL}^{-1} \qquad (3.1)$$

where, G includes the elastic Green's functions scaled by the thickness of prism and the LOS unit vectors, $r = [r_1 \dots, r_n]^T$ is the observation residual and C_{LL}^{-1} is a diagonal matrix including the variance of LOS displacements. The variance is estimated during multitemporal interferometric analysis and is on average less than 5 mm. The variance-covariance matrix Q of the volume strain can be obtained as;

$$Q = S_0^2 (G^T P G)^{-1} \tag{3.2}$$

where, S_0^2 is the primary variance factor and usually assumed to be 1 [*Mikhail et al.*, 1978]. To avoid the unrealistic variations of the volume strain, its second derivative is minimized [*Harris and Segall*, 1987]. Availability of the time series of LOS displacement in ascending and descending tracks allows us to obtain time-dependent models of volume strain for each track.

Assuming $\{u_0^1, \dots, u_{N_1}^1\}$ and $\{s_0^{2^1}, \dots, s_{N_1}^{2^1}\}$ are the volume strain time series and the associated variance of an arbitrary prism in the first data set, respectively, and $\{u_0^2, \dots, u_{N_2}^2\}$ and $\{s_0^{2^1}, \dots, s_{N_2}^{2^1}\}$ are the corresponding time series and variance of the same prism in the second data set, N_1 and N_2 are the number of images in ascending and descending data sets. A Kalman filter structure is used to combine these two data sets and generate a seamless map of the volumetric strain $\{y_0, y_1, \dots, y_{N_1+N_2}\}$, that includes both ascending and descending results [*Grewal and Andrews*, 2001]. The *dynamics model* is in the form of;

$$y_k = y_{k-1} + v_{k,k-1} t_{k,k-1} + w_{k-1} \tag{3.3}$$

where, $v_{k,k-1}$ and $t_{k,k-1}$ are the linear velocity and time difference between time k and $k-1$, and w_{k-1} is the system noise. The *measurement model* is given by;

$$y_{k_1} = u_{k_1}^1 + \varepsilon^1$$

$$y_{k_2} = u_{k_2}^2 + c + \varepsilon^2 \tag{3.4}$$

Where k_1 and k_2 refer to the acquisition time of the ascending and descending data sets, respectively, c is the constant shift between the temporal mean value of the ascending and descending data sets with an initial value of $\sum_{i=0}^{N_1} u_i^1 - \sum_{i=0}^{N_2} u_i^2$, and ε is the measurement noise. The system of Equations (3.3) and (3.4) is solved subject to the constraint;

$$^1/_{N_1} \sum_{k_1=0}^{N_1} y_{k_1} = {}^1/_{N_2} \sum_{k_2=0}^{N_2} y_{k_2} \tag{3.5}$$

To obtain initial values used in the Equations (3.3-5), the volumetric strain and variance time series of one track is interpolated on the other. Given the u_a and s_a^2 volume strain and associated variance at time t_a, and u_b and s_b^2 respected values at time t_b, the interpolated volume strain and variance at time t_c is obtained by;

$$u_c = \frac{t_c - t_a}{t_b - t_a}(u_b - u_a) + u_a$$

$$s_c^2 = (\frac{t_c - t_a}{t_b - t_a} s_b)^2 + (\frac{t_c - t_a}{t_b - t_a} s_a)^2 + s_a^2 \tag{3.6}$$

Note that to apply Equation 3.6, it is not required that t_c falls between t_a and t_b. Given the observed pattern of surface deformation map (Figure 3.1a), three zones of volumetric strain are to be generated on three separate meshes. The West zone mesh is 33 km x 25 km divided into scalene triangles with an average horizontal dimension of 1.5 km. The North zone valley mesh is 26 km x 20 km divided into scalene triangles with an average horizontal dimension of 0.7 km. The East zone mesh is 26 km x 30 km and divided into scalene triangles with an average horizontal dimension of 1.6 km.

3.2.3 Synthetic Test

Before examining real data, a checkerboard test like that of *Mossop and Segall* [1999], is set up to determine if the complex spatial pattern can be recovered. This test is performed on the North mesh since it has the finest resolution. Synthetic LOS surface deformation observations are projected via forward modeling from a fabricated volumetric strain model

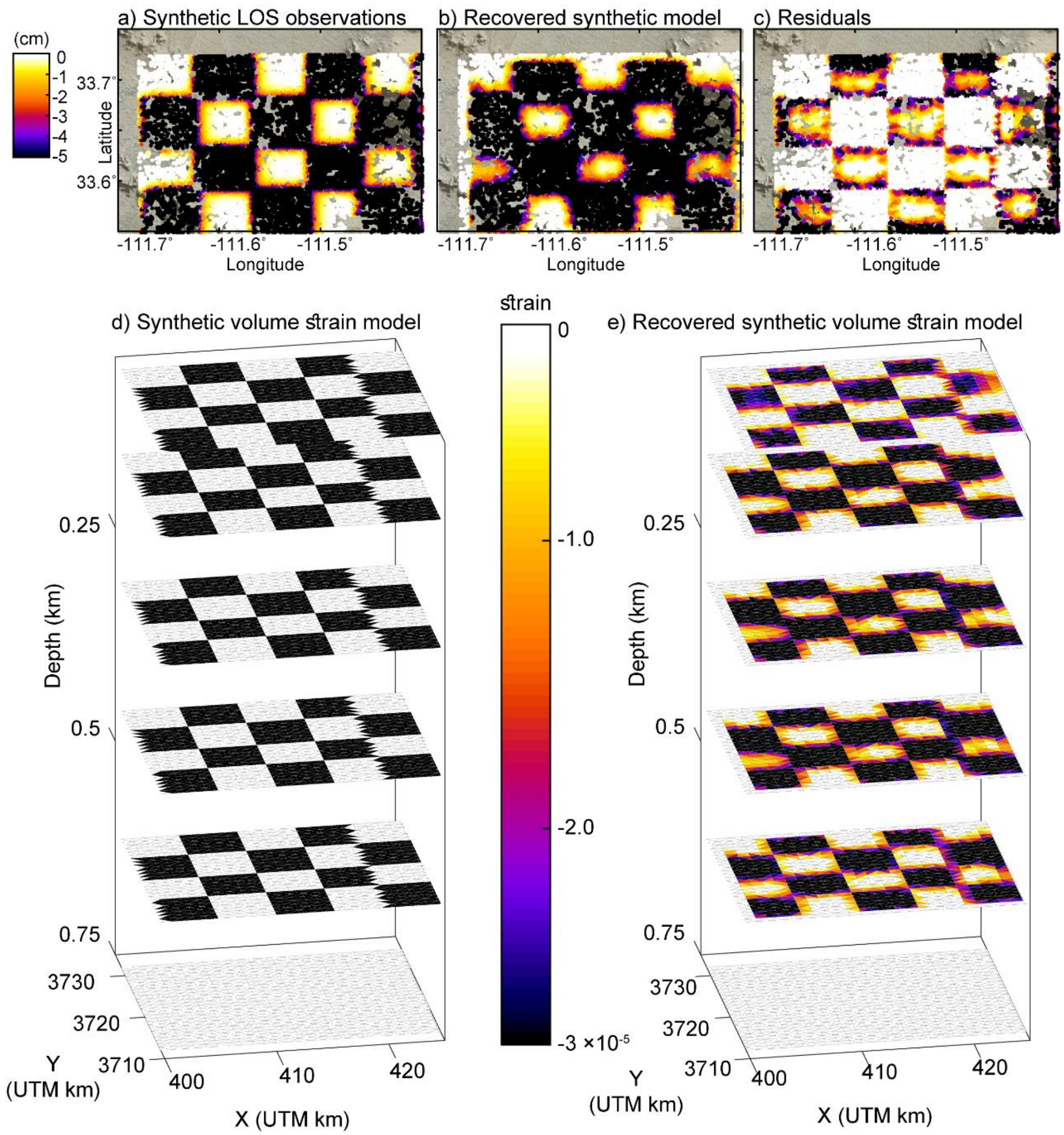

Figure 3.2. Checkerboard Test (a) using synthetic observations, the (b) recovered model and (c) residuals compare the (d) synthetic three-dimensional volumetric strain for forward modeling (c) and the recovered model after inversion of synthetic observations.

displaying a checkerboard pattern with values of either zero or -3x10^{-5} (Figure 3.2 a&d). The synthetic observations are then inverted to solve for recovered volumetric strain (Figure 3.2 b&e) and forward modeled to project recovered observations. The model has sufficient resolution to retrieve major features of volume strain and handle data gaps, when comparing the residuals (Figure 3.2c) between the synthetic and recovered model. However, it is important to note the recovered volumetric strain models tend to dull sharp rectangular edges. Regardless, subsidence zone deformation patterns are generally curvilinear and the impact of dulling using these methods will suffice to proceed with actual observations.

3.3 Time-dependent Volume Strain Results

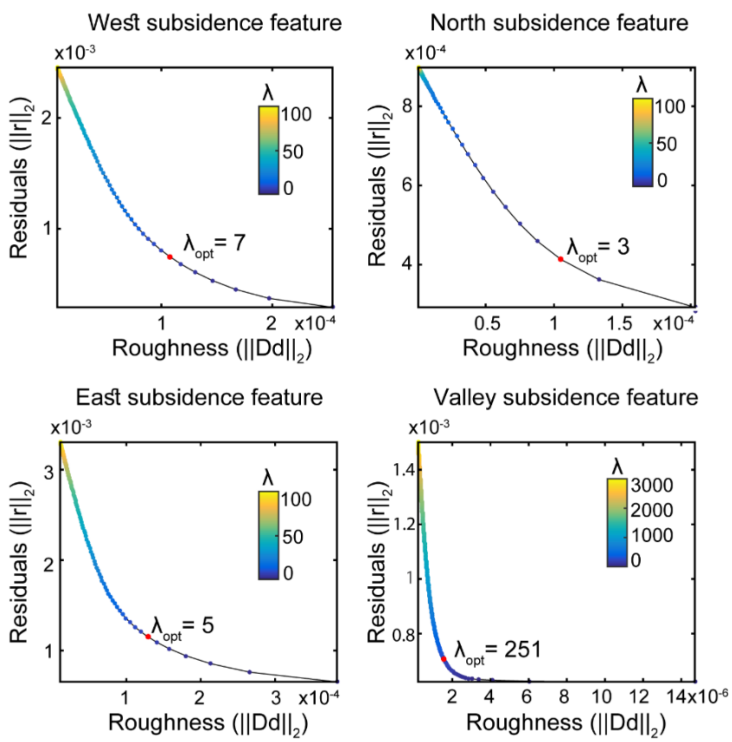

Figure 3.3. Tradeoff Curves for Optimal Smoothing.

To solve for volumetric strain using the displacement time series, the ideal smoothing factor for each subsidence zone is identified. The optimal lambda λ_{opt} is found by starting with a range of test values, and analyzing tradeoff curves (Figure 3.3) of model roughness and model misfit for each smoothing factor. The optimal values (Table 3.1) tend to scale with the size of the model mesh extent. The resulting volumetric strain models provide a detailed picture at depth and highlight nuances between deformation zones. Parameters for each inversion are listed in Table 3.1.

First, the West valley feature cumulative LOS observations, model, and residuals are presented for the ascending (Figure 3.4a-c) and descending (Figure 3.4d-f) Envisat time series. Spatial subsidence patterns are similar between the two perspectives, yet the descending track displays a greater amount of vertical displacement, which is likely due to the additional 13 months captured in that time series. The models reproduce subsidence patterns with minimal residuals; however, misfits attributed to smoothing include less subsidence in the center of the zone and a more diffuse pattern around the periphery. The three-dimensional volume strain models (Figure 3.4g-h) depict the subterranean distribution.

Table 3.1. Volumetric Strain Inversion Parameters

Zone	# of Triangles		Laplacian	
	Plane	Total	λ	z/x ratio
West	924	7392	7	2.7×10^{-2}
North	1300	10400	3	3.5×10^{-2}
East	760	6080	5	3.0×10^{-2}

Second, the North Valley feature cumulative LOS observations, model, and residuals are presented for the ascending (Figure 3.5a-c) and descending (Figure 3.5d-f) Envisat time series. Similarly, to the West Valley, differences between tracks, subsidence patterns, and residuals exist. However, the North valley subsidence pattern is discontinuous and patchy. Despite these challenges, the model reasonably reproduces the deformation patterns model misfit is minimal, while the three-dimensional volume strain models (Figure 3.5g-h) continue to depict the complex geometry in the subterranean distribution.

Third, the East Valley feature cumulative LOS observations, model, and residuals are presented for the ascending (Figure 3.6a-c) and descending (Figure 3.6d-f) Envisat time series. Deformation rates are greater in this feature compared to the other areas. However, the East Valley is not captured in entirety by the descending track, thus the oblong subsidence feature is truncated in the southeast. Incidentally, the area with maximum displacement is captured by both tracks and the three-dimensional volume strain models (Figure 3.6g-h) can depict volumetric strain for this important zone.

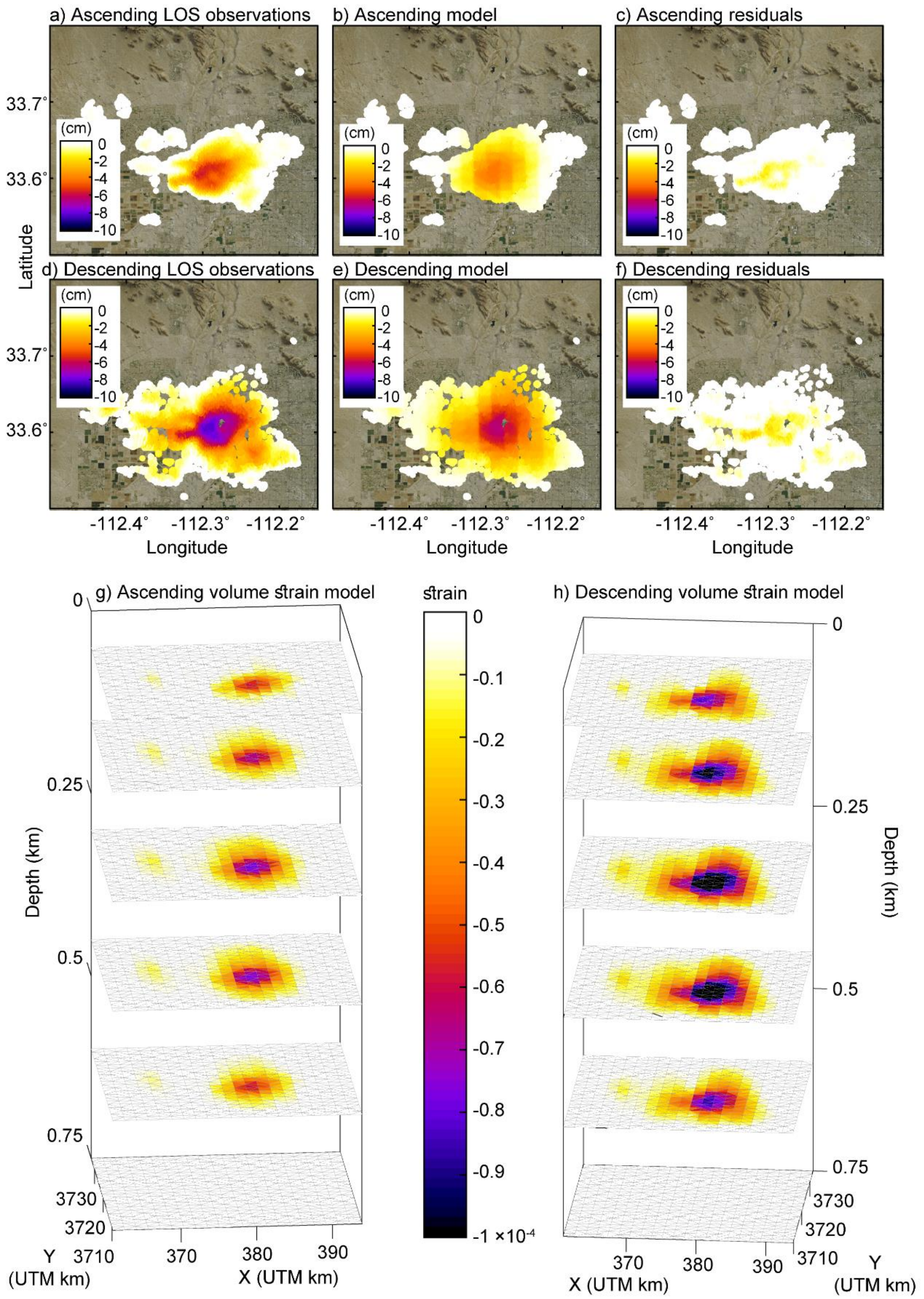

Figure 3.4) West Valley Cumulative LOS Observations, Model, and Residuals (a-c) for the ascending and (d-f) descending Envisat time series and the respective three-dimensional strain models (g-h). This encompasses the time period: Feb-2004 to Oct-2010.

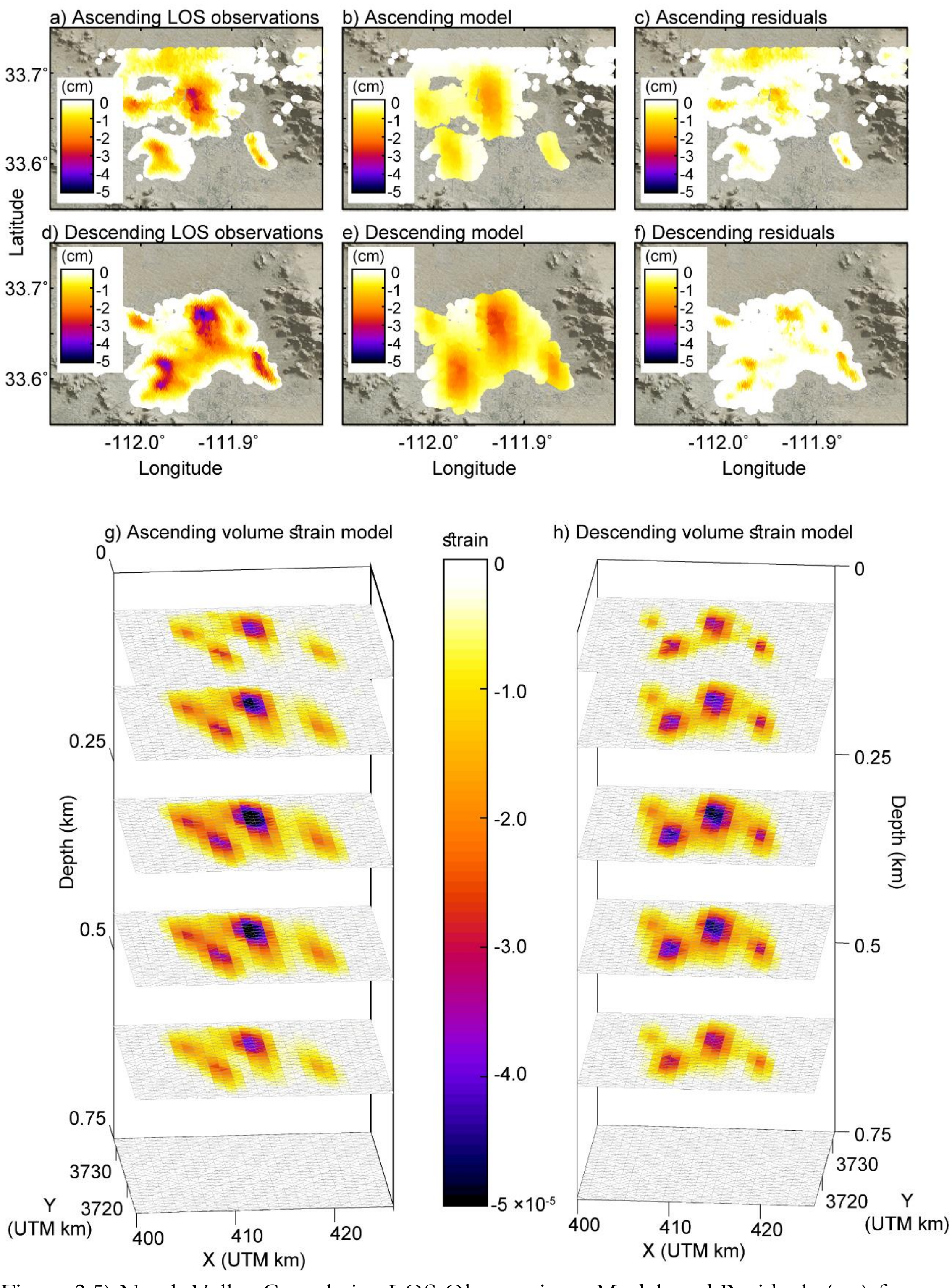

Figure 3.5) North Valley Cumulative LOS Observations, Model, and Residuals (a-c) for the ascending and (d-f) descending Envisat time series and the respective three-dimensional strain models (g-h). This encompasses the time period: Feb-2004 to Oct-2010.

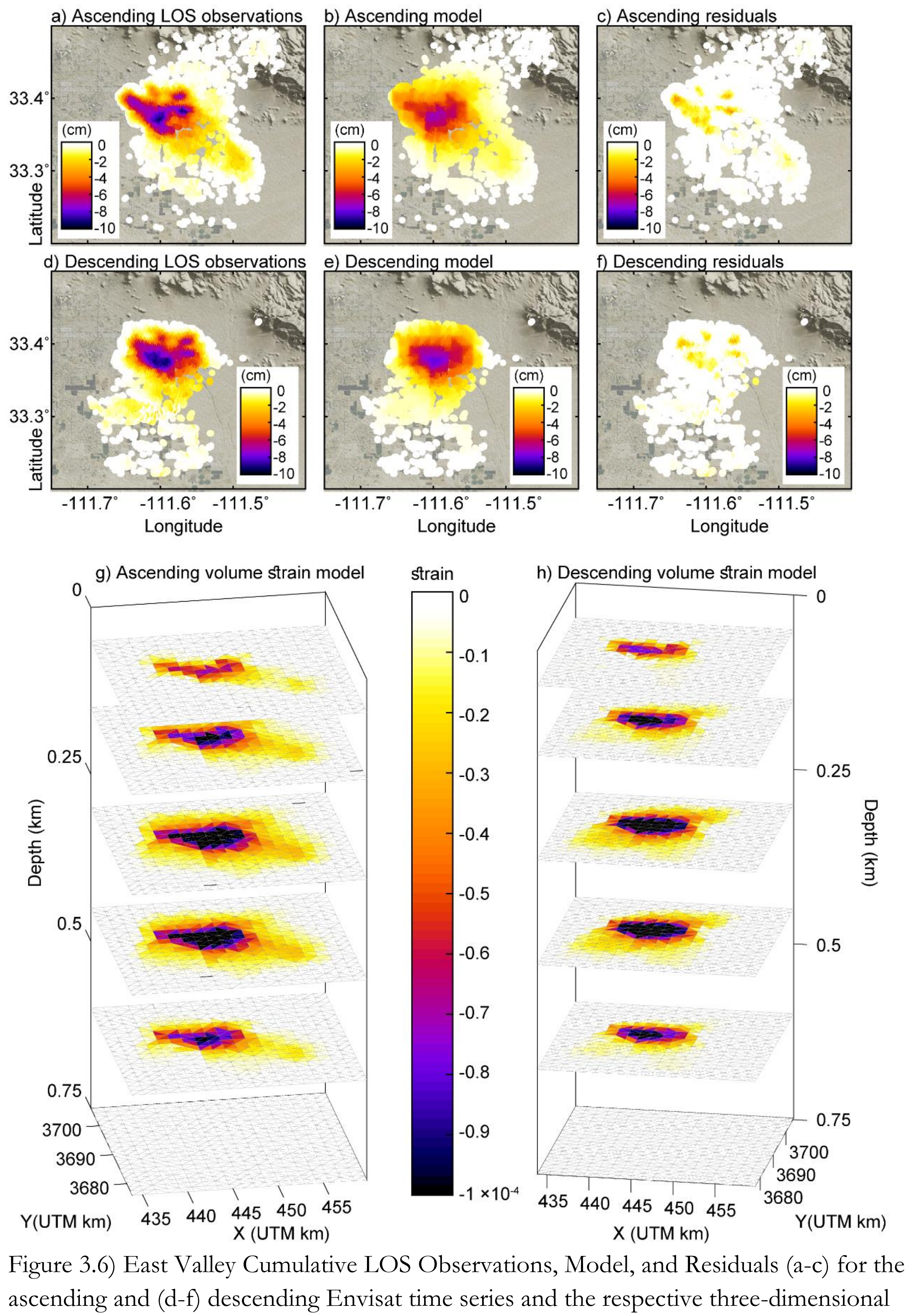

Figure 3.6) East Valley Cumulative LOS Observations, Model, and Residuals (a-c) for the ascending and (d-f) descending Envisat time series and the respective three-dimensional strain models (g-h). This encompasses the time period: Feb-2004 to Oct-2010.

By combining the ascending and descending derived volumetric strain models, we generate time series of strain evolution, spanning 2-Feb-2004 to 18-Oct-2010 (Figure 3.7). For each zone, the prism with the maximum compressive strain is outlined in black and the corresponding time series at each depth plane are shown.

3.4. Earth Fissures

Earth fissures can be initiated in aquifer system sediments from shear failure on vertical planes [*Sheng et al.*, 2003; *Budhu*, 2008]. To identify whether a location is prone to earth fissuring, the minor principal stress/tensile strength ratio R, which is the ratio of minor principle stress σ_3 to the tensile strength τ_s is calculated;

$$R = \frac{\sigma_3}{\tau_s} \tag{3.7}$$

We follow the convention that $\sigma_1 < 0$ is compression and $\sigma_1 > 0$ is extension. Following *Hernandez-Marin and Burbey* [2010], in estimating tensile strength, an intermediate value of tensile strength ($\tau_s = 1 \text{ x } 10^5$ Pa) is assumed, considering the alluvial material contains an amalgamation of various materials from soil ($1\text{x}10^4$ Pa) to caliche ($3.27\text{x}10^6$ Pa) [*Hernandez-Marin and Burbey*, 2010; *Zhang et al.*, 2017]. *Zhang et al.* [2017] asserts that tensile strength is typically tens of kilopascals in clayey soils. To determine minor principal stresses σ_3, the volumetric strain model and the displacement gradient tensor derived from displacements due to angular dislocations is used to calculate near-surface strain on a new observation triangular mesh surface at 1 m depth for the period Feb-2004 to Oct-2010 [*Comninou and Dundurs*, 1975].

Figure 3.7. (Following page) Cumulative Volumetric Strain Models and Time Series of Combined Ascending/Descending Observations (Feb-2004 to Oct-2010) for the West (a-b), North (c-d), and East (e-f) zones.

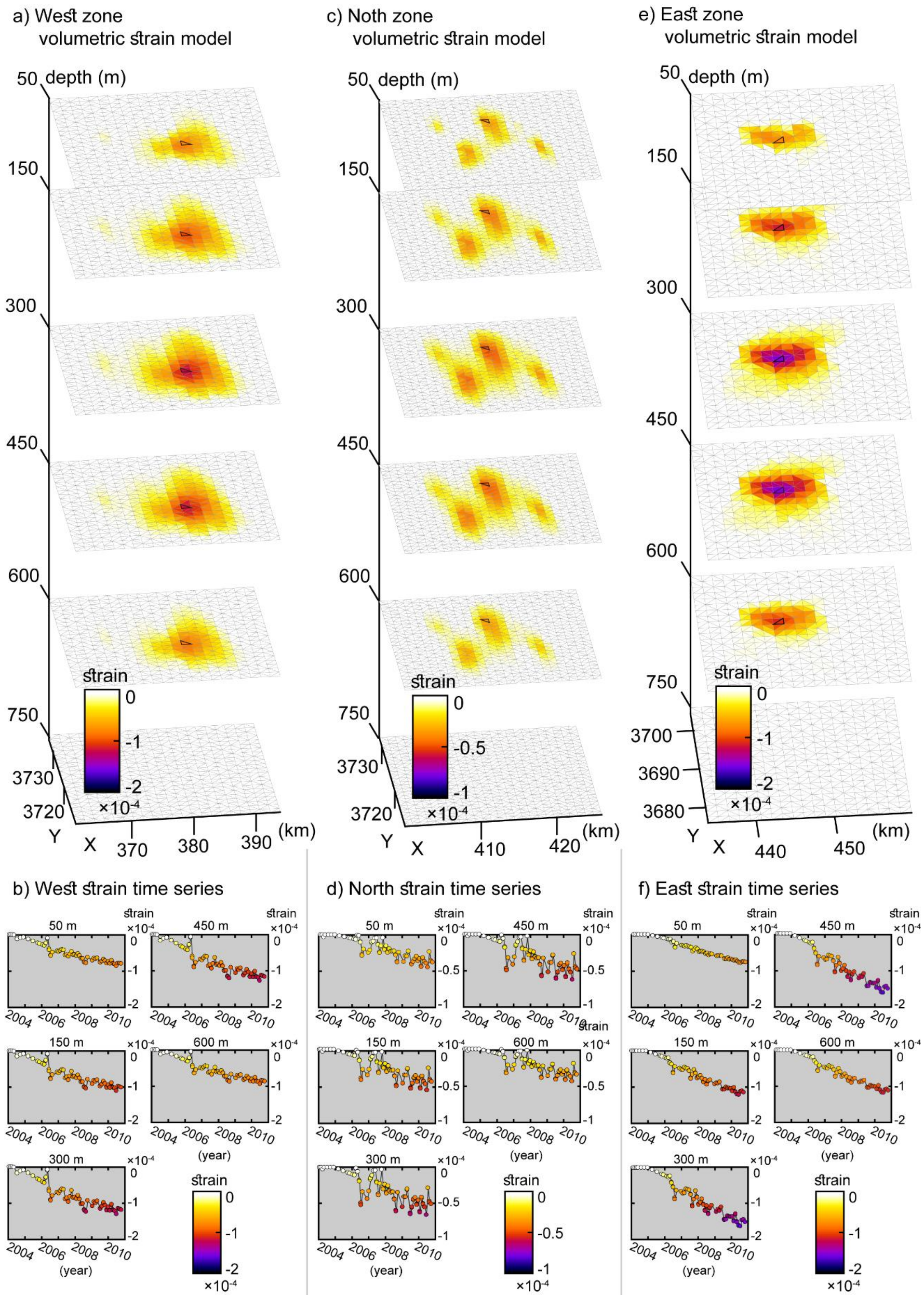

a) West zone
volumetric strain model
c) Noth zone
volumetric strain model
e) East zone
volumetric strain model
depth (m)
50
150
300
450
600
750
strain
0
-1
-2
×10⁻⁴
-0.5
3730
3720
3700
3690
3680
Y
X
370
380
390
410
420
440
450
(km)
b) West strain time series
d) North strain time series
f) East strain time series
50 m
150 m
300 m
450 m
600 m
2004
2006
2008
2010
(year)

Strain is converted to a stress tensor using the linear transformation relations of Hook's Law. Characteristic values, or eigenvalues are identified to isolate the maximum and minimum stresses on the observation surface and the major and minor principle stresses. When the minor principal stress/tensile strength ratio is less than -1, tensile cracks can form [*Sheng et al.*, 2003]. Many areas beyond this threshold of $R < -1$ are towards the perimeter of the subsidence zones (Figure 3.8), with patchier concentrations within the deformation zones. Since these locations are more prone to fissuring and the next step is to compare these locations with mapped earth fissures. Earth fissures are mapped in shapefiles that are distributed by the AZGS with releases in 2015 and 2017 (repository.azgs.az.gov/uri_gin/azgs/dlio/997). Time of fissure discovery is not indicated in the files; therefore, fissure formation may have occurred when stress was distributed differently. Most fissures are in both 2015 and 2017 files with few exceptions, indicating very few new fissures were added during this time.

The West zone (Figure 9a) has many fissures to the south and west of where R-values exceed the threshold during the 2004-2010 period. These fissures may be related to deformation prior to 1992, in which 18 feet of subsidence near Luke Air Force Base (AFB) is estimated to have taken place [*Galloway et al.*, 1999]. However, many areas we identify as 'at risk' are in relatively heavily populated areas, such as Peoria and Sun City West. In the North zone (Figure 3.8b), only two fissures are mapped, yet the perimeter of all three deformation zones are at risk. The East zone is associated with many documented fissures and many other areas are at risk (Figure 3.8c). The aquifer system is complex in this area, including opposing directional horizontal motion [*Miller and Shirzaei*, 2015] and clay zones of low hydraulic conductivity which are associated with sags in subsidence profiles [*Budhu and Adiyaman*, 2013].

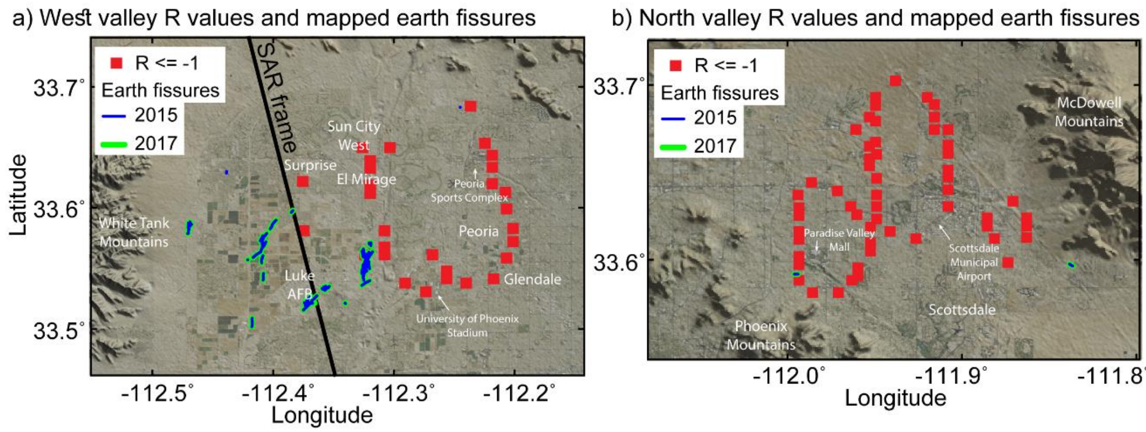

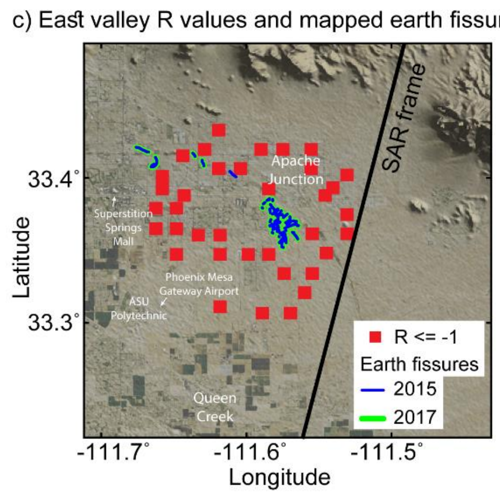

Figure 3.8. Minor Principal Stress/Tensile Strength Ratio **R** and Locations of Earth Fissures (a) for West, (b) North, (c) and East subsidence zones (Feb-2004 to Oct-2010). Fissures mapped and reported by AZGS in 2015 and 2017.

3.5 Concluding Remarks

The ascending and descending InSAR LOS displacement time series are inverted to solve for the three-dimensional volumetric strain of subsidence zones. The model is then used to convert strain to a near-surface stress field using Hook's Law linear transformation. Characteristic values, or eigenvalues are identified to isolate the maximum and minimum stresses on the observation surface and the major and minor principal stresses. The ratio between minor principal stresses and rock tensile strength are calculated to identify areas prone to fissuring.

This study focuses on cumulative displacement and strain from 2004-2010 in Phoenix, as well as areas prone to fissuring due to near-surface stresses. If pumping rates increase, or is pumped from different locations, strain and stress patterns can change. As new radar imagery becomes available and deformation patterns change, the process should be repeated to determine if different or additional areas are at risk for earth fissure formation.

This chapter is adapted from a manuscript in preparation for submission

CHAPTER 4: AQUIFER MECHANICAL PROPERTIES AND DECELERATED COMPACTION IN TUCSON, ARIZONA

Abstract: In recent decades, high groundwater extraction rates, often coincident with periods of severe drought, result in the widespread decline of water levels. Overexploitation of aquifers also causes land subsidence, which poses a severe threat to infrastructure. Tucson, Arizona experiences land subsidence coupled with the depletion of groundwater, a critical water resource for the desert city. Long time series of surface deformation and head levels are examined to understand the spatiotemporal evolution of land subsidence and its implications for aquifer properties. Measurements at extensometer stations indicate rapid compaction of fine-grained material up to 8.5 mm/yr from 1990 to 2005, which results in permanent storage volume losses up to 4.1%. The analysis of densely populated sets of interferograms generated from Envisat and RadarSAT C band acquisitions yields multitemporal maps of surface deformation at unprecedented resolution. These maps reveal that subsidence significantly slows by the late 2000s, corresponding with the implementation of artificial recharge efforts. Subsequent to groundwater level recovery, a brief 6.6-year interval of residual compaction is observed, suggesting a high vertical hydraulic conductivity, which is then shown to be up to $9.8\text{x}10^{-4}$ m/d. The average elastic and inelastic skeletal storage coefficients are estimated for the aquifer system to be $3.78\text{x}10^{-3}$ and $6.01\text{x}10^{-3}$, respectively. Interferometric synthetic aperture radar shows deformation nearly ceases by 2015, likely reducing hazards associated with Earth fissuring and infrastructure damage. This study highlights successful outcomes of water management and conservation plans that preserve existing groundwater reserves and increase artificial recharge.

4.1 Background

Over 650,000 people reside in Tucson, which is in the Upper Santa Cruz (USC) alluvial basin and bounded by fault-block mountains in southeastern Arizona (Figure 4.1a & b). The population is reliant on a semi-confined, unconsolidated aquifer system, which supplies much of the community freshwater demand. Land subsidence and earth fissures associated with groundwater pumping are well documented in the Tucson Active Management Area (TAMA), which includes both the USC and nearby Avra Valley sedimentary basins [*Anderson*, 1988; *Evans and Pool*, 2000; *Carruth et al.*, 2005; *Garcia-Fresca and Sharp*, 2005; *Tillman and Leake*, 2010; *Galloway and Burbey*, 2011; *Conway*, 2015; *Kim et al.*, 2015]. The TAMA was established by the Groundwater Management Act of 1980 in response to decades of subsidence and steep declines in well levels. An important task of ADWR regarding TAMA is to attain safe-yield by 2025, meaning long-term drawdown volumes should equal replenishment volumes [*Jacobs and Holway*, 2004]. To this end, diverted Colorado River water via the Central Arizona Project (CAP) canal is artificially recharging aquifers and is a key strategy against drought-related water scarcity [*Scanlon et al.*, 2016]. Managed recharge is accomplished with gravity-driven spreading basins and underground storage facilities and helps offset groundwater withdrawals and prevents overexploitation. [*Mason and Bota*, 2006]. The groundwater management and conservation challenges facing Tucson offer lessons for cities with similar predicaments [*Megdal*, 2007].

TAMA basin-fill deposits are up to 3800 meters thick, but most productive wells are less than 300 meters, as the water quality declines at greater depths and contains dissolved solids [*Mason and Bota*, 2006]. Valley wide, groundwater flow is typically northward, but pumping alters the flow paths and several areas developed perched aquifers as recharge pools atop aquitard layers [*Hanson*, 1989]. The mountains and bedrock of this region are structurally complicated with many instances of metamorphic core complexes above low-angle décollement faults. The impermeable bedrock basement in the Tucson valley is uneven and offset by high-angle normal faults (Figure 1b), which also displaced some of the lower basin-fill deposits and may affect compaction patterns [*Evans and Pool*, 2000].

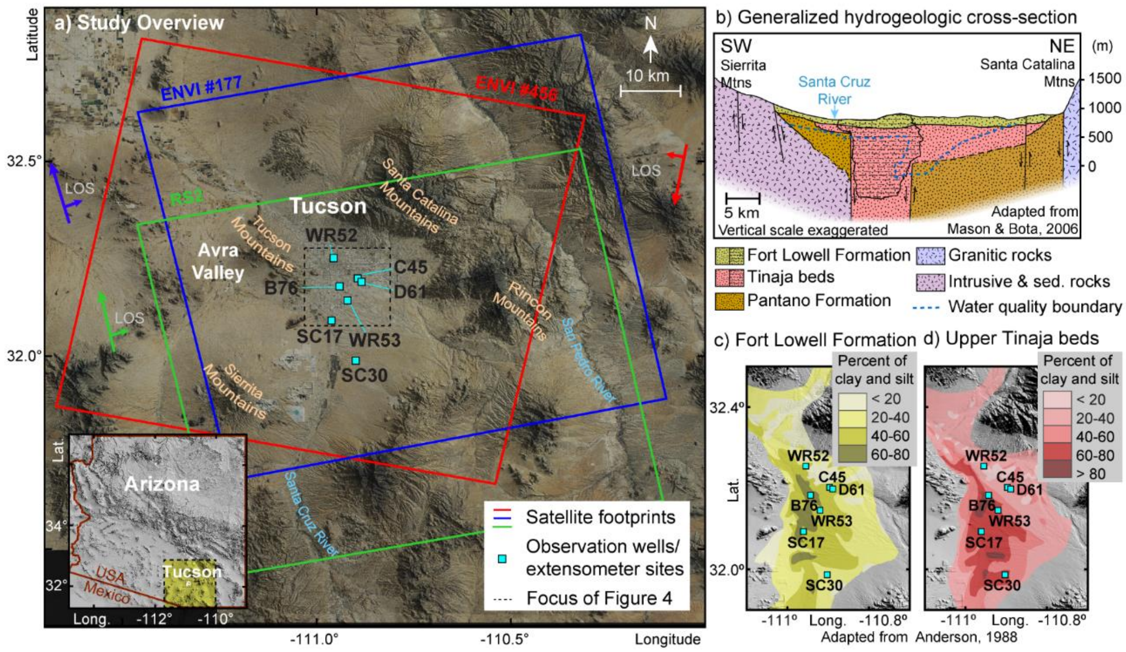

Figure 4.1. Tucson, Arizona Study Area (a) SAR Satellite footprint polygons and observation well sites are equipped with extensometers (b) Generalized hydrogeologic cross-section adapted from *Mason and Bota, 2006*, where productive aquifer system is above the blue dotted line (below is brackish water containing more than 500 mg/L of dissolved solids). (c) Estimates of clay content percentages in the Fort Lowell adapted from *Anderson, 1988*.

The heterogeneous aquifer systems of this region are composed of discontinuous, interbedded aquifer and aquitard layers [*Anderson*, 1995]. Aquifer units consist of coarse-grained water-bearing beds, while aquitard lenses act as less permeable confining layers. The distribution and thickness of aquitard clays generally decreases towards the basin edges, but the localized variability of interbedded lenses are complex and thus wells in close proximity can show differences [*Anderson*, 1988; *Mason and Bota*, 2006]. The estimated percentage of fine-grained aquitard material for the Fort Lowell and upper Tinaja Formations (Figure 4.1c & d) in the study area ranges from less than 20% to greater than 80% [*Anderson*, 1988].

Aquifer system deformation is governed by effective stress, i.e. normal stress minus pore pressure, in that elastic deformation occurs when effective stress is beyond a pre-consolidation stress threshold [*K. Terzaghi*, 1925; *Jacob*, 1940; *Burbey*, 2001b]. On the other hand, aquifer system storage capacity is permanently lost if effective stress increases beyond pre-consolidation stress causing inelastic deformation. Moreover, changes in effective stress can modify aquifer-aquitard hydrological properties [*Helm*, 1976; *Rudolph and Frind*, 1991; *Preisig et al.*, 2014]. As a part of successful water management effort, water managers and policymakers need to know whether groundwater declines will induce permanent, inelastic compaction and storage volume loss.

Recent studies making use of interferometric data and groundwater levels improve understanding of the spatiotemporal patterns of deformation and the underlying physical processes [*Amelung et al.*, 1999; *Bell et al.*, 2008; *Cabral-Cano et al.*, 2008; *Chaussard et al.*, 2014; *Reeves et al.*, 2014; *Miller and Shirzaei*, 2015; *Scanlon et al.*, 2015; *Chen et al.*, 2016; *Smith et al.*, 2017]. To begin, the vertical time series of compaction and expansion at monitoring well sites equipped with borehole extensometers are examined. This allows for investigation of the longer-term behavior of the aquifer system in response to groundwater level declines, yet at a lower spatial resolution. Next, high spatiotemporal resolution InSAR data captures surface deformation during a period of groundwater level recovery between 2004 and 2015. An advanced multitemporal InSAR algorithm is applied to large sets of C-Band SAR images acquired by both Envisat and RADARSAT-2 satellites, which operate at a 5.6 cm wavelength. For Envisat, the opposing look angle geometries of the ascending and descending satellite tracks allows for projecting vertical and east-west directional components. To validate the InSAR, results are compared with GPS and extensometer time series. Analysis of the seasonal components of the vertical InSAR displacement time series and hydraulic head levels enables the calculation of elastic skeletal storativity, describing the amount of fresh water an aquifer system produces without inducing irreversible compaction. The long InSAR time series highlights the spatiotemporal evolution of the land subsidence and sheds light on the mechanical properties of the aquifer-aquitard system.

4.2. Data and Methods

4.2.1 Extensometer and Well Data

The broad spatial extent and imperceptible temporal behavior of land subsidence make measurement and monitoring difficult. Since the late 1980's, the United States Geological Survey maintains observation wells equipped with borehole extensometers. Figure 4.1 shows the well locations and associated labels. These wells provide measurements of groundwater levels with an accuracy of 3 mm (private correspondence USGS) (Figure 4.2) at key locations in the city of Tucson [*Cunningham and Schalk*, 2011]. Several wells, B76, C45, D61, WR52, and WR53, exhibit significant long-term declines until the mid-2000s when recovery begins coincident with the intensification of artificial recharge efforts. Water levels at SC17 and SC30 also reflect this increasing trend, yet did not withstand earlier long-term declines.

Borehole extensometers measure compaction and expansion of vertical thickness using a recorder as the land surface moves relative to a anchored plate at the borehole base [*Hanson*, 1989; *Evans and Pool*, 2000]. Thus, compaction is measured from the surface to the anchor platform fixed in less compressible layers and does not measure any compaction deeper than the anchor [*Hanson*, 1989; *Carruth et al.*, 2005]. Extensometer measurements

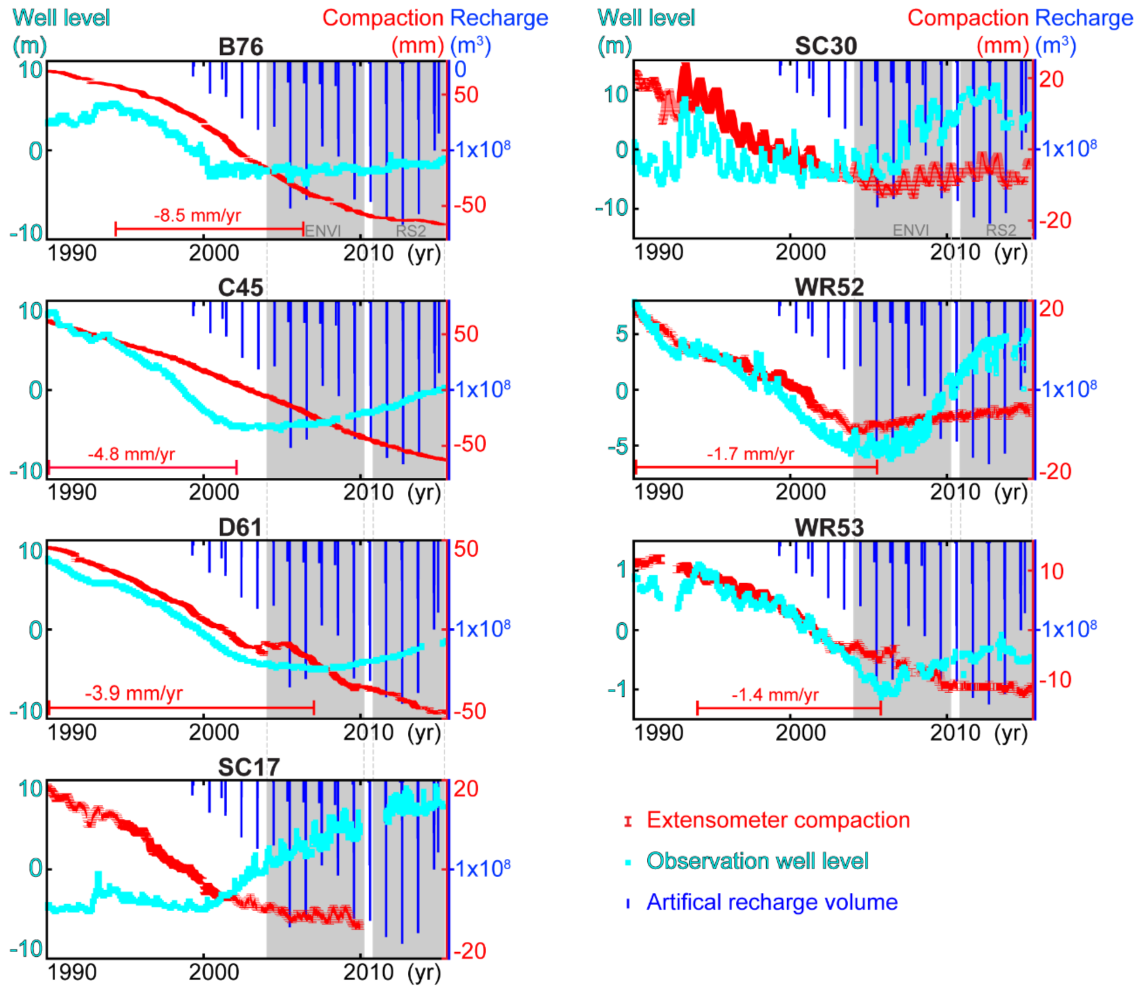

Figure 4.2) Head levels, Compaction, and Recharge. Groundwater levels (cyan) are compared to compaction logged by extensometers (red) and artificial recharge volumes (blue bars). Site-specific intervals of declining water levels are marked with red lines along with the mean compaction rate. The grey shaded areas identify the coinciding Envisat and RADARSAT-2 acquisition intervals.

are accurate to 0.6 mm with a precision of 0.3 ± 0.6 mm ([*Anderson et al.*, 1982] and personal communications, Robert Carruth with USGS, 2017). Compaction rates for intervals exhibiting long-term water level declines are shown for each extensometer site (Figure 4.2). For the five locations with significant persistent drawdowns (B76, C45, D61, WR52, WR52), the mean compaction rate is 4.1 mm/yr. and is as high as 8.5 mm/yr. at site B76. However, even sites with stable, or increasing long-term hydraulic head levels throughout the 1990s (e.g., SC17 & SC30) exhibit compaction (Figure 4.2). This may be due to sustained residual effects of significant drawdowns prior to this study, or perhaps a natural settlement of basin-fill sediment.

4.2.2. InSAR Datasets

InSAR observations offer unprecedented spatial resolution to investigate surface deformation across the Tucson basin. The so-called Wavelet-Based InSAR (WabInSAR) algorithm, an advanced multitemporal InSAR approach [*Shirzaei*, 2013; *Shirzaei and Bürgmann*, 2013], is implemented to analyze multiple sets of SAR images. This includes 24 ascending (11-Jan-2004 to 9-May-2010) and 52 descending (14-Feb-2003 to 10-Sept-2010) orbit track images of the Envisat satellite, and 23 ascending orbit track images from RADARSAT-2 satellite from 30-Oct-2010 to 6-Jun-2015. Figure 4.1 shows the footprint of different SAR frames as well as flight directions. Using this dataset 681 interferograms are generated with spatial and temporal baselines shorter than 300 meters and 3 years, respectively. The effect of topography and the flat earth is calculated and removed using a reference digital elevation model (DEM) and satellite ephemeris data [*Franchioni and Lanari*, 1999]. Elite (i.e. less noisy) pixels are identified using a statistical framework applied to the noise time series estimated through wavelet analysis of the complex phase observations [*Shirzaei*, 2013]. Additional wavelet-based filters are used to adjust for topography correlated atmospheric delay and orbital errors; temporally uncorrelated atmospheric delay is removed with a high-pass filter [*Shirzaei and Walter*, 2011; *Shirzaei and Bürgmann*, 2012]. The algorithm uses a reweighted least squares approach to invert the datasets for LOS displacement time series and linear velocities with sub-millimeter precision.

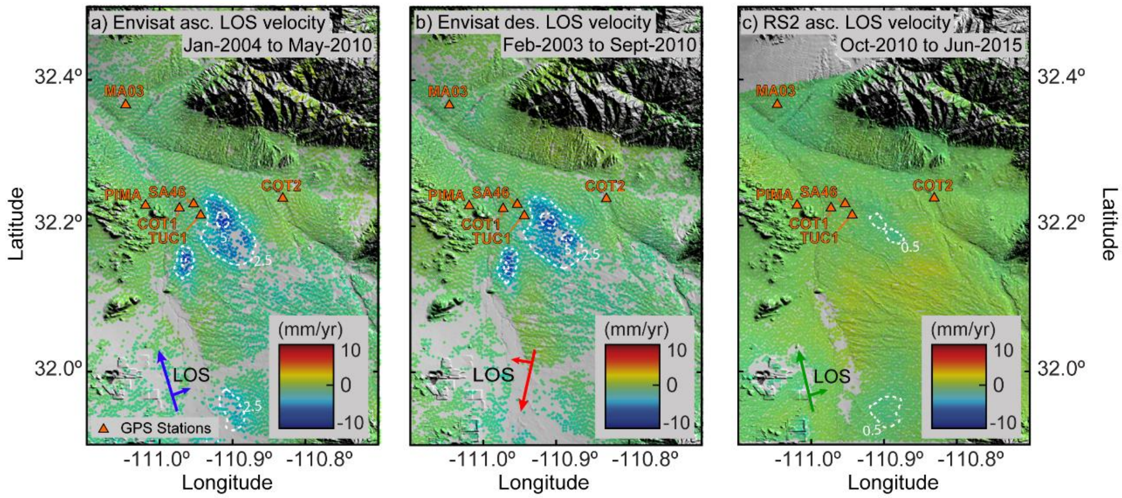

Figure 4.3. Line of Sight Velocity Maps (a) of ascending Envisat track 177 (heading angle 350, incidence 23), (b) descending Envisat track 456 (heading angle 192, incidence 23), and (c) descending RADARSAT2 (heading angle 348, incidence 28). Dashed white lines are velocity contour intervals in mm/yr.

The ascending Envisat velocity map (Figure 4.3a) is characterized by two distinct zones of rapid subsidence to the east and west with LOS rates up to -8.9 mm/yr. for the period 11-Jan-2004 to 09-May-2010. A similar pattern occurs in the descending track for the period 14-Feb-2003 to 10-Sept-2010, where LOS velocities reach -6.3 mm/yr. (Figure 4.3b). This agreement indicates that effect of uncompensated artifacts is negligible and that majority of the signal is vertical. The ascending RADARSAT-2 LOS velocity map shows subsidence up to -1.5 mm/yr. (Figure 4.3c) calculated from 30-Oct-2010 to 6-Jun-2015.

Combining Envisat ascending and descending viewing geometries following the approach detailed in [*Miller and Shirzaei*, 2015], the LOS displacement time series and velocity fields are decomposed into vertical and east-west directional components. To this end, the north-south component of displacement field is considered negligible. Thus, knowing the full geometry (i.e., satellite heading and LOS incidence angles) of SAR acquisitions, the vertical and east-west displacement fields are calculated. Figures 4.4a & b show the corresponding directional components. The map of vertical deformation rate (Figure 4.4a) indicates that the greatest subsidence with a linear rate of -8.2 mm/yr. occurs towards the center of the smaller western zone (location marked by magenta triangle in Figure 4.4a).

The greatest cumulative subsidence of -52.3 mm occurs at the eastern zone (location marked by yellow triangle in Figure 4.4a). No obvious patterns of horizontal velocity are observed in the east-west direction (Figure 4.4b). Next, patterns of the directional times series are examined along a profile (A-A') that crosscuts the major subsidence zones. Noting a steady decline of the land surface in the vertical time series (Figure 4.4c) and an undulation in the east-west direction with a negligible long-term trend (Figure 4.4d), the primary direction of motion is vertical.

Table 4.1. Tucson Aquifer Parameters. Depth is for both well and borehole extensometer. The inelastic skeletal storage coefficient (S_{kv}) and compaction time constant (τ) is for periods of steady water level declines at applicable sites identified in Fig. 4.2. The elastic storage coefficient (S_{ke}) and standard deviation are calculated with Envisat seasonal vertical displacement and head levels. Uncertainties at a 95% confidence interval.

Observation well / extensometer site

	B76	C45	D61	SC17	SC30	WR52	WR53
Site Depth (m)	270	148	314	245	294	246	314
Inelastic period (yr.)	1994-2006	1990-2004	1990-2006	--	--	1990-2006	1994-2005
S_{kv}	$1.09\text{x}10^{-2} \pm 7.31\text{x}10^{-4}$	$4.64\text{x}10^{-3} \pm 2.38\text{x}10^{-3}$	$4.67\text{x}10^{-3} \pm 3.05\text{x}10^{-3}$	--	--	$1.86\text{x}10^{-3} \pm 2.63\text{x}10^{-3}$	$7.95\text{x}10^{-3} \pm 2.27\text{x}10^{-4}$
τ (yr.)	15.0 ± 3.3	2.7 ± 3.8	5.4 ± 2.4	--	--	5.1 ± 1.9	5.1 ± 1.2
S_{ke}	$1.09\ \text{x}10^{-5} \pm 7.91\text{x}10^{-6}$	$5.85\ \text{x}10^{-3} \pm 1.14\text{x}10^{-3}$	$1.00\ \text{x}10^{-2} \pm 1.17\text{x}10^{-3}$	$9.33\ \text{x}10^{-4} \pm 2.03\text{x}10^{-4}$	$4.67\ \text{x}10^{-4} \pm 5.11\text{x}10^{-5}$	$8.05\ \text{x}10^{-4} \pm 1.64\text{x}10^{-4}$	$8.37\ \text{x}10^{-3} \pm 1.61\text{x}10^{-3}$

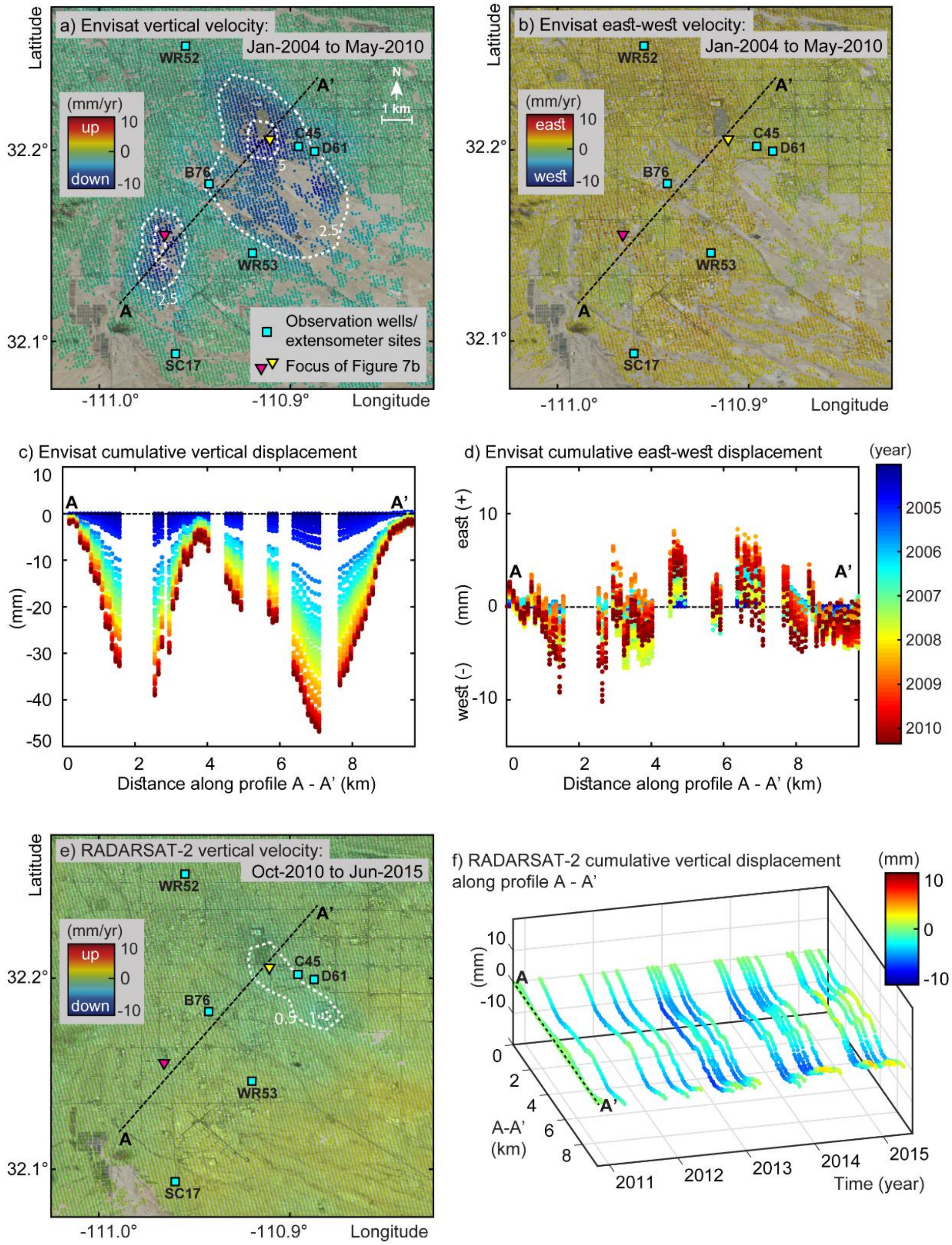

Figure 4.4) Vertical and Horizontal Velocity Maps and Time Series. Envisat imagery from Jan-2004 to May-2010 showing (a) vertical and (b) east-west velocity and displacement time series along A-A' (c & d), as well as for RADARSAT-2 (e-f) from Oct-2010 to Jun-2015. Locations in the western (magenta triangle) and eastern (yellow triangle) subsidence zones are detailed in Figure 4.7b.

Precluded from considering an east-west component for RADARSAT-2 due to the lack of an overlapping descending track, owing to the dominance of the vertical component found in Envisat, the horizontal contribution is assumed negligible to the overall signal. The vertical component is estimated by scaling the time series using the LOS vertical unit vector. The RADARSAT-2 vertical velocity map (Figure 4.4e) exhibits a significantly slower rate during the period 30-Oct-2010 to 6-Jun-2015 with a maximum of -1.7 mm/yr. Figure 4.4f shows the vertical time series along the profile A-A' in which a seasonal oscillation is modulated on a weak long-term subsidence trend.

To validate InSAR results, the 3D displacement field is compared at 6 continuous GPS stations (locations shown in Figure 4.3). Technical advances in GPS positioning associated with data reprocessing [*Desai et al.*, 2011], satellite phase center variation models [*Schmid et al.*, 2007, 2010], and solar radiation pressure models [*Sibthorpe et al.*, 2010] have dramatically improved vertical accuracy [*Argus*, 2012]. For example, such advances in vertical GPS positioning allow for inferring changes in water as a function of time from solid Earth's elastic response to mass loading in California [*Argus et al.*, 2014].

First, to obtain the vertical displacement time series, GPS satellite orbits and a subset of 100 site positions on Earth's surface are determined. These parameters are used to determine the positions of hundreds of sites on Earth's surface using the GIPSY-OASIS algorithms and precise point positioning method [*Zumberge et al.*, 1997; *GIPSY-OASIS*, 2016]. Elastic deformation due to the solid Earth tide, the ocean tides, and the pole tide are removed from the GPS positions. The monthly-averaged GPS vertical displacements presented in Figure 4.5 are estimated with respect to the GPS station COT1, which is used as a local reference for both InSAR and GPS. Comparing the vertical component of InSAR to that of GPS, suggests an overall good agreement between the two independent time series with an average standard deviation of ~3.3 mm. However, only two stations have lengthy GPS time series coincident with the Envisat study duration (Figure 4.5). Inopportunely, stations are peripherally located outside of subsiding zones, thus exhibiting a seasonal signal with an insubstantial long-term trend.

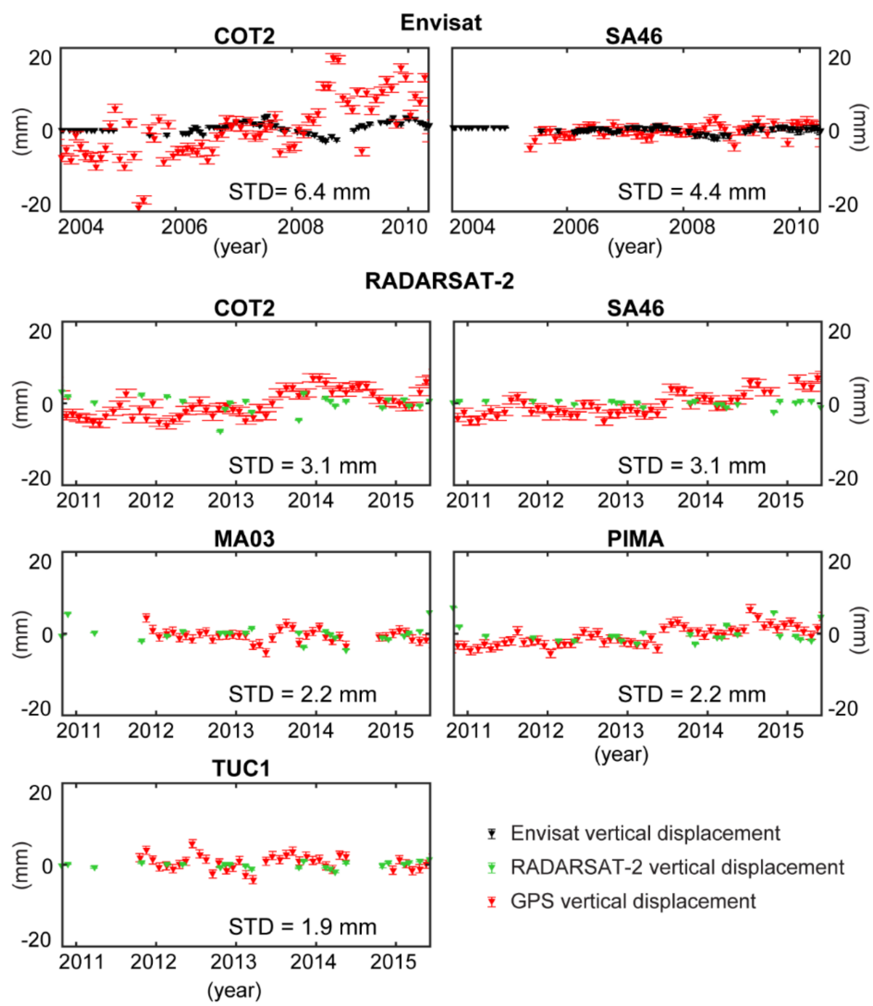

Figure 4.5) InSAR Comparison with GPS. Z-component of monthly GPS time series and vertical InSAR from Envisat and RADARSAT-2. GPS stations are referenced to station COT1. InSAR marker is the average of pixels within 250 meters of GPS station and are referenced to pixels within a 250-meters of COT1.

For additional validation, vertical compaction at 7 borehole extensometers is also compared to the InSAR vertical displacement time series (locations in Figure 4.1a). Extensometer site WR53 is considered as the reference for both datasets to localize the reference frame. Although extensometers sites B76 and C45 show more compaction than that of InSAR (Figure 4.6) and some phase differences occur at station SC30, there is generally good agreement between dataset measurements with an average standard deviation of ~3.1 mm. The long-term differences are likely due to measurement scope, as InSAR estimates are an average of pixels within a 250-m diameter of the site (pixels are 80 m^2) and extensometers diameters are less than 16 cm. Moreover, any N-S oriented horizontal motion directly affects extensometer measurements but has a negligible effect on InSAR observations.

Figure 4.6 next page) Comparison of Extensometer and Vertical InSAR Time Series. Both referenced to station WR53 and InSAR pixels are referenced to pixels within 250 meters of an extensometer site. The standard deviations of the difference between time series are in each box. The agreement suggests compaction below extensometer anchor is minimal at most sites.

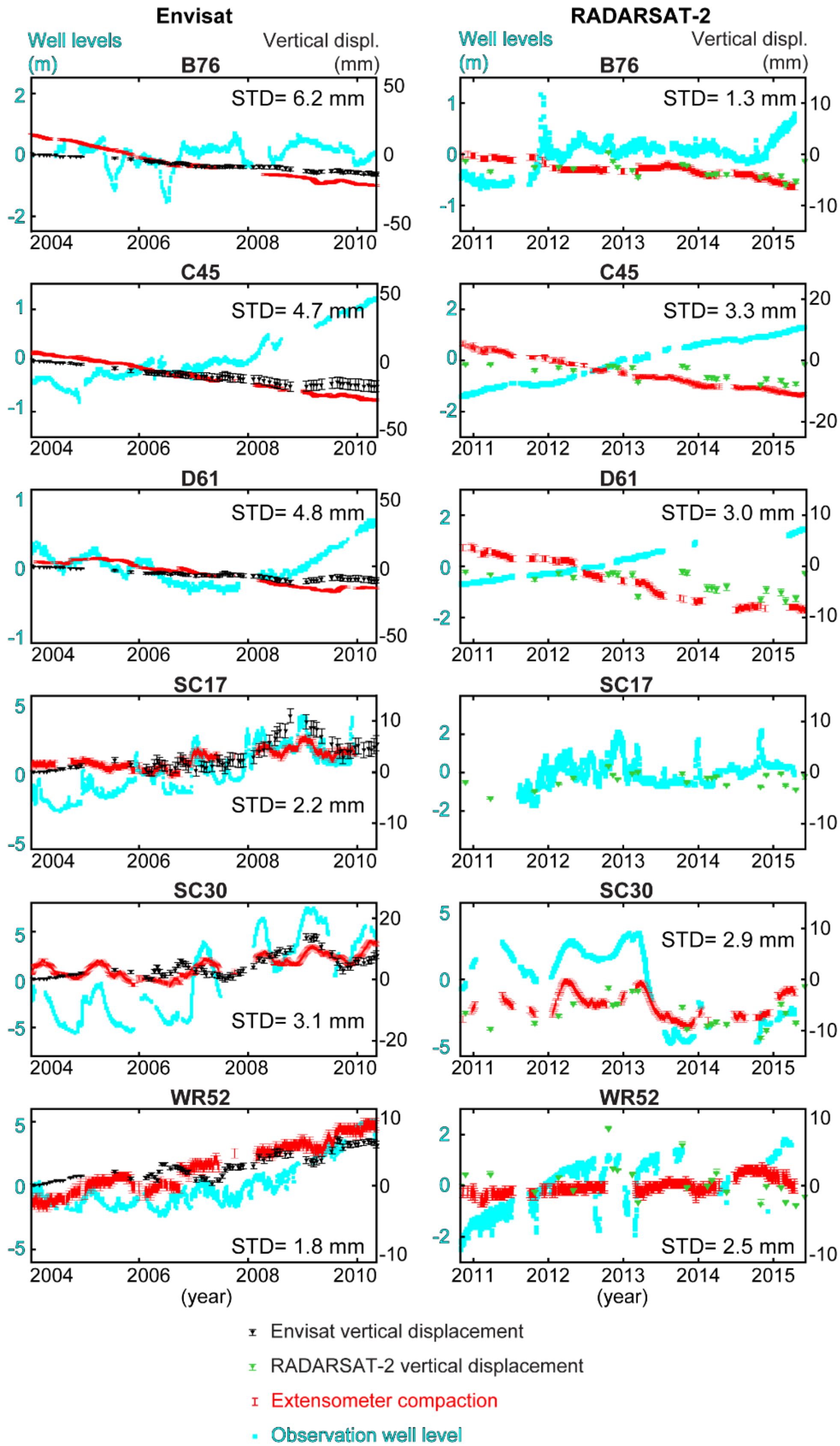
Envisat
RADARSAT-2
Well levels (m)
Vertical displ. (mm)
B76
STD= 6.2 mm
STD= 1.3 mm
C45
STD= 4.7 mm
STD= 3.3 mm
D61
STD= 4.8 mm
STD= 3.0 mm
SC17
STD= 2.2 mm
SC30
STD= 3.1 mm
STD= 2.9 mm
WR52
STD= 1.8 mm
STD= 2.5 mm
(year)
Envisat vertical displacement
RADARSAT-2 vertical displacement
Extensometer compaction
Observation well level

4.3 Hydrological Implications

4.3.1 Aquifer Parameters

Specific storage of a confined aquifer, S_s, is the amount of water produced as pore pressure declines, as the aquifer system compresses, and water expands [*Theis*, 1935; *Jacob*, 1940; *Burbey*, 2001a];

$$S_s = \rho_w g(\alpha + n\beta) \tag{4.1}$$

where, ρ_w is the density of water, g is gravitational acceleration, α is aquifer compressibility, β is water compressibility, and n is porosity. This relates to the principle of effective stress, $\sigma' = \sigma - p$, which is equal to the total overburden stress σ less pore pressure p, and is the foundation of the coupled relationship of changes in hydraulic head levels and deformation in one dimension [*K. Terzaghi*, 1925]. Assuming a constant overburden load, $\Delta p = -\Delta\sigma' = \Delta h \rho_w g$, where Δh is the change in hydraulic head [*Poland and Davis*, 1969], aquifer compressibility is given by:

$$\alpha = -\frac{\Delta b}{\Delta\sigma' b_o} = \frac{\Delta b}{\Delta h \rho_w g b_o} \tag{4.2}$$

where Δb is the compaction and b_o is initial thickness [*Jacob*, 1940]. By incorporating Equation (2) with Equation (1) and assuming water compressibility is negligible relative to aquifer system deformation, the storage coefficient S_k is defined as:

$$S_k = S_s b_o = \frac{\Delta b}{\Delta h} \tag{4.3}$$

This dimensionless coefficient describes the volume of fluid released from an aquifer system area with a change in hydraulic head level. The skeletal storage can be separated into elastic S_{ke} and inelastic S_{kv} skeletal storage coefficients based on whether effective stress is greater than a pre-consolidation stress σ'_{max} threshold [*Hoffmann et al.*, 2003b]:

$$S_k = S_{ke} + S_{kv}$$

$$S_k = \begin{cases} S_{ke} \text{ for } \sigma' < \sigma'_{max} \\ S_{kv} \text{ for } \sigma' \geq \sigma'_{max} \end{cases} \tag{4.4}$$

Aquifer storativity is likely permanently lost when effective stress increases beyond pre-consolidation stress and deformation is inelastic, i.e., mostly interbeds compact. The lateral distribution of clay lenses and variation in thicknesses are difficult to derive from sparse bore logs, yet can contribute to differential subsidence patterns. Thus, determining coefficient values in relation to historical deformation and water head levels is a priority for understanding and modeling the behavior of aquifer systems.

The dimensionless elastic skeletal storage coefficient S_{ke}, an important parameter for groundwater flow models [*Riley*, 1969; *Green and Wang*, 1990], describes the volume of fluid removed or retained as the hydraulic head level fluctuates over an aquifer area without causing inelastic deformation. This coefficient represents the elastic behavior of both the aquifer and aquitard units [*Hoffmann et al.*, 2001; *Liu and Helm*, 2008]. To estimate this parameter:

$$S_{ke} = \frac{\Delta b_p}{\Delta h_p} \tag{4.5}$$

where Δb_P and Δh_P are the elastic, seasonal components of the vertical displacement and water level time series, respectively.

To estimate the time series of seasonal vertical displacement Δb_p and hydraulic head level Δh_p, the time-frequency components of the time series are deconstructed via continuous wavelet transform following *Miller & Shirzaei* [2015]. Wavelets allow analyzing signals with nonstationary components and are capable of decomposing the signal into its building block based on its localized frequency properties [*Christopher Torrence*, 1998].

Fluctuations occurring within 0.5 to 1-year periods are identified, which are then isolated and reconstructed into Δb_p and Δh_p. This assumption is made to be consistent with the natural seasonal recharge/discharge cycle of the aquifer system. Moreover, given the slow infiltration rate of the recharged fluid and temporal sampling of the SAR acquisitions being 1-2 months, shorter periods may not be reliable. Also, regarding hydraulic head and extensometer data, signals with shorter periods can be attributed to tidal effects, which need to be avoided. The mean range of seasonal vertical displacement is 5.2 mm and the maximum range is 11.5 mm for the Envisat period. The range increases during the RADARSAT-2 period with a mean range of vertical seasonal displacement of 8.4 mm and a maximum range of 17.4 mm. Wavelet analysis is performed on the well level time series coinciding with the Envisat period, where the mean range of seasonal water levels is 1.93 m and the maximum range of 6.36 m occurs at the well SC30.

To estimate elastic skeletal storage coefficient and associated uncertainties, a constrained least squares algorithm [*Mikhail et al.*, 1978] and an iterative bootstrapping scheme are implemented. During the bootstrapping step, the least squares estimation step is repeated 500 times, and in each iteration, 80% of the time steps are randomly selected for the calculation. This results in a robust statistical estimation and a probability distribution function for elastic skeletal storage. The elastic storativity values are calculated for the Envisat period and the associated uncertainties in 95% confidence interval, which are displayed in Table 2.1, with values ranging from 1.09×10^{-5} to 1.00×10^{-2}. Using a smooth spline interpolation approach, the estimated elastic storage coefficients are interpolated on a grid with cell resolution of 5 m (Figure 4.7a). The elastic storage coefficient is generally smaller towards the west on the resulting map, which correlates to areas of the basin with higher percentages of fine-grained material (Fig 4.1 c&d). In conjunction with high-resolution maps of surface deformation obtained from InSAR, availability of such maps allows approximating head level changes where well data are not available. Moreover, they can be used to inform hydrological models.

The dimensionless inelastic skeletal storage coefficient describes the volume of fluid expelled from cumulative aquitard layers in a compacting aquifer system volume when stressed beyond the pre-consolidation stress level [*Hoffmann et al.*, 2003a]. The inelastic skeletal storage coefficient can be several orders of magnitude greater than the elastic storage coefficient [*Burbey*, 2001b]. A temporal lag described by a compaction time constant occurs due to delayed equilibration of aquitard head levels to neighboring aquifer head levels. Ignoring the elastic changes in aquifer compaction and head levels, the following relationship can be used [*Hoffmann et al.*, 2003a];

$$\frac{\Delta b_l}{\Delta h_l} = S_{kv}\left(1 - \frac{8}{\pi^2} e^{\frac{-\pi^2 t}{4\tau}}\right) \tag{4.6}$$

where, Δb_l is the compaction time series, Δh_l is the long-term head level time series, τ is the compaction time constant, and S_{kv} is the inelastic skeletal storage coefficient [*Bell et al.*, 2008]. These parameters are estimated using a Genetic Algorithm, a nonlinear optimization algorithm inspired by the principles of natural selection, where a population of solutions is stochastically improved by iteratively comparing fitness to a cost function [*Shirzaei and Walter*, 2009]. To evaluate Equation (4.6), only a subset of extensometer data and associated wells are used. First, only sustained periods (~1990-2005) of declining well levels at each applicable site (B76, C45, D61, WR52, WR53) are considered, thus excluding wells with stable or rising levels (SC17, SC30). Second, these periods with declining well levels are below historic lows, thus exceeding the pre-consolidation stress. This assumption is reasonable, given the long-term decline in head levels for the entire period that affected wells are monitored in the dataset. Moreover, this approach is tested successfully elsewhere [*Bell et al.*, 2008]. The alternative approach would be to use a protracted time series of head levels capturing the entire period of pumping activity to establish the historical low as pre-consolidation level [*Smith et al.*, 2017]. Such an approach, however, requires high resolution head level measurements, going back several decades, which are not available. Comparing the vertical compaction time series and water level time series, the inelastic storage coefficient ranges from 1.86×10^{-3} to 1.09×10^{-2}, and the compaction time constant from 2.7 to 15.0 years (Table 4.1). Uncertainties are estimated to a 95% confidence interval for both parameters [*Shirzaei and Walter*, 2009]. Disparate values between sites are expected due to the varied spatial distribution of clay content, yet may also be attributed to differences composition and bedrock structures.

4.3.2. Aquifer Storage Loss

To investigate the effects of inelastic compaction prior to 2005 on the storage capacity of the aquifer system, sites are identified within and nearby zones of subsidence in the basin (B76, C45, D61, WR52, WR53). The mean inelastic storage coefficient value ($\overline{S_{kv}}$ $= 6.01 \times 10^{-3}$), the mean hydraulic head level time series $\overline{\Delta h}$, and the surface area of the subsiding zones, $A = 104\ km^2$, are used to estimate the lost storage volume ΔV;

$$\Delta V = \overline{S_{kv}}\overline{\Delta h} b_o A \tag{4.7}$$

where b_o is the estimated initial thickness of the fine-grained, aquitard layers. To estimate b_o, the aquifer system column thickness is represented by the average observation well depth of the nearby sites (258 m). Then the percentage of compressible, aquitard material of the column is estimated, ranging from low (20%) to high (30%). This percentage range is selected based on a conservative interpretation of the maps of the fine-grained material of the Fort Lowell and Upper Tinaja bed aquifer system formations (Figure 4.1 c&d) [*Anderson*, 1988]. We choose a basin-scale estimate because fine-grained material thicknesses, which vary due to an uneven basement, fault offsets, and aquitard lens distribution, can affect localized compaction and we are interested in the overall pattern. Also, considering a range of compressible thicknesses is better to account for the variable, complex heterogeneity of aquitard layers in the basin. This estimation of storage capacity lost via compaction of fine-grained sediments ranges from 2.81×10^8 m^3 to 4.21×10^8 m^3 (or 2.28×10^5 to 3.41×10^5 acre-feet), which is a 2.7% to 4.1% storage volume loss. In terms of the TAMA conceptual groundwater budget, the amount of storage volume lost approximates the four to six years of pumpage outflow from the entire area [*Mason and Bota*, 2006]. A permanent reduction in storage volume has important implications for future withdrawals. For example, using the values from the previous calculation and pumping the same volume at the same rate in the future, the groundwater level would drop an additional 0.37 meters (1.2 feet). It is also important to note that from 1940 to 1995, water table levels declined from 30 to 60 meters in the Tucson valley [*Mason and Bota*, 2006] and this study does not capture volume losses preceding 1990.

4.3.3. Residual Compaction

Subsidence rates decelerate over time with an exponential decay pattern representing delayed compaction of slow draining aquitards [*K. Terzaghi*, 1925]. Aquifer systems with thick aquitard lenses may enter a state of nearly perpetual lagged equilibration if the effects of past pumping are sustained as a subsequent pumping period begins [*Pavelko*, 2004]. Deceleration patterns of two locations in the heart of each urban subsidence zone are highlighted (marked by triangles in Figure 4.4). The vertical InSAR displacement time series obtained from Envisat and RADARSAT-2 are combined with negligible displacement assumed between 09-May-2010 and 30-Oct-2010 (Figure 4.7b). Vertical deformation significantly slows by 2009, supporting this assumption of negligible deformation between dataset periods, and is concurrent with recovering well levels (Figure 4.2). We model Terzaghi's relationship as an exponential function of time, $\Delta b = Me^{(-Bt)-1}$, where Δb is the vertical deformation time series, M is the magnitude of the aquifer subsidence response, and B is the decay coefficient ranging [-1,0]. The Genetic Algorithm is used to estimate optimum coefficients M and B for the selected locations in each subsidence zone. The magnitude response of the larger eastern zone is 54.4 mm and the decay coefficient is -0.35; the smaller western zone is similar with a magnitude response of 54.8 mm and decay coefficient of -0.30.

Such large decay coefficients are indicative of a relatively high vertical hydraulic conductivity K_v for the hydrologic units, meaning the duration of the delay in equilibrating neighboring aquifer/aquitard units is relatively short. Vertical hydraulic conductivity relates to delayed compaction by the following equation [*Riley*, 1969; *Smith et al.*, 2017],

$$\bar{\tau} = \frac{\overline{S_{ke}}}{K_v} \left(\frac{\overline{b_o}}{2}\right)^2 \tag{4.8}$$

Where $\bar{\tau}$ = 6.6 years, the mean of the previously estimated compaction time constants, which is supported by the observation of recovering hydraulic head levels beginning ~2003 and subsidence cessation in the center of the subsidence zones ~2009. Note that during this period of recovering water levels, inelastic deformation is negligible and the system is dominated by elastic, seasonal behavior. Thus, the mean elastic skeletal storage coefficient is used, $\overline{S_{ke}}$= 1.79 x10^{-3}, as are low and high (20-30%) estimates of $\overline{b_o}$, the thickness of the fine-grained, aquitard layers.

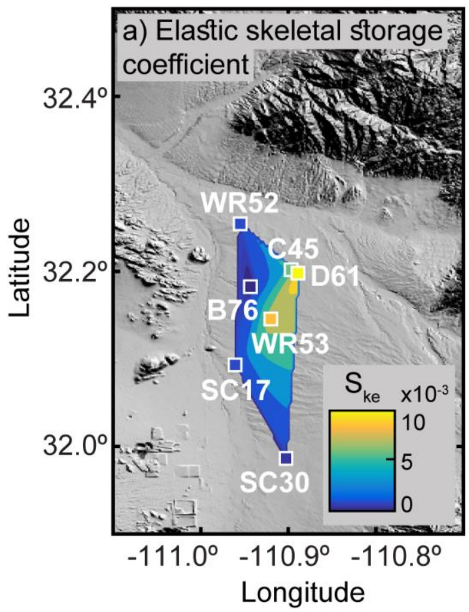

Figure 4.7 Analysis of Aquifer Characteristics (a) Elastic skeletal storage coefficient values. Values in between well sites estimated with spline interpolation (built in MATLAB function). b) Continuous time series of maximum subsidence locations (marked in Figure 4.4a, b, c with yellow triangles, respectively). The modeled relationship follows Terzaghi's exponential decay relationship for slow draining aquitards within a 95% confidence interval, assuming negligible deformation in between datasets. US Drought Monitor Intensity Classification drought severity via weekly average for Tucson.

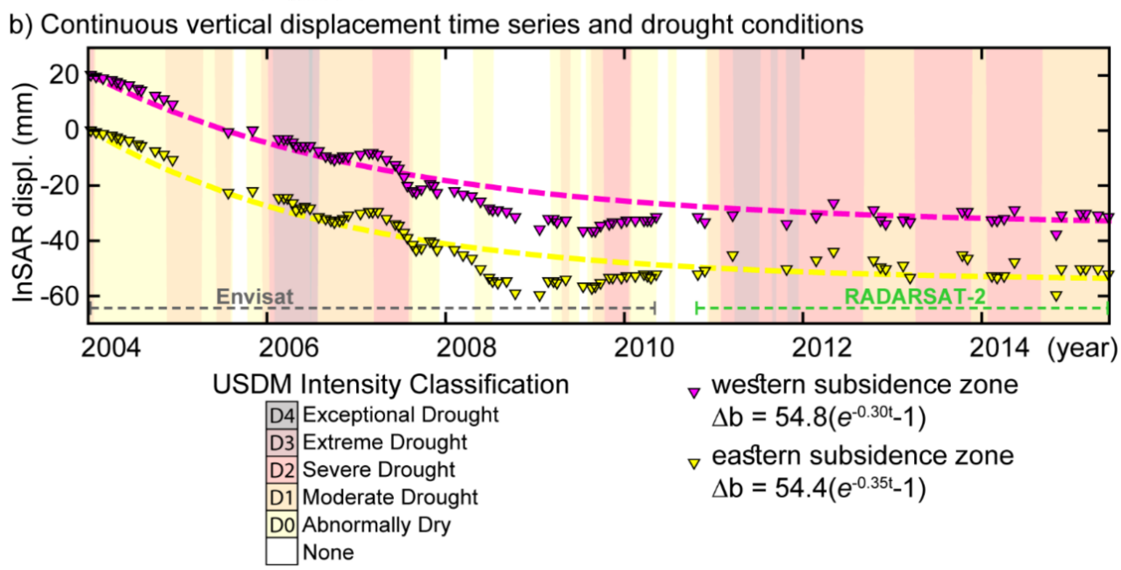

This estimate is based on geologic maps outlining the approximate percentage clay content of formations, which is simplified into one problem for the overall aquifer system column in the basin (Figure 4.1b & c) [*Anderson*, 1988]. A range of 4.4x10^{-4} and 9.8x10^{-4} m/day is estimated for vertical conductivity. This is compared to the TAMA Upper Santa Cruz groundwater flow model, where the vertical hydraulic conductivity values for 20%-40%

and 40-60% fine-grained material are 7.9×10^{-4} m/day and 5.2×10^{-4} m/day respectively, consistent with estimates from this study. However, this estimate is much faster than estimates of 1.67×10^{-8} to 2.48×10^{-6} m/day for San Joaquin Valley [*Sneed*, 2001]. The history, composition, and structure of the Tucson and San Joaquin aquifer systems are istinct, yet several observations support a disparity between locales. Drillers' logs samples from San Joaquin Valley indicate that thick clay layers have already drained following historical pumping, thus current pumping mostly affects thin aquitard layers resulting in lower hydraulic conductivities [*Faunt et al.*, 2009]. Values in the San Joaquin Valley have reduced by a factor as great as 6 times the original calculated laboratory values [*Williamson et al.*, 1989]. Furthermore, the lack of an uplift signal in Tucson associated with recovering heads suggests diffusion is quickly assimilating water into the system. However, the difference in hydraulic conductivity values between sites is also partly due to the first order assumption of a single layer aquifer system. A multilayered approach which accounts for individual interbed stratigraphy is required to capture complex aquitard lens distribution and provide a more accurate estimation. Even with a simplified model using generalized stratigraphy, the results provide information that can aid water management.

4.4 Discussion and Conclusions

Inherent limitations of coherent imaging systems, such as SAR interferometry, are sensitivity to the land surface cover change and poor temporal sampling rate. However, the data from Sentinel-1A/B satellites [*Shirzaei et al.*, 2017] and future SAR satellites such as NISAR (NASA-ISRO SAR mission) will offer an improved sampling rate as low as 6 days. The unparalleled spatial resolution and coverage provided by InSAR measurements are invaluable for monitoring the regional scale of land subsidence (Table 4.2). More expensive and difficult to improve is the spatial distribution of observation wells, which provide an in-situ measurement of the groundwater head level. Regions with sparse reliable well data must rely on alternative strategies, such as local gravity surveys and regional GRACE storage change estimates [*Scanlon et al.*, 2015]. Borehole extensometers and GPS often offer robust temporal sampling but are limited to point locations. Also, extensometer measurements can be sensitive to temperature, humidity, and soil moisture content in shallow zones. To obtain a robust perspective of aquifer properties and mechanics, the approach of analyzing multiple datasets helps minimize the impact of individual dataset limitations.

Table 4.2: Methods of Monitoring Deformation.[*Anderson et al.*, 1982; *Cunningham and Schalk*, 2011; *D.M. et al.*, 2011; *Argus*, 2012]. Resolution means the spatial extent of the ground surface that is covered by individual measurement. Spatial coverage refers to the extent of monitoring network or dimension of satellite imagery.

	Resolution	Spatial coverage	Temporal sampling	Accuracy	Precision
Extensometer	point	10's m	daily	~ 0.6 mm	0.3 ± 0.6 mm
InSAR	10's m x 10's m	100's km	< 30 days	~ 5 mm	< 1 mm/yr.
GPS	point	10's - 1000's km	daily	~ 4 mm	0.1 mm

In this study, the time series of surface deformation is investigated across the Tucson Valley in conjunction with measurements of groundwater levels at several observational wells. During periods of rapid subsidence from 1990 through the mid-2000s, compaction of fine-grained material is as fast as 8.5 mm/yr., which results in permanent storage volume losses of 2.7% to 4.1%. The subsidence significantly slows throughout the valley by 2004, coincident with the implementation of artificial recharge efforts. Following, a relatively brief interval of residual compaction, subsidence nearly ceased by 2015. This rapid recovery likely stems from unusually high vertical conductivity in the valley, contributing to the success of water management plans by reducing the duration of delayed compaction. Estimated aquifer mechanical properties, including elastic and inelastic storage, and lateral variability are also observed in the valley. The heterogeneity of clay content, thickness, and distribution of lenses significantly affects the spatiotemporal subsidence patterns observed in Tucson.

Other regions with rising water levels exhibit uplift of the land surface due to poroelastic aquifer rebound. For example, in the Taipei Basin, Taiwan, rebound is 10% of the magnitude of earlier subsidence rates [*Chen et al.*, 2007] and in the Santa Clara Valley, California, *Chaussard et al*. [2014] describes uplift up to 4 mm/yr. *Shirzaei et al.* [2017] also report uplift in the Santa Clara Valley up to 8mm from August 2015 through September 2015. Precipitation during this period was negligible and the observed uplift is attributed to a combination of reducing pumping, a shift to using treated surface water and increasing the allocation of imported water. Lastly, in Phoenix, Arizona, *Miller and Shirzaei,* [2015] characterize a zone of uplift reaching 6 mm/yr. located near underground storage facilities designed to replenish depleted aquifer systems (refer to Chapter 2). Conversely, Tucson, Arizona lacks a long wavelength uplift pattern associated with the managed recharge program. High vertical conductivity values, may account for the lack of an uplift zone in Tucson by allowing faster diffusion of recharged fluid. The type of recharge apparatus may also have an impact, as Tucson generally employs spreading basins relying on infiltration rather than underground storage facilities that penetrate deeper.

Interestingly, the arrest of subsidence in metropolitan Tucson occurs during a drought. In Figure 4.7b, displacement data and models are superimposed on a drought intensity chart for the Tucson area. The weekly US Drought Monitor (USDM) intensity classification scheme and categorical statistics are based on the Palmer Drought Severity Index, Climate Prediction Center Soil Moisture Model Percentiles, USGS Weekly Streamflow Percentiles, Standardized Precipitation Index, Objective Drought Indicator

Blends Percentiles, and numerous supplementary indicators [*Svoboda et al.*, 2002]. The USDM intensity classification categories increase in intensity from abnormally dry to exceptional drought (D0-D4), considered for the Tucson urban area (918 km^2). Tucson drought conditions fluctuated in severity since 2000 and intensified in 2011, which is common in a historical context [*Morehouse et al.*, 2002]. Decelerated subsidence despite worsening drought is a testament to thoughtful groundwater management. Since 1996, artificial recharge efforts have added $3.51x10^9$ m^3 ($2.8x10^6$ acre-feet) to aquifer storage (private correspondence AWDR), which is greater than 45 years of pumpage at the current rate of the conceptual model [*Mason and Bota*, 2006]. Conservation and recharge efforts help the city reduce aquifer depletion in subsidence zones and store water for the future. Considering the fact that water usage in 2013 was at the same level as 1989 [*Megdal and Forrest*, 2015], and the Tucson population projected to increase, continued conservation efforts are vital. Drought-resilience improved by storing CAP canal deliveries, which continue despite declines in total water storage in the Colorado River Basin [*Scanlon et al.*, 2015]. However, future CAP deliveries are dependent on conditions in the water-stressed Colorado River Basin. In the case of a shortage, future deliveries and recharge efforts are at risk and overexploitation of groundwater will resume [*Castle et al.*, 2014]. Careful study of new satellite data will aid in identifying zones susceptible to subsidence and storativity changes for Tucson as conditions change.

This chapter is adapted from:

M. M. Miller, M. Shirzaei, D. Argus, Aquifer Mechanical Properties and Decelerated Compaction in Tucson, Arizona. *J. Geophys. Res. Solid Earth* (2017), doi:10.1002/2017JB014531.

CHAPTER 5: ELASTIC RESPONSE OF AQUIFER SYSTEM TO 2010-2011 CANTERBURY EARTHQUAKE SEQUENCE, NEW ZEALAND

Abstract: During the 2010 to 2011 Canterbury earthquake sequence, Christchurch, New Zealand, experienced loss of life, unprecedented liquefaction, and devastation to infrastructure. Hydrogeological effects included damaged wells and pumping mechanisms, instantaneous and sustained groundwater fluctuations, and evidence of decreased aquifer transmissivity and permeability in response to the events. As porous solids deform, fluid pressure changes, and flow is affected in response to stress. Groundwater systems exhibit complex responses to static and dynamic stresses associated with earthquakes and these observations are possible indicators the aquifer properties were affected. One of these properties, the elastic storage coefficient, represents the volume of water released or absorbed per unit area of the aquifer with a unit change in the hydraulic head due to elastic processes. In this study, a combination of surface deformation data obtained from interferometric synthetic aperture radar (InSAR) and groundwater level data are used to explore the possible variations of elastic skeletal storativity because of the 2010 to 2011 Canterbury earthquake sequence, Christchurch New Zealand.

5.1 Background

The 2010 to 2011 Canterbury earthquake sequence, Christchurch, New Zealand, occurred on previously unmapped faults starting on September 4, 2010, with a M_w 7.1 event, followed by three large events: M_w 6.2 on February 22, 2011, M_w 6.0 on June 13, 2011, and offshore M_w 5.9 on December 23, 2011 [*Atzori et al.*, 2012; *Bannister and Gledhill*, 2012; *Quigley et al.*, 2012]. As a result, the city of Christchurch experienced loss of life, unprecedented liquefaction [*Cubrinovski et al.*, 2011; *Quigley et al.*, 2013], lateral spreading [*Cubrinovski et al.*, 2012], instantaneous and sustained groundwater fluctuations [*Cox et al.*, 2012; *Gulley et al.*, 2013], and evidence of decreased aquifer transmissivity and permeability in response to the events [*Rutter et al.*, 2016]. Wells and pumping mechanisms were also damaged, which poses a threat to the city of Christchurch water supply [*Gulley et al.*, 2013].

Groundwater systems exhibit complex responses to static and dynamic stresses associated with earthquakes [*Roeloffs*, 1996; *Manga and Wang*, 2007]. Static stress stems from fault offset and is most significant in the near and intermediate distances [*Manga and Brodsky*, 2006]. Many co-seismic, time-dependent hydrological responses are constrained spatially by the volumetric strain field [*Zhou and Burbey*, 2014] and are also determined by the faulting style [*Muir-Wood and King*, 1993]. Furthermore, the early post-seismic deformation can also be attributed to pore-pressure changes due to co-seismic events [*Jónsson et al.*, 2003]. On the other hand, the dynamic stress changes due to the passage of seismic waves can impact the far field [*Manga and Brodsky*, 2006]. Phenomena attributed to dynamic strain changes include sustained co-seismic changes to groundwater levels [*Roeloffs*, 1998], permeability changes in the shallow crust [*Rojstaczer et al.*, 1995; *Elkhoury et al.*, 2006; *Manga et al.*, 2012], and breaching of confining layers to hydrologically connect aquifers [*Wang, C., Wang*, 2004; *Wang et al.*, 2016] and new springs [*Manga et al.*, 2016; *Wang et al.*, 2017]. Moreover, the maximum distance of liquefaction occurrence increases with earthquake magnitude [*Papadopoulos and Lefkopoulos*, 1993].

As porous solids deform, fluid pressure changes, and flow is affected in response to stress. Poroelastic theory describes the coupling of differential stress, strain, and pore pressure, which are modulated by material properties [*Biot*, 1941; *Rice and Cleary*, 1976; *H.Wang*, 2000]. One of these properties, the elastic storage coefficient, represents the volume of water released or absorbed per unit area of the aquifer with a unit change in the hydraulic head due to elastic processes [*Jacob*, 1940; *Cooper*, 1966]. This parameter can be determined through laboratory experiments [*Riley*, 1969; *D.M. et al.*, 2011] or derived from deformation and well level observations [*Miller and Shirzaei*, 2015; *Miller et al.*, 2017]. Elastic skeletal storativity S_{ske} is estimated by comparing the recurring, elastic oscillations in vertical deformation data Δb and hydraulic head levels Δh, using the relation: $\Delta b = S_{ske}\Delta h$. In this study, a combination of surface deformation data obtained from interferometric synthetic aperture radar (InSAR) and groundwater level data are used to explore the possible variations of elastic skeletal storativity because of the 2010 to 2011 Canterbury earthquake sequence, Christchurch New Zealand.

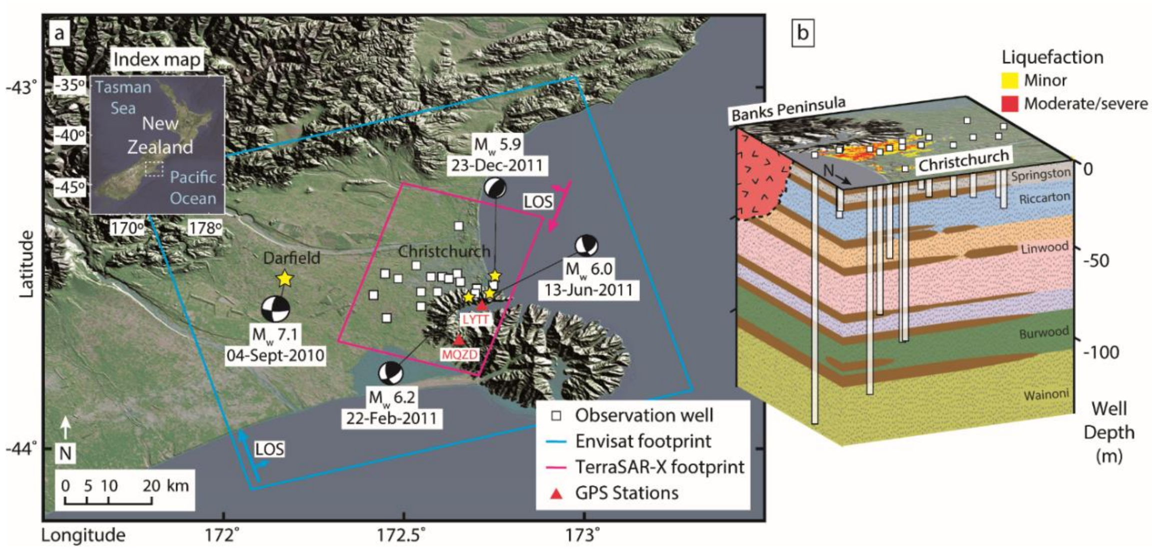

Figure 5.1. Study Area Overview in Lower Hutt, New Zealand. (a) SAR Satellite footprint polygons for ascending Envisat (blue, azimuth = 349º, incidence angle = 23º) and descending TerraSAR-X (magenta, azimuth = 196º, incidence angle = 44.5º). Locations and focal mechanisms of four largest earthquakes are yellow stars/beach balls. (b) Liquefaction map and generalized cross-section. Wells are screened within various aquifer units and confined by aquitards (brown) that thin landwards. Unit thicknesses, lenses, and discontinuities are interpreted and not to scale.

5.2 Geologic Setting

The Canterbury Plains are flanked by the Alpine Fault and active strike-slip regimes to the west, and the Marlborough region to the northeast, which accommodates much of the plate motion between the Pacific and Australian plates [*Wallace et al.*, 2007]. The Canterbury earthquakes are thought to be related to intraplate tectonic stresses in the upper crust rather than plate boundary kinematics [*Sibson et al.*, 2011]. Although faults and folds were identified via seismic reflection prior to the emergence and surface rupture of the Greendale fault in 2010 [*Jongens et al.*, 2012], neither the Greendale fault nor blind structures related to the sequence were previously mapped [*Beavan et al.*, 2012]. Bounded to the west by the Southern Alps, the Canterbury Plains (Figure 5.1a) contain a sequence of amalgamated alluvial fans of Mesozoic Greywacke [*Brown et al.*, 1988]. Quaternary periods of glaciation and sea level regression led to deposition of alluvial and fluvial gravel aquifers, alternating with periods of sea-level transgression and glacial retreat, in which confining marine aquitard layers were deposited inland [*Forsyth et al.*, 2008]. Thus, the coastline at times was closer to the mountains and at times farther than the present coastline. Above a basement of greywacke, an alternating sequence of confined aquifers and confining aquitard layers extend to a depth of 300-500 meters and is topped by a shallow unconfined aquifer where the water table is near the land surface. The thickness of the confining units increases seaward, while permeability increases landward due to gravel sorting and enhanced recharge by influent seepage [*Wilson*, 1973].

Table 5.2. Christchurch Well Information, Location, and Distance from Earthquakes

Well ID	Long.	Lat.	Depth (m)	Aquifer name	Well distance from the epicenter (km)			
					Sept-04	*Feb-22*	*Jun-13*	*Dec-23*
M36/4886	172.55	-43.61	9.0	n/a	10.6	10.8	10.4	11.1
M36/4804	172.45	-43.64	12.0	n/a	12.3	7.2	8.0	13.5
M36/4741	172.59	-43.56	12.4	Springston	10.7	14.2	13.3	10.4
M35/5560	172.58	-43.52	21.0	Riccarton	8.7	14.2	13.0	7.8
M35/3614	172.53	-43.49	24.5	Riccarton	6.5	13.2	11.9	5.1
M36/4740	172.59	-43.56	27.2	Riccarton	10.7	14.2	13.3	10.4
M35/1079	172.49	-43.53	29.3	Riccarton	1.2	7.7	6.3	1.1
M36/4018	172.54	-43.57	29.5	Riccarton	7.5	10.3	9.5	7.6
M35/1080	172.45	-43.51	30.0	n/a	2.5	7.6	6.3	2.7
M35/2565	172.63	-43.53	30.4	Riccarton	12.7	17.6	16.5	11.9
M36/1160	172.70	-43.57	30.8	Riccarton	18.8	22.3	21.5	18.3
M36/5325	172.70	-43.56	33.0	Riccarton	19.0	23.0	22.1	18.4
M36/0217	172.42	-43.57	40.5	n/a	6.5	0.7	1.1	7.9
M35/2564	172.63	-43.53	55.4	Linwood	12.7	17.6	16.5	11.9
M35/3779	172.65	-43.51	82.9	Linwood	14.6	20.0	18.8	13.8
M35/0846	172.65	-43.39	87.5	n/a	21.9	28.8	27.4	20.6
M35/5157	172.61	-43.52	99.5	Burwood	11.3	16.5	15.4	10.4
M35/2081	172.66	-43.54	125.8	Wainoni	15.1	19.7	18.7	14.5
M36/5895	172.75	-43.55	138.0	Wainoni	22.6	26.7	25.8	21.9

The aquifer system stratigraphy is heterogeneous and thicknesses of aquifer and aquitard units can vary and layers can be discontinuous. Many wells in the Environment Canterbury Network (ECAN) investigated here list the aquifer unit name with some offering borehole logs detailing stratigraphy at a site. Wells are screened from several different aquifer formations, including Wainoni, Burwood, Linwood, Riccarton, and Springston Formations, in order of decreasing depth (Figure 5.1b and Table 5.1). However, not all the wells listed in the ECAN database identify which aquifer unit is screened. Because the aquifer-aquitard sequences were deposited with similar source material during regressive-transgressive sea-level change, the composition and sedimentary structures of each unit include many similarities. The depositional environment is primarily glacial outwash river deposits consisting of gravels, sand, and occasional clay or silt lenses [*Brown et al.*, 1988]. Some distinctive features are prevalent yellow clays in the Burwood Formation, occasional peat layers in the Riccarton and Linwood Formations, and that the Springston Formation caps degradational terraces and presently is exposed in several river cuts [*Brown et al.*, 1988]. To the south, Miocene volcanics comprise much of the Banks Peninsula and locally affect the groundwater systems. Banks Peninsula aquifers have isotopically distinctive groundwater within fractures and joints of volcanic rocks and complex flow paths allow mixing with the Canterbury fluvial aquifers [*Brown and Weeber*, 1994].

5.3 Data and Methods

5.3.1 InSAR Surface Deformation

InSAR observations provide high spatial resolution measurements of Canterbury surface deformation caused by earthquake sequences and hydrogeological processes. Wavelet-Based InSAR (WabInSAR) is an advanced multitemporal InSAR approach to analyze numerous sets of SAR images [*Shirzaei*, 2013; *Shirzaei and Bürgmann*, 2013]. The topographic effects and the flat earth are computed and deducted using a reference digital elevation model (DEM) and satellite ephemeris data [*Franchioni and Lanari*, 1999]. Less noisy pixels, referred to as *elite*, are recognized by applying a statistical framework to the estimated noise time series through wavelet analysis of the complex phase observations [*Shirzaei*, 2013]. Wavelet-based filters are also used to correct for topography correlated atmospheric delay and orbital error, while a high-pass filter addresses temporally uncorrelated atmospheric delay [*Shirzaei and Walter*, 2011; *Shirzaei and Bürgmann*, 2012]. The algorithm implements a reweighted least squares approach, thereby inverting the datasets for the line of sight (LOS) displacement time series and achieving sub-millimeter vertical precision.

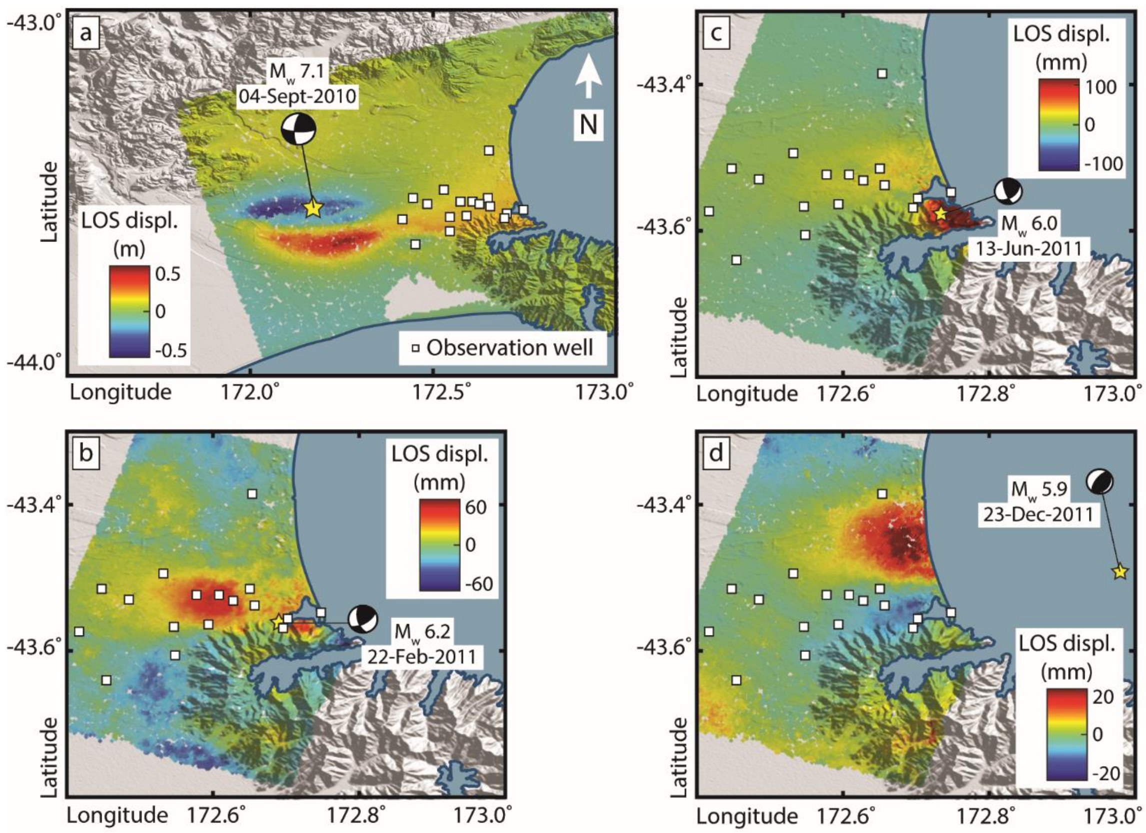

Figure 5.2. Co-seismic Displacement. Time frame for (a) 9-Jul-2010 to 17-Sept-2010, (b) 18-Sept-2010 to 2-Mar-2011, (c) 9-Jun-2011 to 20-Jun-2011 and (d) 2-Dec-2011 to 26-Jan-2012.

From 24-Oct-2003 to 17-Sept-2010, 37 ascending orbit track images from the Envisat satellite capture the pre- and co-seismic deformation of the M_w 7.1 Darfield event (Figure 5.2a). The median repeat interval is 35 days, the mean is 70 days, and the maximum data gap is 664 days. Using this dataset, 165 interferograms are generated with spatial and temporal baselines shorter than 350 meters and 1000 days, respectively. To avoid complications from large temporal gaps, the portion of the time series preceding the maximum gap starting on 28-Sept-2007 is isolated for time series analysis. This selected interval of nearly 4 years preceding the earthquake sequence serves as a baseline for later comparisons.

Next, the 102 descending orbit track images from TerraSAR-X satellite are examined from 7-Sept-2010 to 27-Aug-2015. Using this dataset, ~600 interferograms are generated with horizontal spatial and temporal baselines shorter than 200 meters and 200 days, respectively. The median repeat interval is 11 days, the mean is 18 days, maximum data gap is 165 days, and the complete time series captures the surface deformation associated with the final three of the four shocks (Figure 5.2b-d). To minimize the impact of co-seismic deformation on the estimates of aquifer elastic properties, a subset of the time series is selected that begins shortly after the last event of sequence spanning period 26-Jan-2012 to 27-Aug-2015. Using the viewing geometries of the satellites, the LOS time series is projected, scaled, and the vertical unit vector is isolated (Envisat: incidence = 23º, heading = 349º; and TerraSAR-X: incidence angle = 44.5º, heading angle = 196º).

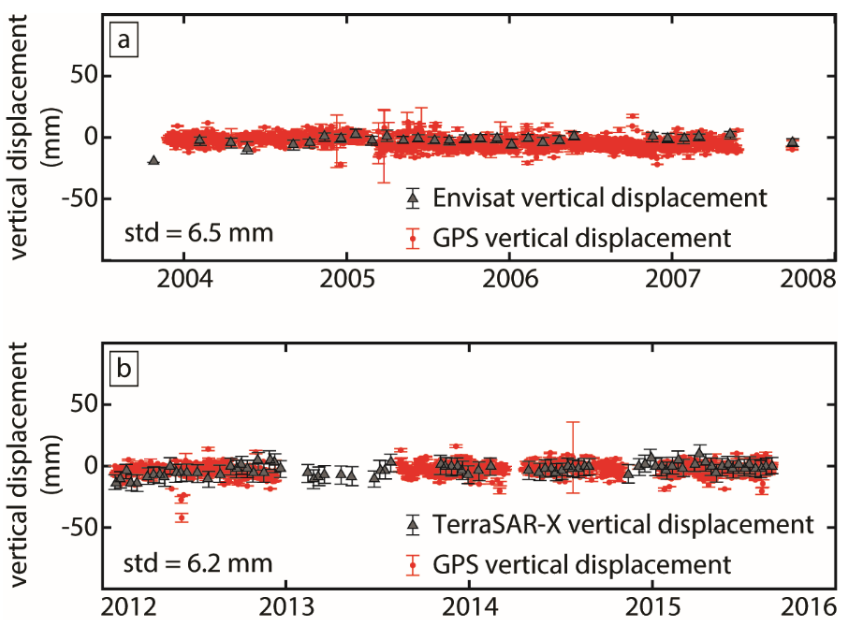

Figure 5.3. The Vertical Component of Daily GPS Time Series Compared to InSAR Vertical Component. (a) Envisat and (b) TerraSAR-X. GPS Station LYTT is referenced to MQZD. InSAR values are the mean of pixels within 250-m of GPS station and are referenced to MQZD.

To validate the InSAR results, the 3D displacement field is compared using two continuous Global Positioning System (GPS) stations LYTT and MQZD which are supplied by GeoNet (http://apps.linz.govt.nz/positionz/). Data measurements for these stations are given in the northern, eastern, and vertical directions and originally referenced to a global reference frame. The daily GPS vertical displacements presented in Figure 5.3 are estimated with respect to the GPS station MQZD, which is used as a local reference for both InSAR and GPS. Comparing the vertical component of InSAR to that of vertical GPS, there is an overall agreement between the two independent time series with an average standard deviation of 6.5 mm for Envisat and 6.2 mm for TerraSAR-X. Inopportunely, the GPS stations are peripherally located on the Banks Peninsula, thus the seasonal behavior exhibited is not coupled with aquifer system processes.

5.3.2 Groundwater Levels

The city of Christchurch and neighboring Canterbury Plains boast a well maintained, dense network of monitoring wells accessible through Environment Canterbury (ECAN). (www.ecan.govt.nz/data/well-search/). Wells with data coincident with InSAR intervals, pre-seismic 24-Oct-

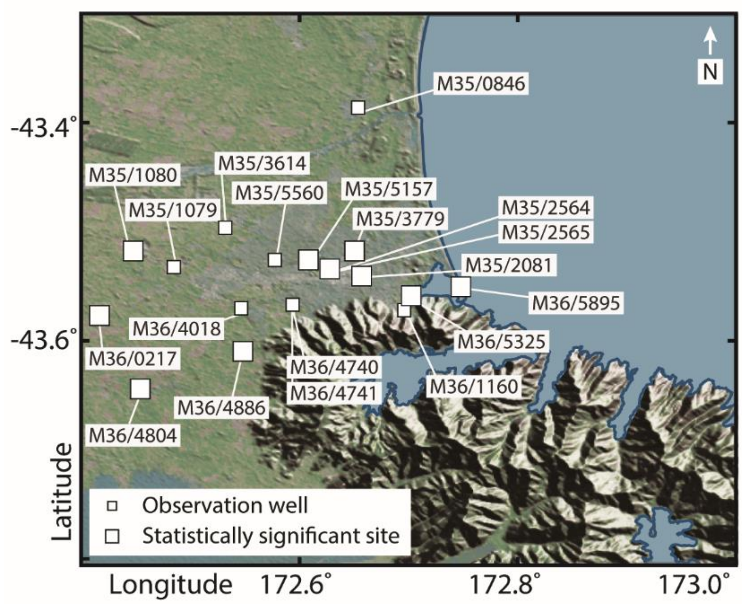

Figure 5.4: Well Names and Locations. Large squares are statistically significant S_{ske}.

2003 to 28-Sept-2007 and post-seismic 26-Jan-2012 to 27-Aug-2015 are selected, excluding those wells with temporal gaps of six months or more. Each wellsite record is examined to assess if the damage sustained in the earthquakes resulted in significant changes in well level readings, i.e. deepening. Nineteen wells meet this criterion and are suitable for analysis (Figure 5.4). The distance of each well to each epicenter (Table 5.1) is shortest for the Feb-22 event with a mean of 11 km and longest the Sept-4 event at 34 km.

5.3.3 Elastic storage coefficient calculation

The elastic skeletal storage coefficient S_{ske} is an important parameter for groundwater flow models and hydrologic theory and it describes the volume of fluid removed or retained as the hydraulic head level fluctuates over an aquifer area [*Riley*, 1969; *Green and Wang*, 1990]. This coefficient represents the elastic behavior of both aquifer and aquitard units in the system [*Hoffmann et al.*, 2001; *Liu and Helm*, 2008]. For the calculation, the seasonal time series of vertical displacement and hydraulic head levels are deconstructed into time-frequency components via continuous wavelet transform following *Miller & Shirzaei* [2015]. Wavelets evaluate signals with nonstationary components and are capable of decomposing a signal into building blocks based on localized frequency properties [*Christopher Torrence*, 1998]. Selected oscillations are identified as occurring within 0.5 to 1.5-year periods, as these wavelengths capture summer highs and winter lows. These seasonal fluctuations elicit an elastic response and exclude shorter-term elastic behavior attributed to tidal effects. The isolated signal components are then reconstructed into seasonal time series for vertical displacement Δb and hydraulic head levels Δh, as inputs to solve: $\Delta b = S_{ske}\Delta h$. Next, a constrained least squares algorithm is applied with an iterative

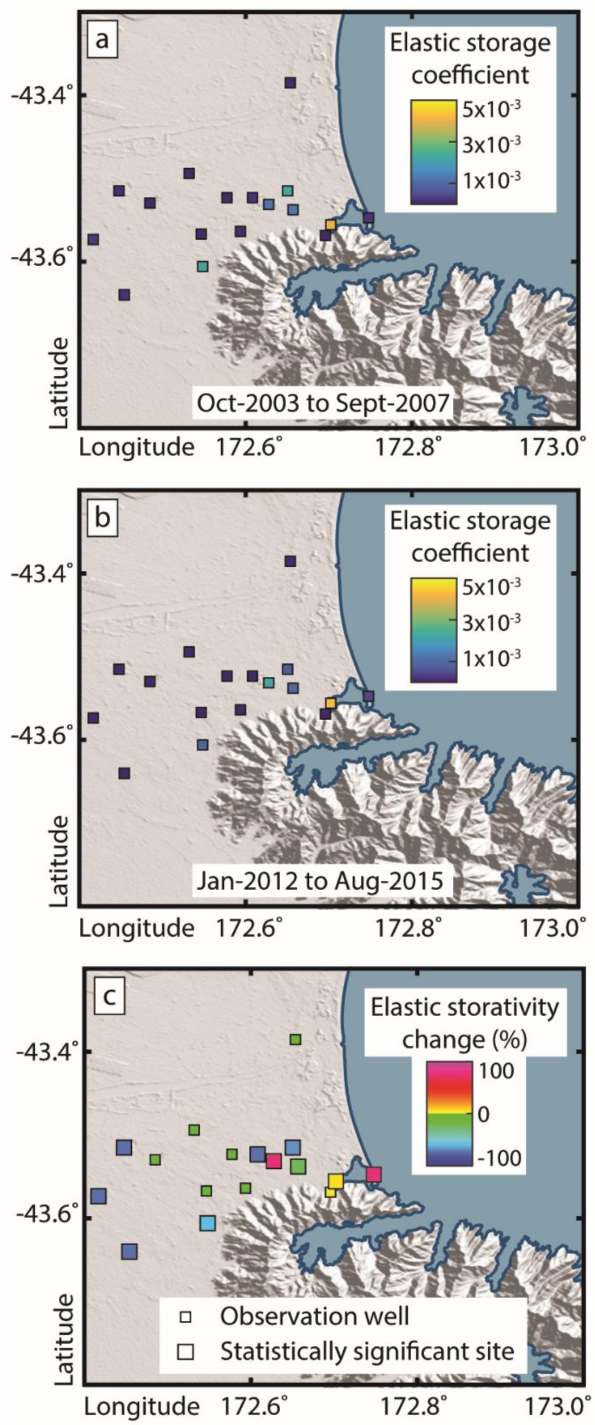

Figure 5.5. Elastic Storage Coefficients calculated at each well for (a) Envisat and (b) TerraSAR-X intervals, and the (c) percentage change difference of mean values between time periods (a & b).

bootstrapping process [*Mikhail et al.*, 1978]. The bootstrapping step repeats the least squares estimation 500 times where each iteration utilizes 80% of time steps that are randomly selected for the calculation. This results in a robust statistical estimation and a probability distribution function for elastic skeletal storage coefficient with uncertainties.

5.4 Results

The skeletal elastic storativity values calculated for the period from 24-Oct-2003 to 28-Sept-2007, i.e. Envisat (Figure 5.5a), range from 1.1×10^{-5} to 4.0×10^{-3}. For the TerraSAR-X period from 26-Jan-2012 to 27-Aug-2015 (Figure 5.5b), the values range from 1.1 $\times 10^{-5}$ to 4.3×10^{-3} (values and uncertainties in Table 5.2). Spatially, the elastic storativity values are lower to the west and north, with higher values found near metropolitan Christchurch and the Banks Peninsula in both

Table 5.2. Elastic Storage Coefficient Values. The unitless value is calculated for each well using well and InSAR time series and head levels (SD = standard deviation).

Well ID	Envisat *24-Oct-2003 to 28-Sept-2007*		TerraSAR-X *26-Jan-2012 to 27-Aug-2015*	
	S_{ske}	SD	S_{ske}	SD
M36/4886	2.22 x10^{3}	2.43 x10^{4}	8.71 x10^{4}	7.86 x10^{5}
M36/4804	1.75 x10^{4}	2.48 x10^{5}	4.47 x10^{5}	4.75 x10^{7}
M36/4741	1.16 x10^{5}	4.36 x10^{6}	1.16 x10^{5}	3.56 x10^{10}
M35/5560	1.12 x10^{5}	3.78 x10^{6}	1.12 x10^{5}	7.36 x10^{10}
M35/3614	1.12 x10^{5}	5.51 x10^{6}	1.11 x10^{5}	5.03 x10^{9}
M36/4740	1.15 x10^{5}	3.88 x10^{6}	1.15 x10^{5}	4.32 x10^{10}
M35/1079	7.10 x10^{5}	2.75 x10^{5}	7.01 x10^{5}	1.96 x10^{7}
M36/4018	1.06 x10^{5}	3.32 x10^{6}	1.06 x10^{5}	1.33 x10^{9}
M35/1080	1.12 x10^{4}	3.12 x10^{5}	2.87 x10^{5}	3.26 x10^{7}
M35/2565	1.22 x10^{3}	5.14 x10^{4}	2.12 x10^{3}	3.27 x10^{6}
M36/1160	1.31 x10^{5}	1.36 x10^{5}	1.31 x10^{5}	2.66 x10^{10}
M36/5325	4.00 x10^{3}	3.72 x10^{4}	4.25 x10^{3}	1.01 x10^{3}
M36/0217	2.82 x10^{4}	6.41 x10^{6}	7.18 x10^{5}	7.23 x10^{7}
M35/2564	8.05 x10^{4}	3.25 x10^{4}	1.41 x10^{3}	2.14 x10^{6}
M35/3779	2.33 x10^{3}	4.62 x10^{4}	7.45 x10^{4}	7.46 x10^{5}
M35/0846	1.19 x10^{5}	1.02 x10^{5}	1.19 x10^{5}	4.00 x10^{10}
M35/5157	2.07 x10^{4}	7.78 x10^{5}	5.27 x10^{5}	6.35 x10^{7}
M35/2081	1.23 x10^{3}	2.71 x10^{4}	9.41 x10^{4}	1.11 x10^{4}
M36/5895	2.34 x10^{4}	8.10 x10^{5}	4.08 x10^{4}	7.48 x10^{7}

calculation intervals. The difference in storativity before and after the earthquake sequence is of interest, therefore it is necessary to determine if the change in elastic storage coefficients is statistically significant. A statistical test is performed on the mean difference at 99% confidence. This test investigates if given the measurement variance estimated through bootstrapping, whether the difference between means is meaningful at the given confidence range [*Meyer*, 1970]. As a result, a subset of 11 wells with significant changes are identified (Figure 5.4).

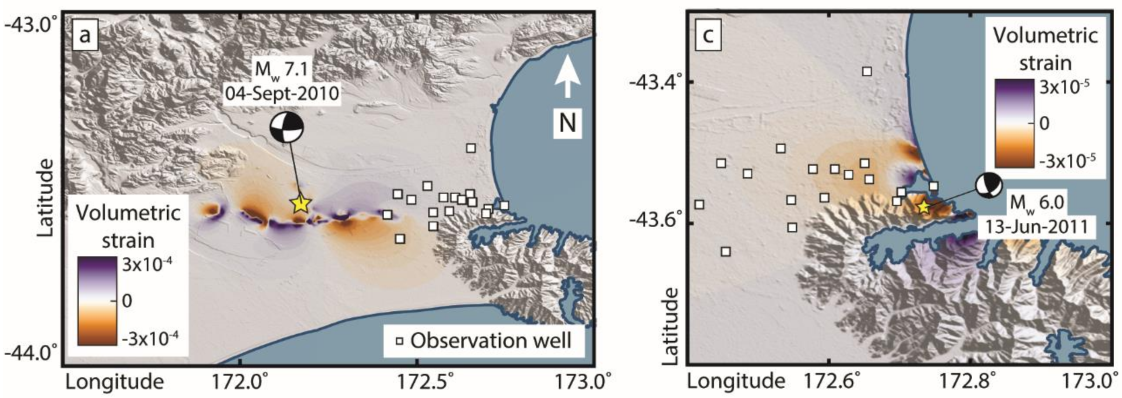

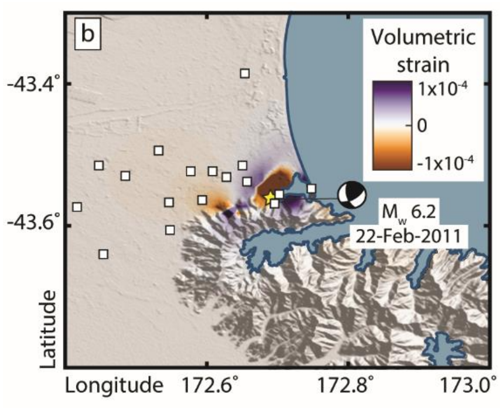

Figure 5.6. Dilatational Strain solutions from *Atzori et al.* [2012]. (a) September 4, 2010 event exhibits sizable strains in the Canterbury Plains with most wells in a compressive regime (excepting M36/0217, M36/4804 & M36/4886), the (b) February 22, 2011 event affects City Centre and the northern Banks Peninsula hills, and the (c) June 13, 2011 event near the coast and Banks Peninsula with most wells in a tensile regime (excepting M35/0846 & M36/5325).

5.5 Discussion

To investigate if the measured changes in storativity are correlated to stress changes imparted by the earthquake sequence, the spatial distribution and sign of significant storativity changes are compared with the estimates of co-seismic volumetric strain change and peak ground velocity. Any meaningful relation between the type of response and distance of sites from epicenter or locations of mapped liquefaction are also explored. To estimate the spatial distribution of co-seismic dilatational strain changes, already published models of co-seismic slip distribution are used. For the first three seismic events, *Atzori et.al,* [2012] model the earthquakes by inverting InSAR displacement maps with constraints based on relocated aftershocks, field data, and Global Positioning System (GPS).

5.5.1 Co-seismic Dilatational Strain Change

The study uses a nonlinear inversion for constraining fault geometry and a linear inversion for slip distribution assuming an elastic half-space on variably sized rectangular patches. Using a forward calculation [*Okada*, 1992], the spatial distribution of dilatational strain for each individual earthquake is obtained and corresponding values at each site are listed in Table 5.3. As one or more events may have an impact on elastic storage properties, the cumulative dilatational strain is explored for three events at each individual site (Figure 5.7). The spatial pattern of the cumulative strain values is complex and areas of compression (positive values) and extension (negative) are often close together near the wells. Net cumulative dilatational strain values range from -2.8 x10^{-4} to 1.33 x10^{-4} with two zones of extreme values: west of the city and north of Banks Peninsula in the south of the city. It is determined if the storage change result is consistent with expectations, i.e., compression reduces storage and extension increases storage. Qualitatively, the net cumulative dilatational strain result agrees with storage increase or decrease. Thirteen of the nineteen wells exhibit changes consistent with the cumulative strain regime, of which eight of eleven have statistically significant changes (Table 5.3). Of the six anomalous wells, three are not showing statistically significant changes (M4740, M35/4741, M36/1160). Well M35/5157, along with the well of statistically insignificant change M36/4740 and M36/4741, is in a cumulative extensive regime, yet initially experienced

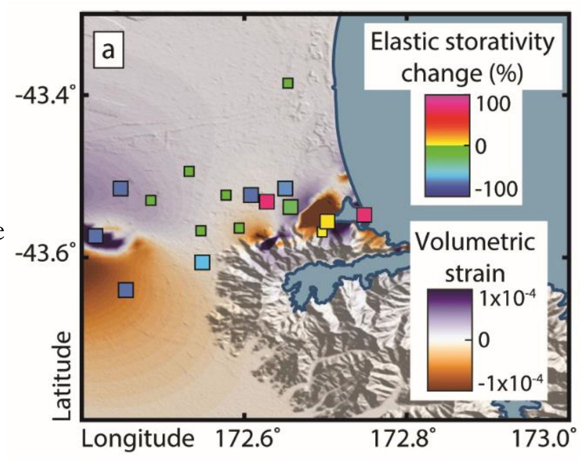

Figure 5.7. Elastic Storativity Change and Cumulative Dilatational Strain Solutions. Strain solutions are combined from *Atzori et al.* [2012] for the three largest earthquakes.

a compressive regime for the Darfield earthquake. A possible explanation for the inconsistent result at these sites is that storage was permanently reduced in the first event, and subsequent extensive strains were unable to dilate the aquifer system.

Table 5.3. Comparing ΔS_{ske} with *Atzori et al.* [2012] dilatational strain solutions. Wells with statistically significant ΔS_{ske} have an x. The *Cumulative* column is strain of *Sept-4 + Feb-22 + Jun-13* earthquakes. Negative strain is extension (orange) and positive strain is contraction (purple). An x in the column $\Delta S_{ske} \sim \sum\sigma$ indicates the *Cumulative* result is consistent with expectations, i.e. compression reduces storage and extension increases storage.

Well	ΔS_{ske}			Strain (+) compression (-) extension			
	$\%\Delta S_{ske}$	Stat Sig	$\Delta S_{ske} \sim \sum\sigma$	*Cumulative*	*Sept-4*	*Feb-22*	*Jun-13*
M36/4886	-60.8	x	-	$-8.7\text{x}10^{-6}$	$-7.1\text{x}10^{-6}$	$-9.8\text{x}10^{-8}$	$-1.5\text{x}10^{-6}$
M36/4804	-74.5	x	-	$-5.7\text{x}10^{-5}$	$-5.7\text{x}10^{-5}$	$-6.7\text{x}10^{-8}$	$-5.1\text{x}10^{-7}$
M36/4741	-0.02	-	-	$-2.2\text{x}10^{-5}$	$6.1\text{x}10^{-6}$	$-2.4\text{x}10^{-5}$	$-4.8\text{x}10^{-6}$
M35/5560	-0.05	-	x	$2.0\text{x}10^{-6}$	$1.4\text{x}10^{-5}$	$-6.7\text{x}10^{-6}$	$-4.9\text{x}10^{-6}$
M35/3614	-0.26	-	x	$1.6\text{x}10^{-5}$	$2.1\text{x}10^{-5}$	$-2.9\text{x}10^{-6}$	$-2.7\text{x}10^{-6}$
M36/4740	-0.02	-	-	$-2.2\text{x}10^{-5}$	$6.1\text{x}10^{-6}$	$-2.4\text{x}10^{-5}$	$-4.8\text{x}10^{-6}$
M35/1079	-1.33	-	x	$3.2\text{x}10^{-5}$	$3.7\text{x}10^{-5}$	$-2.3\text{x}10^{-6}$	$-1.9\text{x}10^{-6}$
M36/4018	-0.07	-	x	$3.3\text{x}10^{-6}$	$1.2\text{x}10^{-5}$	$-5.6\text{x}10^{-6}$	$-2.9\text{x}10^{-6}$
M35/1080	-74.4	x	-	$4.0\text{x}10^{-5}$	$4.3\text{x}10^{-5}$	$-1.5\text{x}10^{-6}$	$-1.4\text{x}10^{-6}$
M35/2565	74.5	x	x	$-1.2\text{x}10^{-6}$	$6.9\text{x}10^{-6}$	$1.4\text{x}10^{-7}$	$-8.2\text{x}10^{-6}$
M36/1160	0.01	-	-	$2.0\text{x}10^{-5}$	$8.7\text{x}10^{-7}$	$2.6\text{x}10^{-5}$	$-7.3\text{x}10^{-6}$
M36/5325	6.24	x	x	$-2.0\text{x}10^{-4}$	$1.5\text{x}10^{-6}$	$-2.0\text{x}10^{-4}$	$-2.2\text{x}10^{-6}$
M36/0217	-74.5	x	x	$1.3\text{x}10^{-4}$	$1.3\text{x}10^{-4}$	$-8.4\text{x}10^{-7}$	$-8.9\text{x}10^{-7}$
M35/2564	74.5	x	x	$-1.2\text{x}10^{-6}$	$6.9\text{x}10^{-6}$	$1.4\text{x}10^{-7}$	$-8.2\text{x}10^{-6}$
M35/3779	-68.0	x	x	$1.3\text{x}10^{-5}$	$6.1\text{x}10^{-6}$	$1.6\text{x}10^{-5}$	$-8.7\text{x}10^{-6}$
M35/0846	-0.02	-	x	$7.6\text{x}10^{-6}$	$6.0\text{x}10^{-6}$	$7.5\text{x}10^{-7}$	$8.9\text{x}10^{-7}$
M35/5157	-74.5	x	-	$-2.8\text{x}10^{-6}$	$9.2\text{x}10^{-6}$	$-5.2\text{x}10^{-6}$	$-6.8\text{x}10^{-6}$
M35/2081	-23.7	x	x	$4.1\text{x}10^{-5}$	$4.2\text{x}10^{-6}$	$4.6\text{x}10^{-5}$	$-9.2\text{x}10^{-6}$
M36/5895	74.5	x	x	$-2.8\text{x}10^{-4}$	$1.1\text{x}10^{-6}$	$-2.6\text{x}10^{-4}$	$-1.9\text{x}10^{-5}$

Table 5.4 displays an estimate of correlation coefficients relating total cumulative dilatational strain to the percentage change in the elastic storage coefficient ΔS_{ske} for A-all wells, SS-wells with statistically significant changes in elastic storativity, further categorized into C-compressive and D-dilatational regimes.

Table 5.4. Correlations Coefficients: all wells (A), sites with statistically significant ΔS_{ske}, (SS), a compressive regime (C), and represents extensive regime (D).

Correlating		(Sites) (Sites/regime)	Correlation coefficients				
			Cumulative	*Sept-4*	*Feb-22*	*Jun-13*	*Dec-23*
Dilatational strain	% ΔS_{ske}	(A)	0.45	0.18	0.41	0.52	--
		(SS)	0.51	0.19	0.47	0.65	--
		(A, C)	0.62	0.47	0.58	--	--
		(SS, C)	0.28	0.47	0.65	--	--
		(A, D)	0.31	--	0.67	0.56	--
		(SS, D)	0.32	--	0.98	0.65	--
Epicenter distance (km)	% ΔS_{ske}	(A)	--	0.54	0.45	0.53	0.57
		(SS)	--	0.65	0.60	0.66	0.64
PGV (cm/s)	% ΔS_{ske}	(A)	--	-0.28	0.48	0.50	0.44
		(SS)	--	-0.39	0.67	0.58	0.57
Liquefaction severity	% ΔS_{ske}	(A)	0.29	-0.06	0.44	--	--
		(SS)	0.42	-0.03	0.66	--	--
Liquefaction severity	Strain	(A, C)	0.40	0.23	0.37	--	--
		(A, E)		--	0.77	--	--

Considering all wells, the correlation coefficient is 0.45. Considering only wells with statistically significant change results in a coefficient of 0.51. Considering the effect of individual events, the highest correlation coefficients are found in relation to the February earthquake, with statistically significant wells in a compressive regime at 0.58 and in a dilatory regime at 0.98.

Oblique-slip earthquakes, even with small components of dip-slip, are known to have diverse, complex hydrologic responses to static strain [*Muir-Wood and King*, 1993]. The Darfield event was dominantly right-lateral strike slip with up to 1.5 m vertical displacement [*Beavan et al.*, 2010; *Quigley et al.*, 2012]. The Canterbury events generated widespread groundwater level changes which varied spatially, with depth, and response type and direction i.e., slope change, spike offset, step change, and or spikes [*Cox et al.*, 2012; *Gulley et al.*, 2013]. Many of these changes are thought to be permanent [*Cox et al.*, 2012; *Rutter et al.*, 2016] and are still discernable through August 2017. Qualitatively, there is evidence supporting static strain as a mechanism for the changes seen in elastic storage at 13 wells, however, quantitatively, the correlation numbers are not conclusive.

5.5.2 Peak Ground Velocity

Peak ground velocity (PGV), also referred to as strong ground motion, measures the rate of shaking using seismic data and provides a measurement of dynamic strain. Using PGV values from USGS ShakeMaps, (www.earthquake.usgs.gov/data/shakemap/), the spatial distribution of shaking due to each individual earthquake is investigated (Figure 5.8)

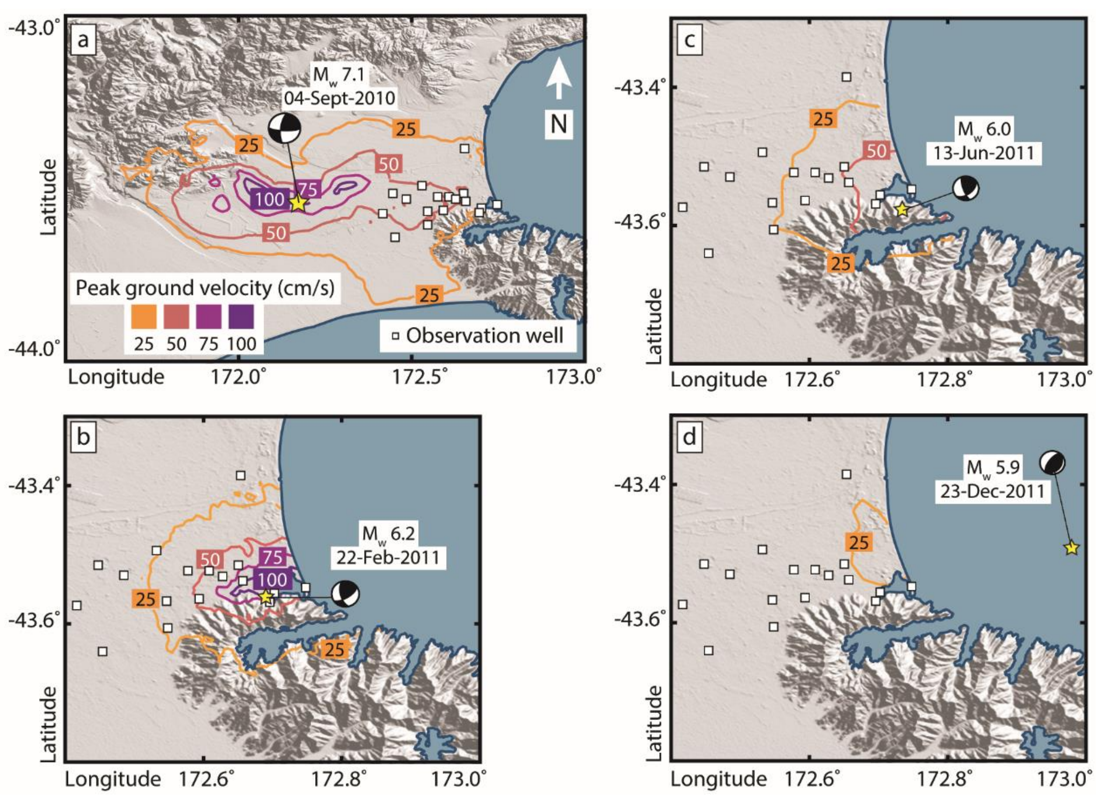

Figure 5.8: Peak Ground Velocity Contours for Each Earthquake.

as well as its amplitude at the location of each site. Each event generates shaking greater than 25 cm/s in or around Christchurch, with velocities over 100 cm/s at several wells during the February earthquake (Table 5.5). To determine if being shaken repeatedly may correlate with observed changes in storativity, the models are combined (Figure 5.9). The solid colormap contours the maximum PGV calculated of all the events, while the green contour lines indicate how many times the area shook greater than 25 m/s. All wells experienced strong ground motion at least once, with most shaking significantly multiple times. As provided in Table 5.4, the observed Darfield earthquake PGV is weakly anticorrelated with elastic storage change for all wells and statistically significantly changed wells. For the subsequent three earthquakes, correlations improve. The response of hydrologic systems to earthquakes is complex, and many studies focus on the evolution of permeability. Linearly dependent on the amplitude of peak ground velocity, analogous to dynamic strain [*Elkhoury et al.*, 2006], sustained permeability increases are observed in California and thought to be related to new fractures or widening fractures [*Rojstaczer et al.*, 1995]. The shaking induced fracturing of aquitards resulting in increased vertical permeability between aquifers is observed in relation to the 1999 Chi-Chi earthquake in Taiwan [*Wang et al.*, 2016].

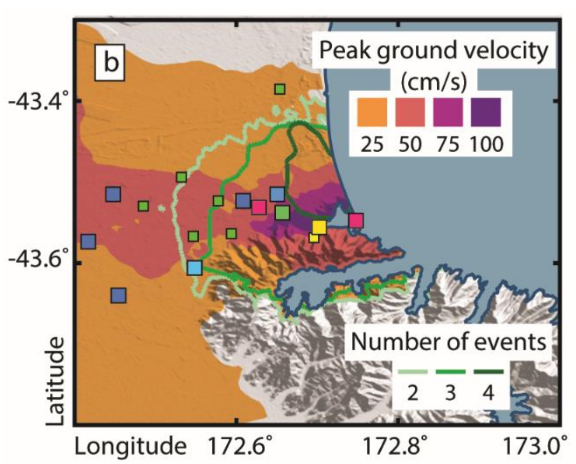

Figure 5.9. Peak Ground Velocity for All Four Events. The solid colormap contours the maximum speed calculated, while the green contour lines indicate how many times the area shook greater than 25 cm/s.

The 2008 Wenchuan earthquake also induced a permeability increase, which then decreased exponentially with time [*Geballe et al.*, 2011]. Permeability decreases are observed in laboratory tests, with or without the addition of silts, when multiple shaking episodes are introduced and permeability decreases with each round as flow paths are blocked [*Liu and Manga*, 2009]. Whether permeability increases or decreases in relation to dynamic strain depends on several mechanisms such as, the number and/or size of fractures, and/or the mobilization of fine-grained sediments which either clears or blocks the flow paths [*Manga et al.*, 2012]. Elastic storage properties are likely to be affected by these same mechanisms.

Table 5.5. Comparing ΔS_{ske} with PGV Solutions and Liquefaction. Wells with statistically significant ΔS_{ske} have an x. Liquefaction codes are (1) minor and (2) moderate/severe.

Well	$\Delta \boldsymbol{S_{ske}}$		Peak ground velocity (cm/s)				Liquefaction	
	% ΔS_{ske}	Stat Sig	*Sept-4*	*Feb-22*	*Jun-13*	*Dec-23*	*Sept-4*	*Feb-22*
M36/4886	-60.8	x	48	27	23	8	-	-
M36/4804	-74.5	x	44	13	10	6	-	-
M36/4741	-0.02	-	49	49	38	11	-	1
M35/5560	-0.05	-	51	39	25	12	-	-
M35/3614	-0.26	-	53	24	17	8	-	-
M36/4740	-0.02	-	49	49	38	11	-	1
M35/1079	-1.33	-	58	17	13	7	-	-
M36/4018	-0.07	-	52	33	22	9	-	-
M35/1080	-74.4	x	56	13	9	6	-	-
M35/2565	74.5	x	52	69	44	19	-	1
M36/1160	0.01	-	26	79	58	17	-	1
M36/5325	6.24	x	30	105	64	21	-	2
M36/0217	-74.5	x	50	11	9	5	-	-
M35/2564	74.5	x	52	69	44	19	-	1
M35/3779	-68.0	x	48	67	48	23	1	1
M35/0846	-0.02	-	34	18	14	12	1	-
M35/5157	-74.5	x	51	54	37	16	1	1
M35/2081	-23.7	x	49	100	48	23	-	1
M36/5895	74.5	x	20	96	66	22	1	2

5.5.3 Liquefaction

Liquefaction is dependent on earthquake magnitude, shaking speed and duration, depth to water table, and the composition and structure of the basin sediments [*Manga and Wang*, 2007]. The liquefaction extent is mapped for the Darfield earthquake and the Feb-22 event [*Townsend et al.*, 2016] (Figure 5.10). These shapefiles are the culmination of interpreting aerial photographs, satellite imagery, and ground-based surveys. Liquefaction is determined based on evidence of predominantly fine sediments and/or water ejected to the surface, and/or the presence of lateral spreading cracks. Similar liquefaction patterns are identified by *Atzori et al.* [2012], who characterized liquefaction using lack of coherence in interferograms.

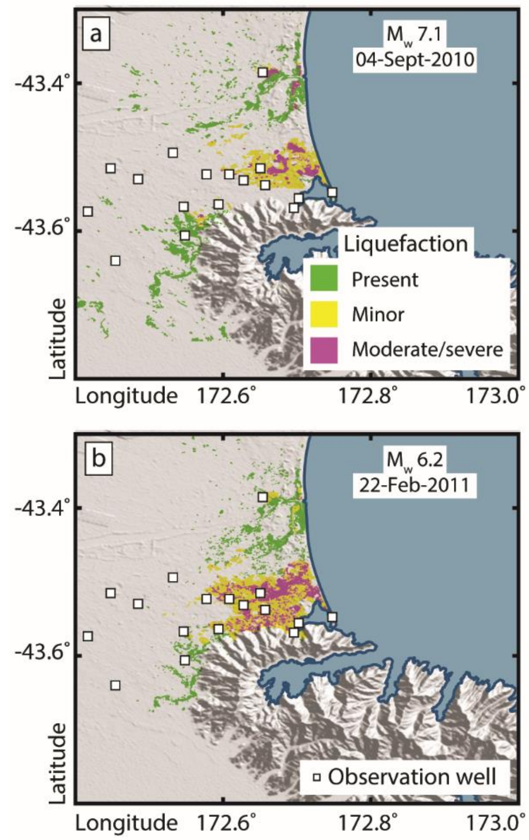

Figure 5.10: Liquefaction Maps [*Townsend et al.*, 2016] adapted by GNS Science for (a) the Darfield earthquake and (b) February event. Liquefaction ranging from present, minor, to moderate/severe.

Qualitatively, 11 out of 19 wells experienced at least one liquefaction event, as did 7 of the 11 statistically significantly changed wells. Figure 5.11 highlights the areas where minor to moderate/severe liquefaction occurs during either earthquake. Numbers represent liquefaction severity in Table 5.5, (1 – minor, 2 – moderate/severe), which are compared to the change in elastic storativity. Correlation is strongest (0.66) in relation to the

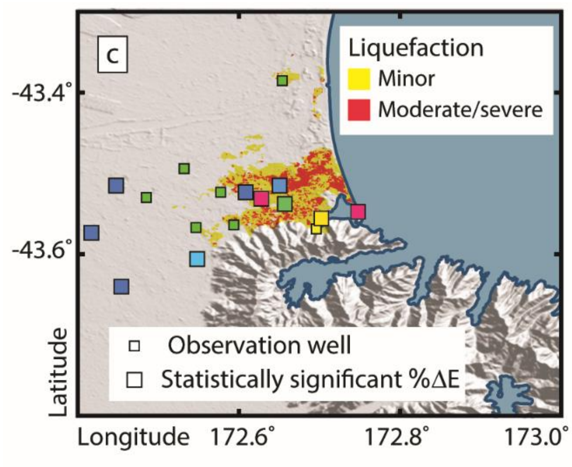

igure 5.11. Combined Liquefaction Occurrence (minor to moderate/severe) Related to Darfield Earthquake and/or the February Event.

February 2011 earthquake, when liquefaction also correlates well with dilatational strain (0.77); correlation coefficients in Table 5.4.

5.5.4 Analysis

A mechanism proposed for the prevalence of liquefaction in Christchurch is the vertical breach of aquitards, releasing artesian fluids upward. *Gulley et al.* [2013], observed several wells with evidence of the vertical movement of fluid coinciding with this study. They identify offsets, which reflect a post-seismic change in aquifer formation in either the positive or negative direction, and spikes, which reflect an immediate, positive transient response of a passing seismic wave. M36/4886, the shallowest well in this study at 9 m, is collocated with a deeper well (M36/4783, 21.5 m) that did not meet the criteria for estimating a change in storage. M36/4886 is a site with a loss of elastic storativity, inconsistent with the extensive dilatational strain regime. However, the hydrographs at this site for the September and February earthquakes, record positive offsets and spikes (Table 5.6), which decay for days. During both earthquakes, the offsets and spikes are higher in the shallower well, but the deeper well remains artesian during the first earthquake while rising to ground level in the second earthquake [*Gulley et al.*, 2013]. This suggests the vertical movement of fluid, and despite the lack of liquefaction mapped at M35/4886, it is possible fine-grained sediments act as plugs in the pore space of the shallower well, reducing storage. M36/4783 has more data than the nearby M36/4804, another well with loss of elastic

Table 5.6. The Behavior of Selected Wells from *Gulley et al., 2013*.

Well	Groundwater response [*Gulley et al.*, 2013]			
	Sep-4		*Feb-22*	
	step	spike	step	spike
M36/4886	0.1	1.8	0.1	1.5
M36/4804	-	-	-	-
M36/4741	-0.1	1.3	-0.0	1.8
M35/5560	0.0	0.3	-	-
M35/3614	-	-	-	-
M36/4740	-0.1	1.2	-0.0	1.6
M35/1079	-	-	-	-
M36/4018	-0.2	1.1	-0.0	0.3
M35/1080	-	-	-	-
M35/2565	-	-	-	-
M36/1160	-	-	-	-
M36/5325	-0.2	0.4	-	-
M36/0217	-	-	-	-
M35/2564	-	-	-	-
M35/3779	-0.4	1.4	-	-
M35/0846	-	-	-	-
M35/5157	-0.0	1.2	-	-
M35/2081	-0.4	2.1	-	-
M36/5895	-	-	-	-

storage in a consistently extensive strain regime, but the same mechanisms may be responsible for the change in properties.

Gulley et al. [2013] posit that negative offsets correlate to deeper wells, which indicates a reduction in storativity. Other wells shared between these two studies are the collocated wells: M36/4740, M36/4741, and M35/5157. Similar patterns exist at these sites, including a compressive regime during the Darfield earthquake, followed by extensive regimes netting in an extensive cumulative strain regime, negative water level offsets and spikes during the earthquakes, and liquefaction mapped. The shallower sites exhibit a slight decrease in storage, that is not statistically significant, but M35/5157 is significantly reduced up to 74.5% at this well. If storativity were reduced in the first earthquake in a compressive regime, subsequent extensive strains greater in absolute values, are likely not enough to re-dilate the system and recuperate what was compacted. Also, the presence of liquefaction at this site suggests movement of fine particles, likely due to transient dynamic strain.

5.6 Concluding Remarks

High-quality water depth data with relatively dense spacing makes Christchurch a natural laboratory for studying the effects of earthquakes on aquifer systems. Many areas in tectonically active zones are reliant on groundwater supplies, which are vulnerable to seismic events. The San Joaquin Valley, California is an agricultural hub near the San Andreas system with the added complications of land subsidence from overexploitation of groundwater and periodic drought. A reduction in storage capacity due to a large magnitude earthquake can threaten the availability of freshwater. Co-seismic changes in water level are observed near Parkfield, California, but any hydraulic conductivity changes during the study duration were within the bound constraints [*Roeloffs*, 1998]. Permeability increased in relation to the Loma Prieto, California earthquake in 1989, and the groundwater water table level declines as discharge increases and the water system is drained [*Rojstaczer and Wolf*, 1992]. Pumping tests of an aquifer system thought to be in a compressional regime during the Chi-Chi 1999 earthquake show a decrease in storativity attributed to consolidated soil particles [*Jang et al.*, 2008]. With the rise of induced seismicity from fluid injection related to fracking activities [*Chang and Segall*, 2016; *Shirzaei et al.*, 2016], there is also concern that a sufficiently large magnitude event can affect groundwater or alter the properties of freshwater aquifers nearby [*Wang et al.*, 2017]. Additional work is needed studying changes in elastic storativity due to earthquakes.

This chapter is adapted from a journal article in preparation for submission.

CHAPTER 6: IMPACT OF LOCAL SUBSIDENCE AND GLOBAL CLIMATE CHANGE ON FLOODING SEVERITY FROM HURRICANE HARVEY

Abstract: Hurricane Harvey caused unprecedented flooding and socioeconomic devastation in Eastern Texas with high winds, elevated storm tide, and record rainfall. Inland flooding is mapped with satellite radar imagery and vast areas outside of hazard zones are overwhelmed. We explore subsidence using measurements with synthetic aperture radar interferometry and find that prior to the cyclone 89% of the flooded area subsided 3 mm/yr or more. The robust correlation demonstrates subsidence intensifies flood severity by modifying base flood elevations and topographic gradients. Given projections of sea level rise and ongoing subsidence through 2100, we determine that 247-294 km^2 of land is at risk of inundation during a future cyclone, compared to 100-158 km^2 considering sea level rise alone. This study highlights the importance of incorporating local land subsidence in flood resilience strategies.

6.1 Background

Climate change amplifies flooding in coastal cities around the world and such flooding is further exacerbated by a combination of anthropogenic and natural changes to the land surface [*Hanson et al.*, 2011]. Sustained climate warming trends result in global Sea Level Rise (SLR), increasing both the occurrence and extent of flooding [*Hirabayashi et al.*, 2013; *Aerts et al.*, 2014]. Concurrent ocean temperature rise increases the frequency and intensity of tropical cyclones [*Knutson et al.*, 2010; *Mousavi et al.*, 2011; *Woodruff et al.*, 2013] and storm surge magnitudes [*Lin et al.*, 2012]. In addition to global climate change phenomena, localized anthropogenic changes to land usage and cover also worsens flooding by wetland depredation [*Day et al.*, 2007], conversion to less permeable ground cover [*Liscum*, 2001], and land subsidence. The vertical motion of land surface primarily stems from groundwater and hydrocarbon extraction and can lower flood control structures [*Dixon et al.*, 2006], change floodplain boundaries and base flood drainage [*Wang et al.*, 2012], and submerge wetlands [*Galloway et al.*, 2003; *Morton et al.*, 2006]. Already, the combined effects of land subsidence and SLR prompted construction of expensive flood defense infrastructure in Tokyo, Bangkok, and Shanghai [*Nicholls and Cazenave*, 2003], elevated housing in the Philippines [*Jamero et al.*, 2017], and abandoned communities in the greater Houston area [*Ingebritsen and Galloway*, 2014]. Storm surge flooding is particularly sensitive to SLR in Galveston Bay [*Warner and Tissot*, 2012] and furthermore, the land subsides due to both aquifer [*Coplin, L.S., Galloway*, 1999] and hydrocarbon reservoir depletion [*Holzer and Bluntzer*, 1984]. The Houston-Galveston region acts as a natural laboratory to study the flooding patterns during cyclones and the convergence of disastrous, anthropogenic complications.

Following rapid intensification Hurricane Harvey made landfall on August 25th, 2018, then stalled over Texas for three days causing a rare 9000-year extreme precipitation event as a tropical storm [*van Oldenborgh et al.*, 2017]. The cyclone spawned during a natural warm swing of temperature variances in the North Atlantic Ocean [*Rosen*, 2017], however, modeling indicates global warming increased the intensity of rainfall increased by 15% and the probability of this much rain or more by a factor of three [*van Oldenborgh et al.*, 2017]. The category-4 storm claimed 80 lives, displaced multitudes, damaged more than 80,000 houses lacking flood insurance [*Shultz et al.*, 2017], of which most are outside of the Federal Emergency Management Agency (FEMA) designated 500-year flood zone [*Blessing et al.*, 2017]. These severe socioeconomic consequences illustrate the importance of disseminating the concerted impacts of global climate change and localized land subsidence to anomalous flooding.

In this chapter, the spatial extent of flooding is observed through analysis of backscatter properties of synthetic aperture radar (SAR) data sets. Second, the extent of storm surge flooding is determined by modeling inundation during the storm tide on a high-resolution DEM created with Light Detection and Ranging (LIDAR) data. Third, land subsidence in the region is detected for the years preceding the cyclone using InSAR and a chi-squares goodness of fit test to determine the significance of the correlation between flooded and subsiding areas. Finally, focus is directed to future coastal flood patterns by 2100 considering projections of sea level rise, continued subsidence, and storms.

6.2 Estimating the Extent of the Harvey Flooding

Change detection to determine the near real-time flood extent using multi-temporal satellite SAR data sets offers the benefit of broad spatial cover and cloud penetration [*Long et al.*, 2014; *Clement et al.*, 2017]. A snapshot of the extent of the flooded zone due to Hurricane Harvey is mapped using synthetic aperture radar (SAR) images acquired by Sentinal-1A/B satellites. Following the approach of *Clement et al.* [2017], a flood-free reference amplitude image is generated using 44 SAR images acquired prior to the hurricane. The amplitude values of each pixel in the reference image are the median of the amplitude time series, minimizing the effects of seasonal surface changes and enhancing the signal to noise ratio. The difference of amplitudes is calculated between the reference image and an image acquired after the storm on August 30th, reflecting the change in radar backscattering

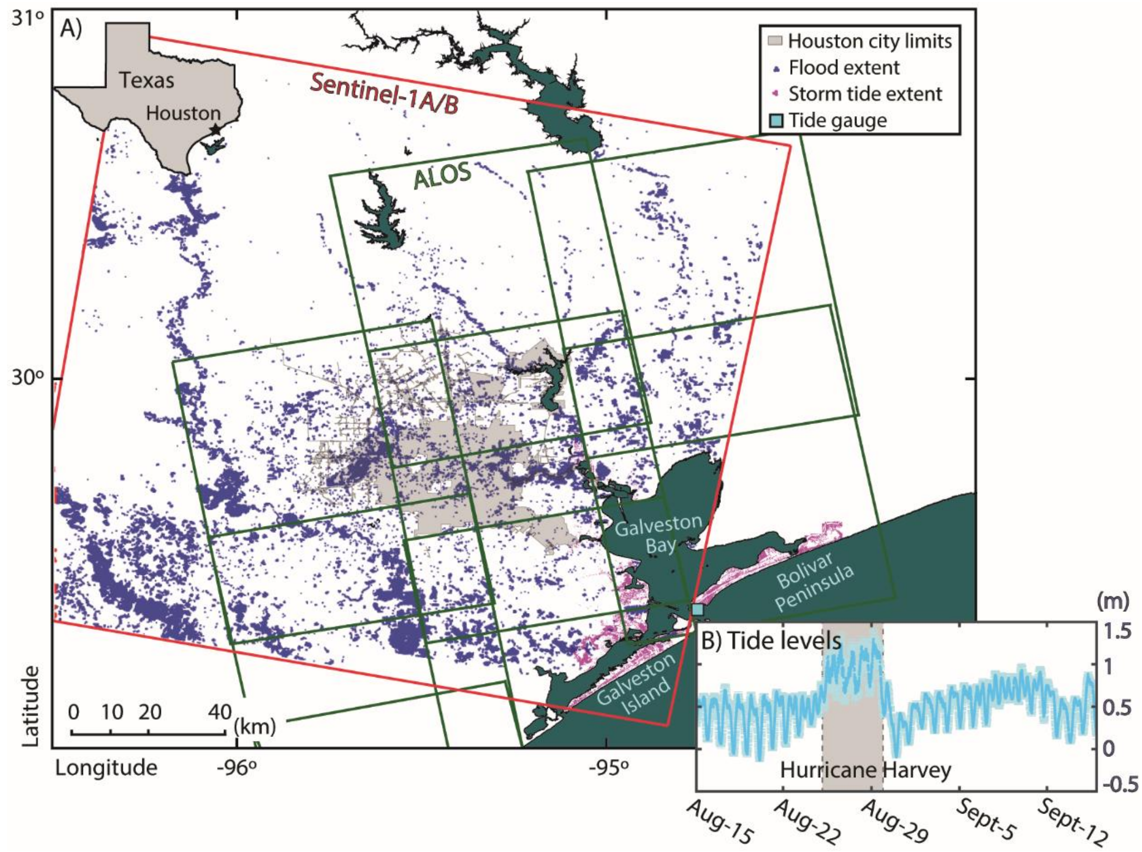

Figure 6.1. Study Overview (a) SAR satellite footprints for ALOS-PALSAR (green) and Sentinel-1A/B SAR (red). Inland flooded pixels from runoff and precipitation are detected using Sentinel SAR. Area inundated due to a 1.3-meter storm tide identified with magenta markers. Location marked by cyan box is location of (B) tide gauge time series from NOAA station located at Galveston Bay entrance, North Jetty (Station ID: 8771341).

primarily due to flooding. The speckle noise is removed from both the pre-cyclonic reference image and the flood image with a median filter of 5×5 pixels. This minimally impacts the reference image and improves the signal to noise ratio for flood image. Clement et al. [2017] further filter the difference images using a reference DEM to remove the zones that are unlikely to flood. However, in this case this step is avoided because the DEM is possibly modified by local land subsidence. The criteria for identifying flooded pixels is given by;

$$P(x, y) < \mu - f_c\,\sigma \tag{6.1}$$

where μ and σ are the mean and standard deviation of difference image and f_c is a coefficient. If the pixel located at azimuth and range location of (x, y) passes this test, it is flooded. The coefficient f_c is site dependent and *Clement et al.,* [2017] following *Long et al.* [2014] consider it to be 1.5. However, visual inspections indicate that f_c equal to 1.25 yields a more accurate estimate of flood extent for this area (Figure 6.1). The satellite frame encompasses the Houston metropolitan area and inland suburbs. Extensive flooding is detected west and southwest of the Houston metropolitan area, with a total submerged area of 782 km^2 (Figure 6.1a). Although many concentrations follow river channels, there is also extensive flooding beyond the designated 500-year flood zone. A National Oceanic and Atmospheric Administration (NOAA) tide gauge in Galveston records a high storm tide of 1.3 m above mean sea level (Figure 6.1b).

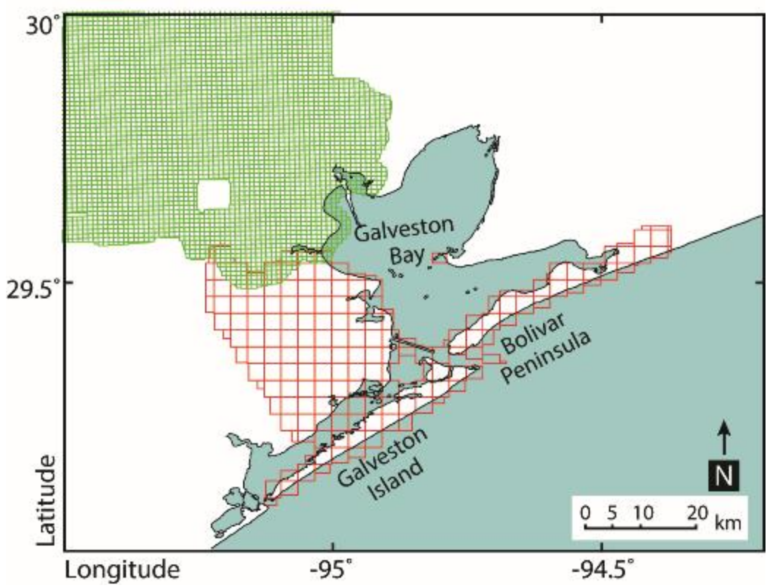

Figure 6.2. LiDAR Footprints. Harris County (green) acquired in 2001 and Galveston County (red) acquired in 2005.

Focusing on the coastal region, the flood extent due to storm tide is modeled for Harris and Galveston counties on 1m x 1m horizontal resolution LIDAR DEMs (Figure 6.2), which are reviewed by NOAA. Harris County data (data.noaa.gov/dataset/2001-hcfcd-lidar-harris-county-tx) was collected in 2001 and Galveston County in 2005 (coast.noaa.gov/htdata/lidar1_z/geoid12a/data/89/). Heights are given in the North

American Vertical Datum of 1988 (NAVD 88) reference frame and the vertical error associated with LiDAR DEM is ~10 cm. In modeling the high storm tide of 1.3 m on the LIDAR DEMs, floods overwhelm 71 km^2, including much of the northern coastlines of Galveston Island and Bolivar Peninsula (Figure 6.1a), as well as low-lying shores of the Houston Ship Channel and several natural and man-made islands. However, the storm tide does not extend far inland. The total flooded area for both the inland and coastal regions is 853 km^2.

6.3. Flooding Compared to Hazard Zones

National Flood Hazard Layer (NFHL) incorporates all flood insurance rate map databases published by FEMA. The primary risk classifications in the study area are a 0.2% annual chance flood risk (500-year flood) and a minimal risk (Figure 6.3a). Areas flooded by Hurricane Harvey, as detected from Sentinel-1A/B are compared with the NFHL risk designation (Figure 6.3b). Assuming a pixel size of 50m x 50m, the total area flooded in a 500-year flood zone is 27 km^2 and that in a minimal risk classification is 115 km^2. In the following, land subsidence is investigated as a possible driver for flood waters to accumulate in minimal risk areas.

Figure 6.3 next page) Flood Hazard Areas and Classification (a) FEMA NFHL 500-yr flood areas (red) and areas of minimal hazard (yellow) mapped as of 2015 (b) NFHL Classification of flooded pixels detected with SAR.

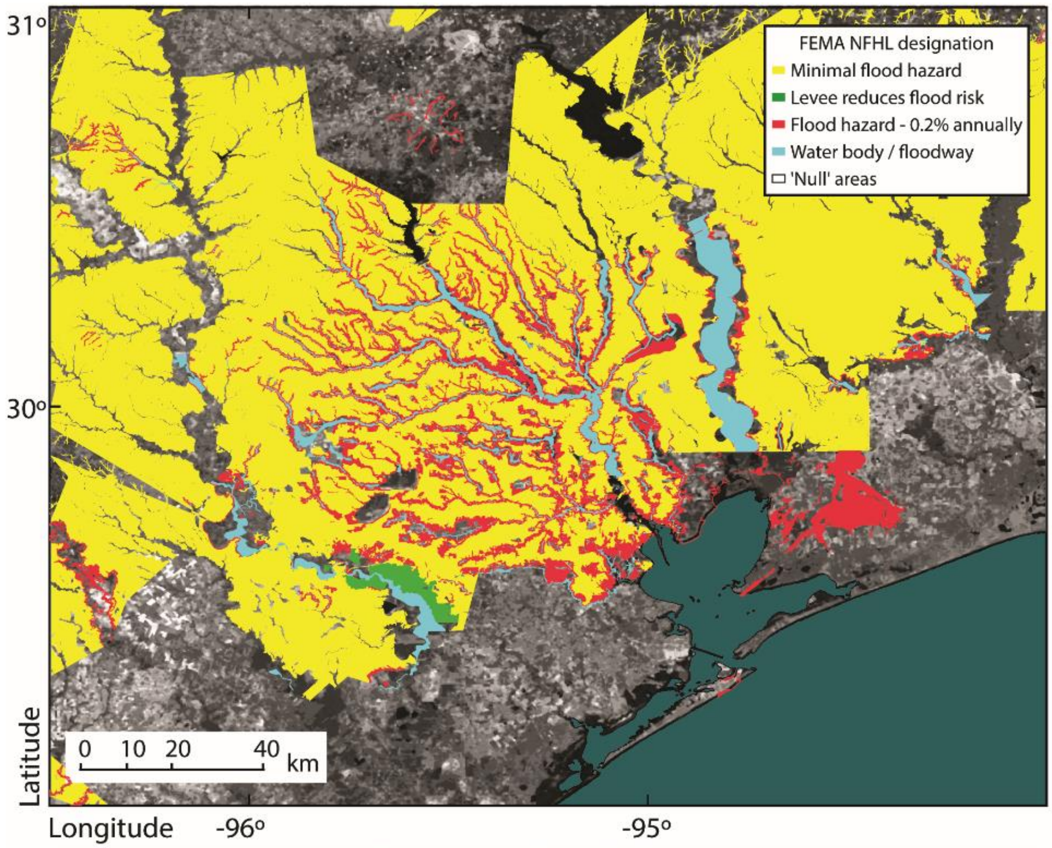
FEMA NFHL designation
Minimal flood hazard
Levee reduces flood risk
Flood hazard - 0.2% annually
Water body / floodway
'Null' areas
31°
30°
0 10 20 40 km
Latitude
Longitude
-96°
-95°

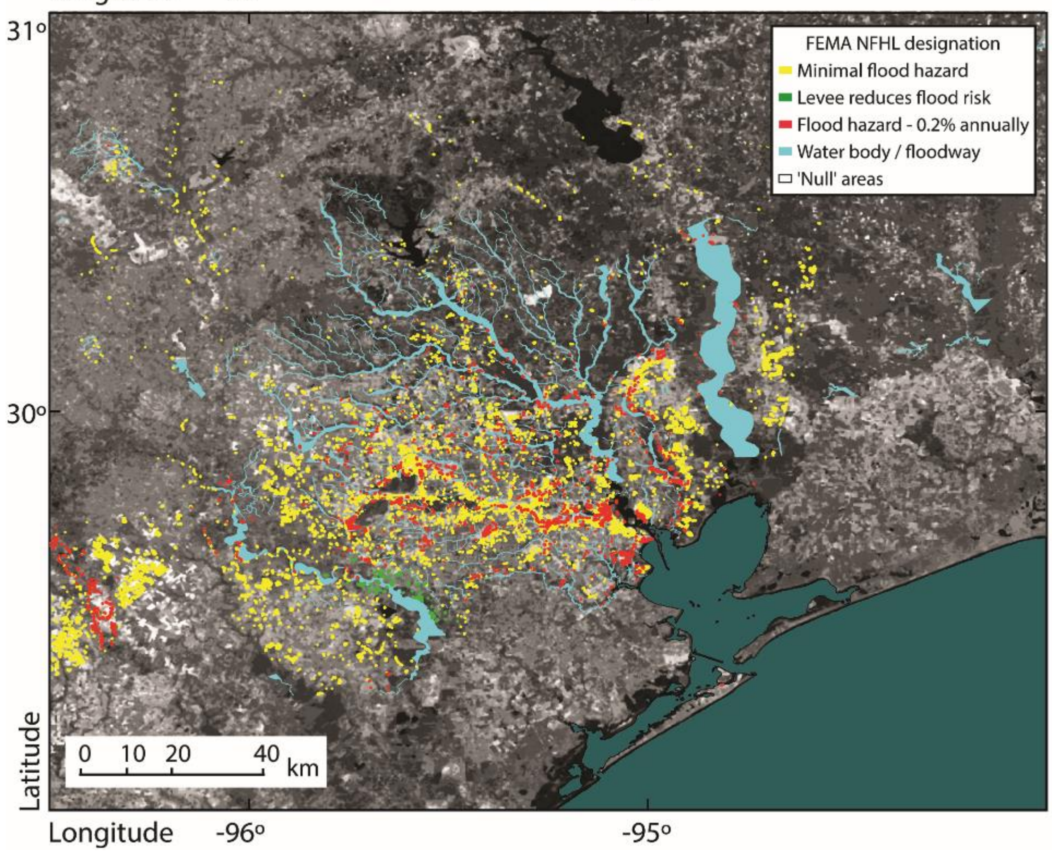
FEMA NFHL designation
Minimal flood hazard
Levee reduces flood risk
Flood hazard - 0.2% annually
Water body / floodway
'Null' areas
31°
30°
0 10 20 40 km
Latitude
Longitude
-96°
-95°

6.4 Subsidence and Flooding

Historically the study area subsided due to oil and gas production [*Holzer and Bluntzer*, 1984] and groundwater exploitation [*Kearns et al.*, 2015]. Rapid groundwater extraction occurred prior to 1980 in the Houston Galveston area; since 2005, hydraulic head levels are relatively stable with annual change of less than 1 m (Figure 6.4), yet prior pumping may still have an effect [*Poland and Davis*, 1969].

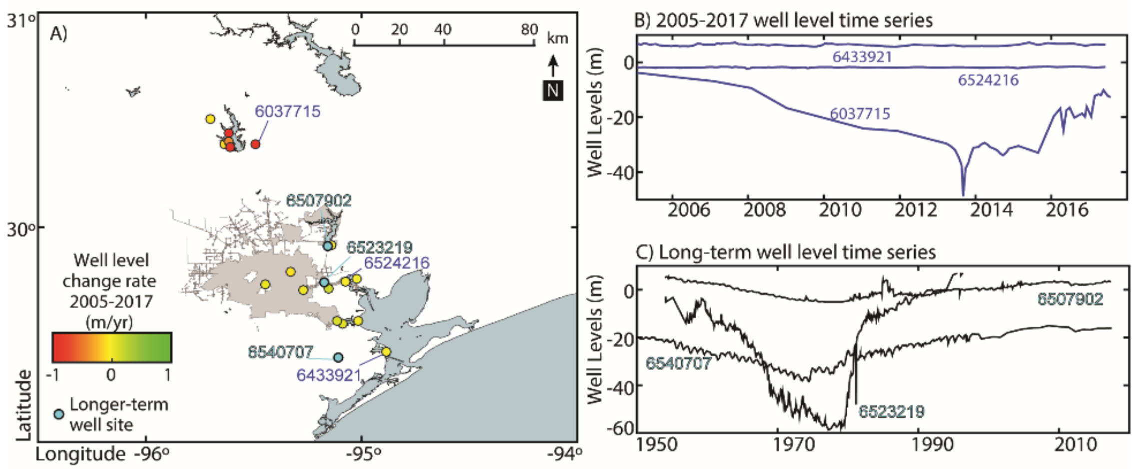

Figure 6.4) Water Level History (a) Colored circles show well level change per year (2005-17). Wells north of the city decline at this time, yet the Houston and coastal wells remain comparatively stable. (b) Time series of selected wells. (c) Extended time series displaying period of significant drawdown, which begins to reverse in the 1970-80's. www.waterdata.usgs.gov.

6.5 InSAR and GNSS Data

InSAR and GNSS are widely used to monitor land subsidence due to natural and anthropogenic processes [*Galloway and Burbey*, 2011; *Miller and Shirzaei*, 2015]. To characterize the rate of vertical land motion prior to the cyclone, a multitemporal InSAR approach is applied to large data sets from ALOS and Sentinel 1A/B satellites in combination with horizontal velocities of continuous GNSS stations [*Shirzaei et al.*, 2013b, 2017]. To transfer the vertical deformation estimates into a continental framework, NA12, a 1-D conformal transformation is applied to the rates of vertical motion at continuous GNSS stations. Wavelet-Based InSAR (WabInSAR) algorithm is implemented, which is a multitemporal SAR interferometric approach, [*Shirzaei*, 2013; *Shirzaei and Bürgmann*, 2013; *Shirzaei et al.*, 2017].

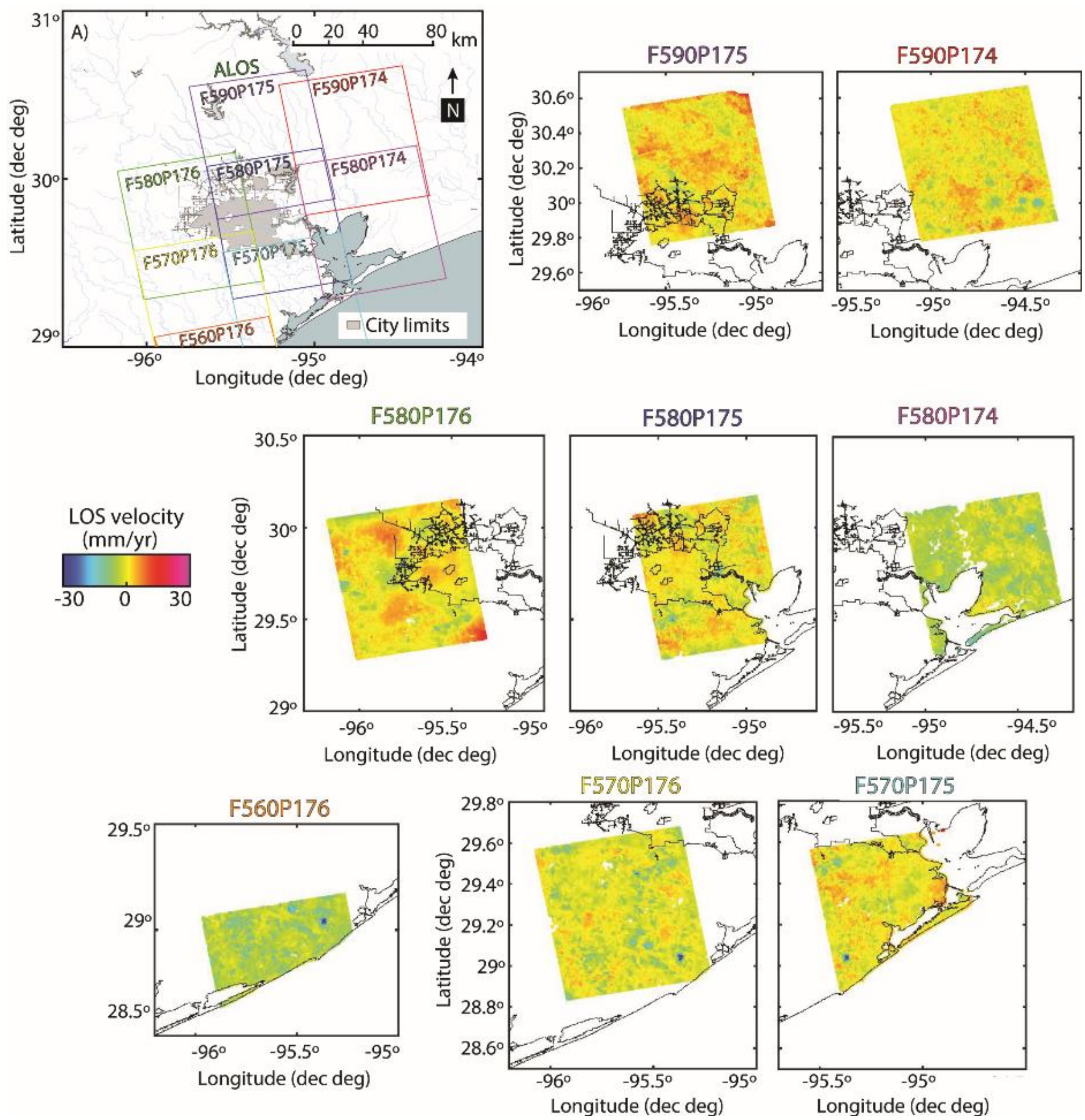

Figure 6.5) Overview of ALOS Frames and LOS Velocity Maps (identified by outline color). The colormap is uniform for all maps where cool colors are moving away from the satellite. Average heading and incidence angles are 345º and 38.5º.

Starting with a large set of SAR images acquired from similar radar viewing geometry, they are precisely co-registered to the same master image. The flat earth effect and topography are removed using a reference 30 m Shuttle Radar Topography Mission DEM [*Farr et al.*, 2007] and satellite ephemeris data [*Franchioni and Lanari*, 1999]. The algorithm applies a statistical framework to identify *elite* pixels based on the complex phase noise estimated with wavelet analysis. WabInSAR implements a variety of wavelet-based filters to correct the effects of topography correlated atmospheric delay [*Shirzaei and Bürgmann*, 2012]. Lastly, through a reweighted least square approach, WabInSAR inverts the interferometric phase and generates a seamless time series of the line-of-sight (LOS) surface deformation.

Overlapping frames of ALOS in ascending orbit include 101 L-Band SAR images acquired in 8 partially overlapping tracks and spanning the period 2007-2011 (Appendix A.1). The average heading and incidence angles are 345 and 38.5 degrees, respectively. These datasets generate 496 high-quality interferograms (Appendix A.2). The LOS displacement rates are shown in Figure 6.5, which include more than 20,000,000 pixels at ~50 m resolution.

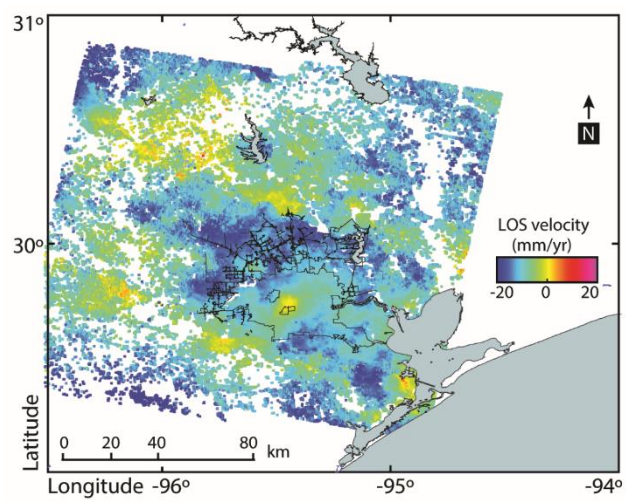

Figure 6.6) LOS Velocity via Sentinel-1-A/B. Cool colors are moving away from the satellite. Average heading and incidence angles are 192° and 23°.

This method I also applied to a data set of 44 C-band images acquired in descending orbit of Sentinel-1A/B satellites spanning the period 2015/12/21 and 2017/08/24 (Appendix A.2). 195 interferograms are generated with spatial and temporal baselines less than 45 m and 120 days, respectively. The pixel size is ~50m x 50m. The specifics of this SAR processing are detailed in *Shirzaei et al.,* [2017]. LOS displacement rates are shown in Figure 6.6.

To correct LOS measurements for horizontal motions due to tectonic processes, the approach of *Burgmann et al.* [2006] is implemented and the horizontal velocities of permanent global navigation satellite system (GNSS) stations, both E-W, and N-S components [*Bürgmann et al.*, 2006]. The measurements of more than 500 permanent GNSS stations of the PBO network across southern Texas are provided by University of Nevada geodetic laboratory [*Blewitt et al.*, 2013]. A subset of these stations with measurements spanning the duration of SAR acquisitions is used to calculate and remove the effect of horizontal displacement rates. The remaining signal considered to be solely due to vertical land motion and is projected on the vertical direction using satellite unit vectors.

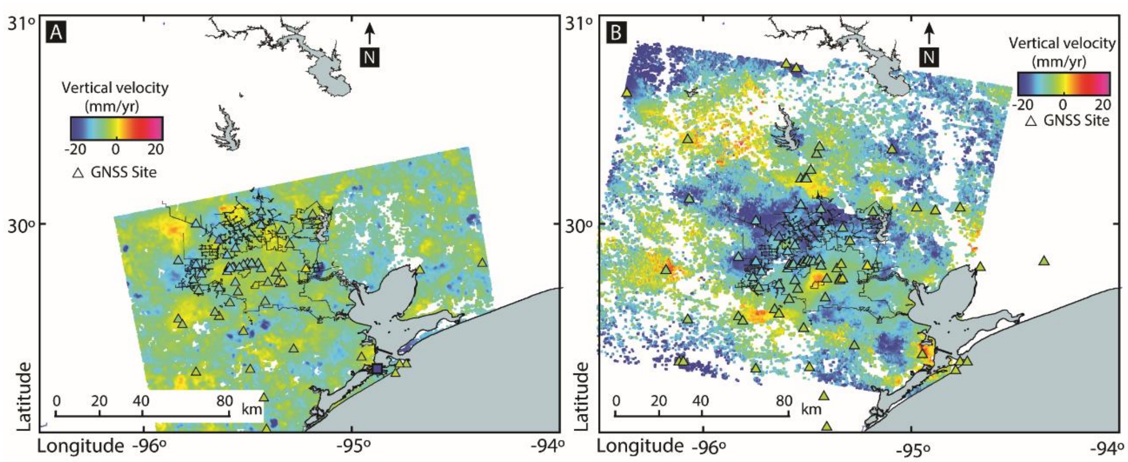

Figure 6.7. Vertical Velocity Maps, The colormap represents subsidence rates calculated from multitemporal SAR interferometric analysis of (a) ALOS and (b) Sentinel-1A/B to generate vertical velocity map.

InSAR derived subsidence velocities show a rate up to 49 mm/yr during the ALOS acquisition period (Jul-07 – Jan-11, Figure 6.7a) and 34 mm/yr during Sentinel (Dec-15 to

Aug-17, Figure 6.7b). Both data sets are also characterized by several localized zones of uplift, potentially related to salt diapirs [*Huffman et al.*, 2004], tectonic processes, and/or faulting [*Qu et al.*, 2015]. The standard deviation between ALOS and GNSS is 2.34 mm/yr, Sentinel 1-A/B, and GNSS is 6.1 mm/yr, and ALOS and Sentinel1-A/B is 5.0 mm/yr, which constitutes good agreement. Considering 3 mm/yr. as the threshold for subsidence to be significant, 89% of the inland flooded areas are also characterized by significant subsidence prior to the storm (Figure 6.8a&b).

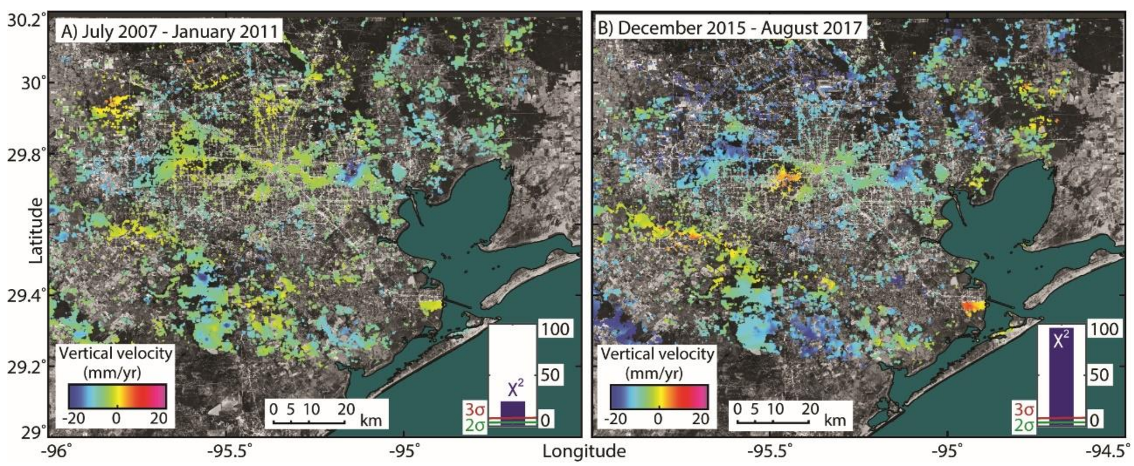

Figure 6.8) Subsidence of Flooded Areas. Areas flooded by Hurricane Harvey and detected following investigating Sentinel-1A/B SAR backscattering intensity. The colormap represents subsidence rates calculated from multitemporal SAR interferometric analysis of (a) ALOS and (b) Sentinel-1A/B to generate vertical velocity map.

A Chi-square test is performed to investigate the statistical significance of the correlation between observed subsidence and mapped flood extent, The Chi-square statistic tests the similarity between frequency distributions, where out of a total of potential outcomes, the observed frequency is compared to expected frequency for a particular outcome [*Meyer*, 1970]. To define these outcomes, the subsidence map derived from ALOS and flood map derived from Sentinel-1A/B are interpolated onto a reference grid. At each collocated area, it is determined if subsidence greater than 3 mm/yr occurs or not s, and if flooding f is detected or not. Four potential outcomes are identified as: 1) flooded, subsiding 2) flooded, not subsiding 3) not flooded, subsiding 4) not flooded, not subsiding. The expected frequency is calculated separately for each outcome, $E_i = (n_s * n_f)/n$, where n is the number of total observations. The chi-squares statistic, $\chi^2 = \sum_{i=1}^{4} \frac{(O-E)^2}{E}$, is then compared to the inverse of a chi-square cumulative distribution function with probability significance level (99%) and one degree of freedom. If the chi-squares statistic is larger, the null hypothesis is rejected and the populations are not independent.

If flooded areas and subsidence zones are correlated, the flooded area should be proportional to the subsided area. Thus, the Chi-square statistic is used to test the null hypothesis that flooded areas are randomly distributed with respect to subsided zones. Figures 6.8 a&b insets show the results of the Chi-squares test at 99% confidence level. Both ALOS and Sentinel data sets have levels of correlation exceeding the 99% significance level and thus the null hypothesis is rejected. Since flooded areas and subsided zones are correlated, special attention to subsidence patterns is needed to identify where floodwaters can collect without proper draining. Other anthropogenic factors likely intensified damage from precipitation and runoff, as Houston has experienced a 114% increase in asphalt and concrete land cover since 1984 [*Khan*, 2005].

6.6 Inundation Extent Forecasting

Exploring the contribution of land subsidence to coastal inundation considering SLR projections, LIDAR data is combined with InSAR derived subsidence maps projected forward 100 years. Next, the SLR forecast based on Representative Concentration Pathway

(RCP) 8.5 is applied [*IPCC Working Group 1*, 2014]. The forecast range by 2100 (67% probability) is from 0.78 to 1.50 meters [*DeCaonto and Pollard*, 2016]. The RCP 8.5 is a scenario in which no significant effort to mitigate or remove emissions is taken.

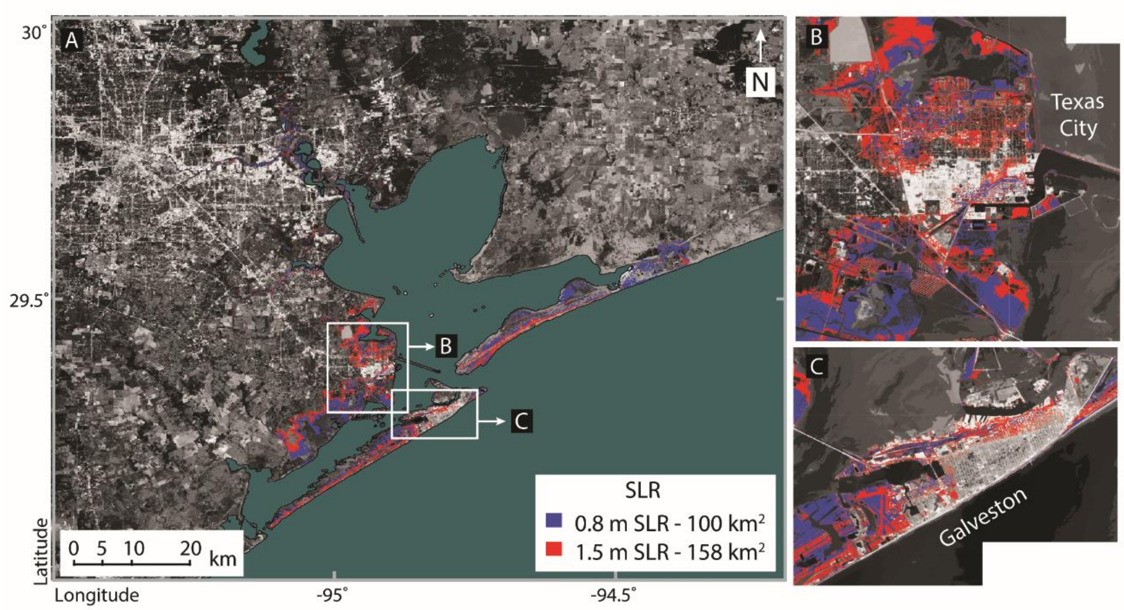

Figure 6.9) Inundation Scenarios (a – i) (a) Areas of inundation by 2100 using SLR forecast range of 0.8 to 1.5 meters following RCP 8.5 and modeled using a LiDAR DEM at 2m x 2m resolution to simulate surface topography. (b) Zoom on Texas City and (c) Galveston.

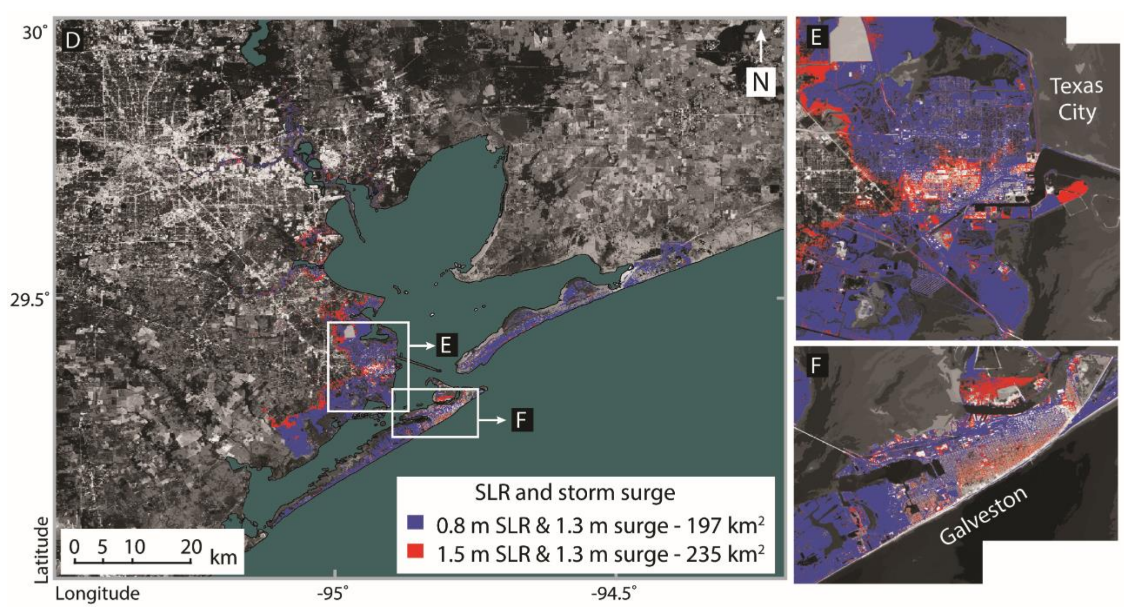

(d) Areas of inundation by 2100 using SLR forecast and a Hurricane Harvey equivalent storm tide. (e) Zoom on Texas City and (f) Galveston.

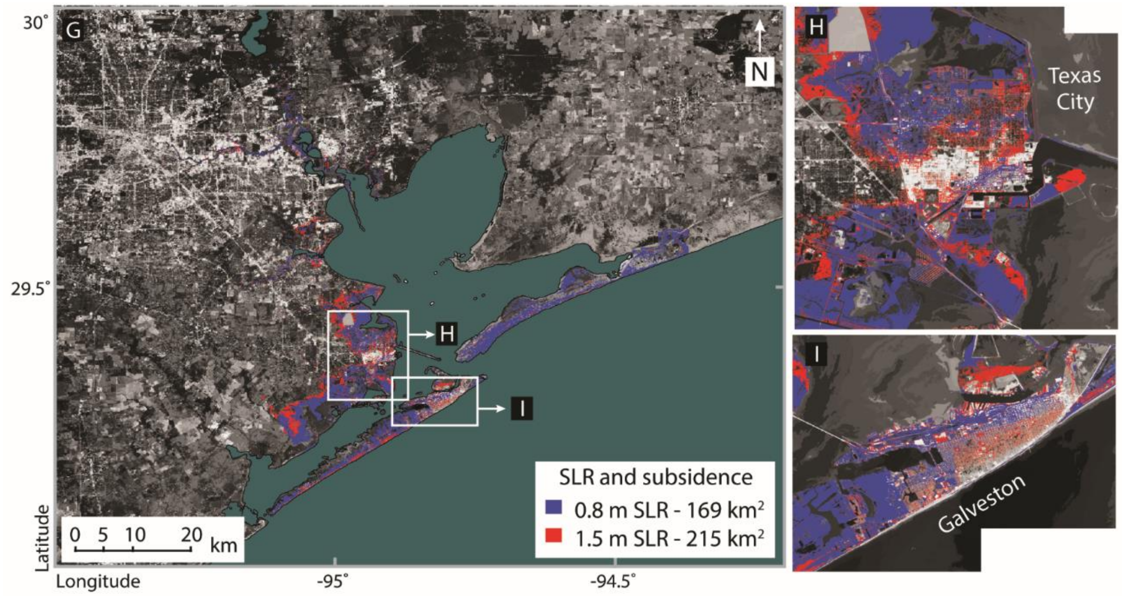

(g) Areas of inundation by 2100 using SLR forecast and static subsidence following RCP 8.5. (h) Zoom on Texas City and (i) Galveston.

Using the lower and upper RCP projection as bounds, modeling shows that SLR alone will submerge an area from 100 to158 km^2 by 2100 (Figure 6.9a-c). Sea level rise accompanied by a storm tide equivalent to that of Hurricane Harvey, the area engulfed is 197 to 235 km^2 (Figure 6.9d-f). Next, projections of steady subsidence rates are considered in addition to SLR and it is determined that the total flooded area to be 169 km^2 to 215 km^2 (Figure 6.9g-i). Finally, a composite scenario including SLR, a storm tide of 1.30 m, and unabated subsidence are projected (Figure 6.10), in which the area vulnerable to flooding is 247 or 294 km^2. Much of Galveston Island, the Bolivar Peninsula, Texas City and La Marque are affected in these models. Although this scenario is extreme, the exercise allows for exploring a *worst-case* scenario and gives perspective on potential flooding patterns.

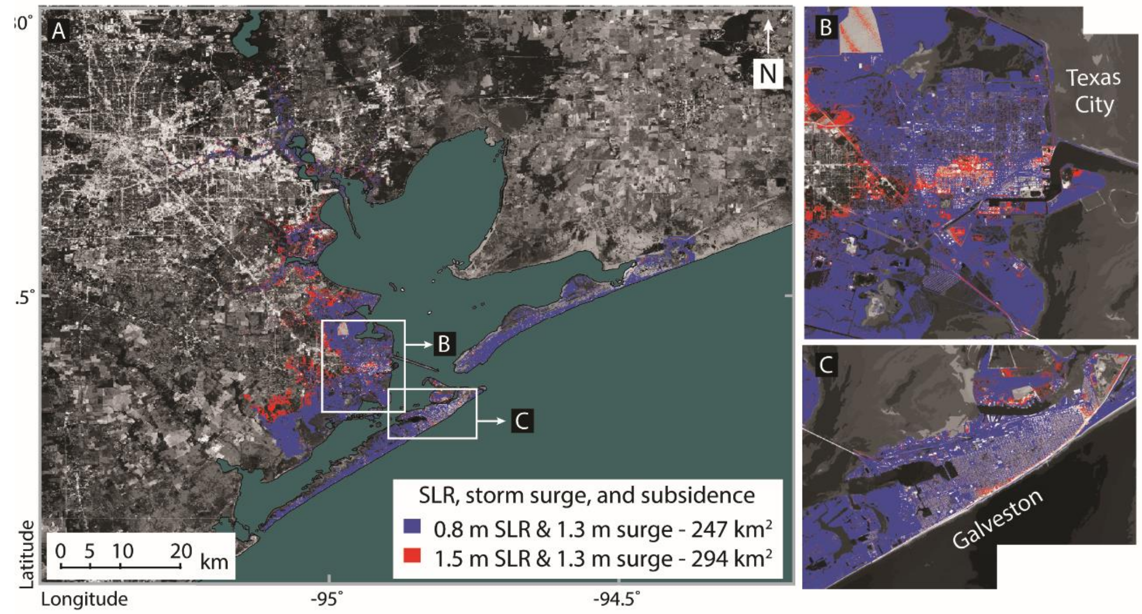

Figure 6.10. Modeling Extreme Coastal Flooding (a) Areas of inundation by 2100 using SLR forecast following RCP 8.5, static subsidence, and a Hurricane Harvey equivalent storm tide of 1.3 meters above MSL. (b) Texas City and (c) Galveston exhibit extensive flooding whether SLR is at the lower bound or upper bound of the RCP range.

6.7 Discussion

The unprecedented flooding during Hurricane Harvey results primarily from heavy rainfall, yet its correlation to localized land subsidence is robust. Land subsidence is likely to continue throughout the 21st century and has the potential to accelerate if substantial groundwater overdraft resumes. Moreover, accelerated land subsidence is possible with rising oil prices, because oil production rates are price-dependent [*Rehrl and Friedrich*, 2006].

Houston is a natural laboratory for studying the combined effects of global climate change on coastal city flooding, including long-term SLR and intensified hurricanes. The probability of Harvey-like rainfall, estimated to be ~1% during the period 1981-2000 under RCP 8.5 scenario, but it rises to 18% for the period 2081-2100 [*Emanuel*, 2017]. Here, the contributions of local land subsidence to flood severity are confirmed. Improved inundation scenarios are developed, integrating high-resolution digital topography, detailed and accurate estimates of coastal LLS, probabilistic projections of SLR and a Harvey-like storm tide.

These techniques do have limitations. SAR imaging used for flood mapping and interferometry for deformation time series relies on the availability of satellite scenes, which are as frequent as every 6 days with Sentinel. However, the availability of an image at peak flood is unlikely. In this case, floodwater recession may have occurred prior to the acquisition, making this estimate a lower bound on the extent of flooding. Near real-time flood mapping would require the use of airborne radar, like the Uninhabited Aerial Vehicle Synthetic Aperture Radar (UAVSAR).

As of 2005, more than 40 million people worldwide lived in areas prone to coastal flooding, and over $3,000 Billion USD is at risk [*Hanson et al.*, 2011]. Coastal populations will grow more than 300% by 2070 and the properties affected by flash flooding will value to ~9% of the projected global GDP [*Aerts et al.*, 2014]. The countries of USA, Japan, and the Netherlands include the most areas with significant flood exposure, but major flood disasters can affect regional to continental scales making flood hazard interdependencies an additional concern [*Jongman et al.*, 2014]. Combining remote sensing techniques such as InSAR and GNSS will provide a broad perspective of vertical land motion. A more accurate hydrologic model including subsidence and sea level rise can help coastal cities to remap flood risk zones and improve their flood resilience. The techniques implemented in this study can be used to evaluate other cities, inform policy decisions, improve hazard risk assessments and flood resilience strategies.

This chapter is adapted from a manuscript in preparation for submission

CHAPTER 7: CONCLUSION

Monitoring and managing groundwater is crucial for ensuring freshwater availability. Geodesy and remote sensing techniques, including InSAR, GPS, and LIDAR capture the surface manifestation of aquifer deformation at depth. In turn, time series and inversion analysis reveals insight about underground reservoir characteristics, water in storage, and forecast areas where deformation is likely to form hazardous earth fissures and flood prone zones. Case studies featured in this work lead to several conclusions:

1) In the Phoenix AMA, three subsidence zones with unique deformation patterns and characteristics are detected, as well as a broad uplift zone coinciding with recharge well locations. Subsidence continues in locations where well levels have significantly recovered. Aquifer properties are estimated, including elastic storativity, inelastic storativity, and the compaction time constant. Distinctive horizontal deformation patterns indicate there are heterogeneities in either the aquifer system material or the basement.

2) For the Phoenix AMA, time series of displacement are used to constrain an inversion for volumetric strain. Volumetric strain at depth is used to solve for the stress tensor near the surface. By examining the ratio of minimum principal stress and the tensile strength of the aquifer material, areas prone to earth fissures are identified.

3) Investigating a long-time series of deformation and well levels in Tucson, the volume of storage previously permanently lost to compaction is calculated. Decelerated compaction is observed with the implementation of artificial recharge effort, likely reducing hazards associated with earth fissuring and infrastructure damage. Calculation of aquifer properties suggests that vertical hydraulic conductivity is comparatively high in this area.

4) Elastic storage values calculated before and after the 2010-2011 Canterbury earthquake sequence are statistically different. A pattern is sought by comparing the patterns of elastic storativity change to static strain of dilatation, dynamic strain of peak ground velocity, maps of liquefaction. Results are inconclusive, likely due to the complex nature of the earthquake sequence, layered aquifer system, and data availability.

5) Hurricane Harvey devastated Houston and Galveston, Texas in August 2017. The spatial extent of flooding observed with SAR backscatter analysis is compared to subsidence maps derived from InSAR. Of the flooded area, 89% subsided at least 3 mm/yr in the years leading up to the cyclone. Scenarios of future coastal flood patterns by 2100 are explored using LIDAR data and projections of sea level rise, continued subsidence, and intense storms. Much of the coast of Houston-Galveston is subject to inundation in these scenarios.

These case studies highlight that each aquifer system has unique properties and behavior. For example, in Phoenix artificial recharge is tied to a broad uplift zone, while in Tucson, artificial recharge diffuses quickly and uplift is not detected. Also, Phoenix experiences residual compaction where wells have recovered, whereas subsidence in Tucson has stalled. This work also emphasizes the versatility of the methods used. For example, identifying and analyzing subtle seasonal variations for calculation of elastic storativity is applicable in a variety of environments. Techniques used in the deserts of Arizona are also applied to temperate, seismically active areas like Christchurch.

Assessing aquifer responses and understanding subterranean poroelastic processes and mechanisms are vital for sustainability of freshwater supplies. The increasing availability of high spatiotemporal resolution SAR data and refinement of inversion techniques will continue to improve our understanding.

REFERENCES

ADWR (1999), *Third management Plan for the Phoenix Active Management Area. 2000-2010.*, Phoenix, AZ.

Aerts, J. C. J. H., W. J. W. Botzen, K. Emanuel, N. Lin, H. De Moel, and E. O. Michel-Kerjan (2014), Climate adaptation: Evaluating flood resilience strategies for coastal megacities, *Science (80-.).*, *344*(6183), 473–475, doi:10.1126/science.1248222.

Aeschbach-Hertig, W., and T. Gleeson (2012), Regional strategies for the accelerating global problem of groundwater depletion, *Nat. Geosci.*, *5*(12), 853–861, doi:10.1038/ngeo1617.

Amelung, F., D. L. Galloway, J. W. Bell, H. A. Zebker, and R. J. Laczniak (1999), Sensing the ups and downs of Las Vegas: InSAR reveals structural control of land subsidence and aquifer-system deformation, *Geology*, *27*(6), 483–486, doi:10.1130/0091-7613(1999)027<0483:STUADO>2.3.CO;2.

Anderson, S. R., H. H. Schumann, and B. L. Wallace (1982), *Progress report on measurement of aquifer compaction in the Tucson basin, Annual static water level basic data report, Tucson basin and Avra Valley, Pima County, Arizona*, City of Tucson.

Anderson, S. R. R. (1988), Potential for aquifer compaction, land subsidence, and earth fissures in the Tucson basin, Pima County, Arizona, *U.S. Geol. Surv. Hydrol. Atlas 713*, (USGS Numbered Series).

Anderson, T. W. (1995), Summary of the southwest alluvial basins, regional aquifer-system analysis, south-central Arizona and parts of adjacent states, *USGS Prof. Pap. 1406-A*, (USGS Numbered Series), A1–A33.

Argus, D. F. (2012), Uncertainty in the velocity between the mass center and surface of Earth, *J. Geophys. Res. B Solid Earth*, *117*(10), doi:10.1029/2012JB009196.

Argus, D. F., Y. Fu, and F. W. Landerer (2014), Seasonal variation in total water storage in California inferred from GPS observations of vertical land motion, *Geophys. Res. Lett.*, *41*(6), 1971–1980, doi:10.1002/2014GL059570.

Arizona Geological Survey (2015), *Locations of Mapped Earth Fissure Traces in Arizona, Arizona Geological Survey, v 05.11.2015*, Arizona Geological Survey, Phoenix, AZ.

Arizona Geological Survey (2017), *Locations of Mapped Earth Fissure Traces in Arizona, Arizona Geological Survey, v 11.06.2017*, Arizona Geological Survey, Phoenix, AZ.

Atzori, S., C. Tolomei, A. Antonioli, J. P. Merryman Boncori, S. Bannister, E. Trasatti, P. Pasquali, and S. Salvi (2012), The 2010-2011 Canterbury, New Zealand, seismic sequence: Multiple source analysis from InSAR data and modeling, *J. Geophys. Res. Solid Earth*, *117*(8), doi:10.1029/2012JB009178.

Bannister, S., and K. Gledhill (2012), Evolution of the 2010-2012 Canterbury earthquake sequence, *New Zeal. J. Geol. Geophys.*, *55*(3), 295–304, doi:10.1080/00288306.2012.680475.

Beavan, J., S. Samsonov, M. Motagh, L. Wallace, S. Ellis, and N. Palmer (2010), The darfield (canterbury) earthquake: Geodetic observations and preliminary source model, *Bull. New Zeal. Soc. Earthq. Eng.*, *43*(4), 228–235.

Beavan, J., M. Motagh, E. J. Fielding, N. Donnelly, and D. Collett (2012), Fault slip models of the 2010-2011 Canterbury, New Zealand, earthquakes from geodetic data and observations of postseismic ground deformation, *New Zeal. J. Geol. Geophys.*, *55*(3), 207–221, doi:10.1080/00288306.2012.697472.

Bell, J. W., F. Amelung, A. Ferretti, M. Bianchi, and F. Novali (2008), Monitoring aquifer-system response to groundwater pumping and artificial recharge, *First Break*, *26*(8), 85–91, doi:10.1029/2007WR006152.

Biot, M. A. (1941), General theory of three-dimensional consolidation, *J. Appl. Phys.*, *12*(2), 155–164, doi:10.1063/1.1712886.

Blessing, R., A. Sebastian, and S. D. Brody (2017), Flood Risk Delineation in the U.S.: How much loss are we capturing?, *Nat. Hazards Rev.*, *18*(3), 1–10, doi:10.1061/(ASCE)NH.1527-6996.0000242.

Blewitt, G., C. Kreemer, W. C. Hammond, and J. M. Goldfarb (2013), Terrestrial reference frame NA12 for crustal deformation studies in North America, *J. Geodyn.*, *72*, 11–24, doi:10.1016/j.jog.2013.08.004.

Brown, L. J., and J. H. Weeber (1994), Hydrogeological implications of geology at the boundary of banks peninsula volcanic rock aquifers and canterbury plains fluvial gravel aquifers, *New Zeal. J. Geol. Geophys.*, *37*(2), 181–193, doi:10.1080/00288306.1994.9514613.

Brown, L. J., D. D. Wilson, N. T. Moar, and D. C. Mildenhall (1988), Stratigraphy of the late quaternary deposits of the northern Canterbury Plains, New Zealand, *New Zeal. J. Geol. Geophys.*, *31*(3), 305–335, doi:10.1080/00288306.1988.10417779.

Budhu, M. (2008), Mechanics of Earth Fissures Using the Mohr-Coulomb Failure Criterion, *Environ. Eng. Geosci.*, *14*(4), 281–295, doi:10.2113/gseegeosci.14.4.281.

Budhu, M., and I. Adiyaman (2013), The Influence of Clay Zones on Land Subsidence from Groundwater Pumping, , *51*(1), 51–57, doi:10.1111/j.1745-6584.2012.00943.x.

Buisman, C. (1936), Verslag Van De Onderzoekingen Over De Iepenziekte, Verricht In Het Phytopathologisch Laboratorium Willie Commelin Scholten Te Baarn Gedurende 1935, *Tijdschr. Over Plantenziekten*, *42*(10), 21–44, doi:10.1007/BF02810267.

Burbey, T. (2001a), Storage Coefficient Revisited: Is Purely Vertical Strain a Good Assumption?, *Ground Water*, *39*(3), 458–464, doi:10.1111/j.1745-6584.2001.tb02330.x.

Burbey, T. J. (2001b), Stress-Strain Analyses for Aquifer-System Characterization, *Ground Water*, *39*(1), 128–136, doi:10.1111/j.1745-6584.2001.tb00358.x.

Bürgmann, R., P. A. Rosen, and E. J. Fielding (2000), Synthetic Aperture Radar Interferometry to Measure Earth's Surface Topography and Its Deformation, *Annu. Rev. Earth Planet. Sci.*, *28*(1), 169–209, doi:10.1146/annurev.earth.28.1.169.

Bürgmann, R., G. Hilley, A. Ferretti, and F. Novali (2006), Resolving vertical tectonics in the San Francisco Bay Area from permanent scatterer InSAR and GPS analysis, *Geology*, *34*(3), 221–224.

Cabral-Cano, E., T. H. Dixon, F. Miralles-Wilhelm, O. Díaz-Molina, O. Sánchez-Zamora, and R. E. Carande (2008), Space geodetic imaging of rapid ground subsidence in Mexico City, *Bull. Geol. Soc. Am.*, *120*(11–12), 1556–1566, doi:10.1130/B26001.1.

Carpenter, M. C. (1987), *Water-level declines, land subsidence, and specific compaction near Apache Junction, south-central Arizona*, USGS Numbered Series: Water-Resources Investigations Report 86-4071, Tuscon, AZ.

Carruth, B. R. L., D. R. Pool, and C. E. Anderson (2005), Land Subsidence and Aquifer Compaction in the Tucson Active Management Area , South-Central Arizona — 1987 – 2005, *Water*, 1987–1990.

Castle, S. L., B. F. Thomas, J. T. Reager, M. Rodell, S. C. Swenson, and J. S. Famiglietti (2014), Groundwater depletion during drought threatens future water security of the Colorado River Basin, *Geophys. Res. Lett.*, *41*(16), 5904–5911, doi:10.1002/2014GL061055.

Casu, F., S. M. Buckley, M. Manzo, A. Pepe, and R. Lanari (2005), Large scale InSAR deformation time series: Phoenix and houston case studies, in *International Geoscience and Remote Sensing Symposium (IGARSS)*, vol. 7, pp. 5240–5243, IEEE.

Chang, K. W., and P. Segall (2016), Seismicity on Basement Faults Induced by Simultaneous Fluid Injection–Extraction, *Pure Appl. Geophys.*, *173*(8), 2621–2636, doi:10.1007/s00024-016-1319-7.

Chaussard, E., R. Bürgmann, M. Shirzaei, E. J. Fielding, and B. Baker (2014), Predictability of hydraulic head changes and characterization of aquifer-system and fault properties from InSAR-derived ground deformation, *J. Geophys. Res. Solid Earth*, *119*(8), 6572–6590, doi:10.1002/2014JB011266.

Chen, C. T., J. C. Hu, C. Y. Lu, J. C. Lee, and Y. C. Chan (2007), Thirty-year land elevation change from subsidence to uplift following the termination of groundwater pumping and its geological implications in the Metropolitan Taipei Basin, Northern Taiwan, *Eng. Geol.*, *95*(1–2), 30–47, doi:10.1016/j.enggeo.2007.09.001.

Chen, J., R. Knight, H. A. Zebker, and W. A. Schreüder (2016), Confined aquifer head measurements and storage properties in the San Luis Valley, Colorado, from spaceborne InSAR observations, *Water Resour. Res.*, *52*(5), 3623–3636, doi:10.1002/2015WR018466.

Christopher Torrence, G. P. C. (1998), A Practical Guide to Wavelet Analysis, *Bull. Am. Meteorol. Soc.*, *79*(1), 61–78, doi:http://dx.doi.org/10.1175/1520-0477(1998)079<0061:APGTWA>2.0.CO;2.

Clement, M. A., C. G. Kilsby, and P. Moore (2017), Multi-temporal synthetic aperture radar flood mapping using change detection, *J. Flood Risk Manag.*, doi:10.1111/jfr3.12303.

Comninou, M., and J. Dundurs (1975), The angular dislocation in a half space, *J. Elast.*, *5*(3–4), 203–216, doi:10.1007/BF00126985.

Conway, B. (2013), *Land Subsidence Monitoring Report, ADWR*, Phoenix, AZ.

Conway, B. D. (2015), Land subsidence and earth fissures in south-central and southern Arizona, USA, *Hydrogeol. J.*, *24*(3), 649–655, doi:10.1007/s10040-015-1329-z.

Cooper, H. (1966), The equation of groundwater flow in fixed and deforming coordinates, *J. Geophys. Res.*, *71*(20), 4785–4790, doi:10.1029/JZ071i020p04785.

Coplin, L.S., Galloway, D. (eds) (1999), Houston-Galveston, Texas: Land Subsidence in the United States, *U.S. Geol. Surv. Circ.*, *1182*, 35–48.

Corkhill, E., S. Corell, B. Hill, and D. Carr (1993), *A Regional Groundwater Flow Model of the Salt River Valley - Phase I: Phoenix Active Management Area Hydrogeologic Framework and Basic Data Report, ADWR*, Phoenix, AZ.

Cox, S. C., H. K. Rutter, A. Sims, M. Manga, J. J. Weir, T. Ezzy, P. A. White, T. W. Horton, and D. Scott (2012), Hydrological effects of the M w 7.1 Darfield (Canterbury) earthquake, 4 September 2010, New Zealand, *New Zeal. J. Geol. Geophys.*, *55*(3), 231–247, doi:10.1080/00288306.2012.680474.

Cubrinovski, M., J. D. Bray, M. Taylor, S. Giorgini, B. A. Bradley, L. Wotherspoon, and J. Zupan (2011), Soil Liquefaction Effects in the Central Business District during the February 2011 Christchurch Earthquake, *Seismol. Res. Lett.*, *82*(6), 893–904, doi:10.1785/gssrl.

Cubrinovski, M., K. Robinson, M. Taylor, M. Hughes, and R. Orense (2012), Lateral spreading and its impacts in urban areas in the 2010-2011 Christchurch earthquakes, *New Zeal. J. Geol. Geophys.*, *55*(3), 255–269, doi:10.1080/00288306.2012.699895.

Cunningham, W. L., and C. W. Schalk (2011), *Groundwater technical procedures of the U.S . Geological Survey Techniques and Methoda 1-A1*, U.S. Geological Survey, Reston, VA.

D.M., A., B. Reguera, G. C. Pitcher, and H. O. Enevoldsen (2011), *Guidebook to studies of land subsidence due to ground-water withdrawal*, UNESCO, Paris.

Davis, T., J. Dieckhoff, and S. Stuk (2014), *Statewide Groundwater Level Changes in Arizona, Water Years 1993 to 2013, 2003 to 2013, and 2012 to 2013, ADWR Open File Report No. 13*, Phoenix, AZ.

Day, J. W. et al. (2007), Restoration of the Mississippi Delta: Lessons from Hurricanes Katrina and Rita, *Science (80-.).*, *315*(5819), 1679–1684, doi:10.1126/science.1137030.

DeCaonto, R. M., and D. Pollard (2016), Contribution of Antartica to past and future sea-level rise, *Nature*, *531*, 1–21.

Desai, S. D., W. Bertiger, J. Gross, B. Haines, N. Harvey, C. Selle, a Sibthorpe, and J. P. Weiss (2011), Results from the Reanalysis of Global GPS Data in the IGS08 Reference Frame, *AGU Fall Meet.*, 1.

Dixon, T. H., F. Amelung, A. Ferretti, F. Novali, F. Rocca, R. Dokka, G. Sella, S. W. Kim, S. Wdowinski, and D. Whitman (2006), Space geodesy: Subsidence and flooding in New Orleans, *Nature*, *441*(7093), 587–588, doi:10.1038/441587a.

Dokka, R. K. (2006), Modern-day tectonic subsidence in coastal Louisiana, *Geology*, *34*(4), 281–284, doi:10.1130/G22264.1.

Dubas, L. (2010), *Geological Update for the Combined SRV and Lower Hassayampa Regional Groundwater Flow Model Areas in the Phoenix AMA, ADWR*, Phoenix, AZ.

Elkhoury, J. E., E. E. Brodsky, and D. C. Agnew (2006), Seismic waves increase permeability, *Nature*, *441*(7097), 1135–1138, doi:10.1038/nature04798.

Emanuel, K. (2017), Assessing the present and future probability of Hurricane Harvey's rainfall, *Proc. Natl. Acad. Sci.*, *114*(48), 201716222, doi:10.1073/pnas.1716222114.

Epstein, V. J. (1987), *Hydrologic and geologic factors affecting land subsidence near Eloy, Arizona,* USGS Numbered Series: Water-Resources Investigations Report 87-4143, Tuscon, AZ.

Evans, D. W., and D. R. Pool (2000), Aquifer compaction and ground-water levels in south-central Arizona, *USGS Water-Resources Investig. Rep. 99-4249*, (USGS Numbered Series), vi, 54 p.   :ill., maps; 28 cm.

Farr, T. G., P. A. Rosen, E. Caro, R. Crippen, R. Duren, S. Hensley, M. Kobrick, M. Paller, E. Rodriguez, and L. Roth (2007), The shuttle radar topography mission, *Rev. Geophys.*, *45*(2).

Faunt, C. C., R. T. Hanson, K. Belitz, W. Schmid, S. P. Predmore, D. L. Rewis, and K. McPherson (2009), *Groundwater Availability of the Central Valley Aquifer, California*.

Ferretti, A., C. Prati, and F. Rocca (2000), Nonlinear subsidence rate estimation using permanent scatterers in differential SAR interferometry, *IEEE Trans. Geosci. Remote Sens.*, *38*(5 I), 2202–2212, doi:10.1109/36.868878.

Fielding, E. J., R. G. Blom, and R. M. Goldstein (1998), Rapid subsidence over oil fields measured by SAR interferometry, *Geophys. Res. Lett.*, *25*(17), 3215–3218, doi:10.1029/98GL52260.

Forsyth, P. J., D. J. A. Barrell, and R. Jongens (2008), 1:250 000 Geological Map 16: Geology of the Christchurch Area, *Low. Hutt, New Zeal.*, 1–67.

Franchioni, G., and R. Lanari (1999), *Synthetic Aperture Radar Processing*, CRC Press, Boca Raton, FL.

Freihoefer, A., D. Mason, P. Jahnke, L. Dubas, and K. Hutchinson (2009), *Regional groundwater flow model of the Salt River Valley Phoenix Active Management Area model update and calibration, ADWR*, Phoenix, AZ.

Galloway, D., D. R. Jones, and S. E. Ingebritsen (1999), *Land subsidence in the United States*.

Galloway, D. L., and T. J. Burbey (2011), Review: Regional land subsidence accompanying groundwater extraction, *Hydrogeol. J.*, *19*(8), 1459–1486, doi:10.1007/s10040-011-0775-5.

Galloway, D. L., K. W. Hudnut, S. E. Ingebritsen, S. P. Phillips, G. Peltzer, F. Rogez, and P. a. Rosen (1998), Detection of aquifer system compaction and land subsidence using interferometric synthetic aperture radar, Antelope Valley, Mojave Desert, California, *Water Resour. Res.*, *34*(10), 2573–2585, doi:10.1029/98WR01285.

Galloway, D. L., L. S. Coplin, and S. E. Ingebritsen (2003), Effects of land subsidence in the greater Houston area, *Manag. Urban Water Supply*, 187–203, doi:10.1007/978-94-017-0237-9_12.

Garcia-Fresca, B., and J. M. . J. Sharp (2005), Reviews in Engineering Geology XVI: Humans as Geologic Agents, in *Humans As Geologic Agents*, vol. 16, edited by J. Ehlen, W. Haneberg, and R. Larson, pp. 123–136, Geological Society of America, Inc., Boulder, Colorado.

Geballe, Z. M., C. Y. Wang, and M. Manga (2011), A permeability-change model for water-level changes triggered by teleseismic waves, *Geofluids*, *11*(3), 302–308, doi:10.1111/j.1468-8123.2011.00341.x.

GIPSY-OASIS (2016), GNSS-Inferred Positioning System and Orbit Analysis Software, *Https://Gipsy-Oasis.Jpl.Nasa.*

Green, D. H., and H. F. Wang (1990), Specific storage as a poroelastic coefficient, *Water Resour. Res.*, *26*(7), 1631–1637, doi:10.1029/WR026i007p01631.

Gulley, A. K., N. F. Dudley Ward, S. C. Cox, and J. P. Kaipio (2013), Groundwater responses to the recent Canterbury earthquakes: A comparison, *J. Hydrol.*, *504*, 171–181, doi:10.1016/j.jhydrol.2013.09.018.

H.Wang (2000), *Theory of linear poroelasicity with applications to geomechanics and hydrogeology*, Princeton University Press, Princeton, NJ.

Hanson, R. T. (1989), Aquifer-system compaction, Tucson Basin and Avra Valley, Arizona, *Water-Resources Investig. Rep. 88-4172*, (USGS Numbered Series), vi, 69 p. :ill., maps;28 cm.

Hanson, S., R. Nicholls, N. Ranger, S. Hallegatte, J. Corfee-Morlot, C. Herweijer, and J. Chateau (2011), A global ranking of port cities with high exposure to climate extremes, *Clim. Change*, *104*(1), 89–111, doi:10.1007/s10584-010-9977-4.

Hanssen, R. F. (2001), *Radar interferometry: data interpretation and error analysis*, Kluwer Academic Publishers, Ney York.

Harris, R. A., and P. Segall (1987), Detection of a locked zone at depth on the Parkfield, California, segment of the San Andreas Fault, *J. Geophys. Res.*, *92*(B8), 7945, doi:10.1029/JB092iB08p07945.

Haupt, R. L., and S. E. Haupt (2004), *Practical Genetic Algorithms Second Edition*, John Wiley & Sons, Hoboken, NJ.

Helm, D. C. (1976), One- dimensional simulation of aquifer system compaction near Pixley, California: 2. Stress- Dependent Parameters, *Water Resour. Res.*, *12*(3), 375–391, doi:10.1029/WR012i003p00375.

Hernandez-Marin, M., and T. J. Burbey (2010), Controls on initiation and propagation of pumping-induced earth fissures: insights from numerical simulations, *Hydrogeol. J.*, *18*(8), 1773–1785, doi:10.1007/s10040-010-0642-9.

Hetland, E. A., P. Musé, M. Simons, Y. N. Lin, P. S. Agram, and C. J. Dicaprio (2012), Multiscale InSAR Time Series (MInTS) analysis of surface deformation, *J. Geophys. Res. Solid Earth*, *117*(2), B02404, doi:10.1029/2011JB008731.

Hipke, W. (2007), *East Valley Water Forum Scenarios for the East Salt River Valley Sub-basin an Application of the Regional Groundwater Flow Model of the Salt River Valley, Arizona, ADW*R, Phoenix, AZ.

Hirabayashi, Y., R. Mahendran, S. Koirala, L. Konoshima, D. Yamazaki, S. Watanabe, H. Kim, and S. Kanae (2013), Global flood risk under climate change, *Nat. Clim. Chang.*, *3*(9), 816–821, doi:10.1038/nclimate1911.

Hoffmann, J., H. A. Zebker, D. L. Galloway, and F. Amelung (2001), Seasonal subsidence and rebound in Las Vegas Valley, Nevada, observed by synthetic aperture radar interferometry, *Water Resour. Res.*, *37*(6), 1551–1566, doi:10.1029/2000WR900404.

Hoffmann, J., D. L. Galloway, and H. A. Zebker (2003a), Inverse modeling of interbed storage parameters using land subsidence observations, Antelope Valley, California, *Water Resour. Res.*, *39*(2), 1039, doi:10.1029/2001WR001252.

Hoffmann, J., S. A. Leake, D. L. Galloway, and A. . Wilson (2003b), MODFLOW-2000 ground-water model—User guide to the Subsidence and Aquifer-System Compaction (SUB) Package, *US Geol. Surv. Open-File Rep. 03*, (USGS Ground-Water Resources Program), 46.

Holzer, T. L. (1981), Preconsolidation stress of aquifer systems in areas of induced land subsidence, *Water Resour. Res.*, *17*(3), 693–703, doi:10.1029/WR017i003p00693.

Holzer, T. L., and R. L. Bluntzer (1984), Holzer et al 1984-Land Subsidence Near Oil and Gas Fields, Houston, Texas, *Groundwater*, *22*(4), 450–459.

Holzer, T. L., and D. L. Galloway (2005), Impacts of land subsidence caused by withdrawal of underground fluids in the United States, in *Reviews in Engineering Geology XVI: Humans as Geologic Agents*, vol. 16, edited by J. Ehlen, W. Haneberg, and R. Larson, pp. 87–99, Geological Society of America, Inc., Boulder, Colorado.

Huffman, A. C., S. A. Kinney, L. R. H. Biewick, H. R. Mitchell, and G. L. Gunther (2004), Salt diapirs in the Gulf Coast, *US Geol. Surv. DS-90-A*, *Version 1*.

Ingebritsen, S. E., and D. L. Galloway (2014), Coastal subsidence and relative sea level rise, *Environ. Res. Lett.*, *9*(9), 091002, doi:10.1088/1748-9326/9/9/091002.

IPCC Working Group 1 (2014), Summary for Policymakers, in *Climate Change 2013 - The Physical Science Basis*, edited by Intergovernmental Panel on Climate Change, pp. 1–30, Cambridge University Press, Cambridge.

Jachens, R. C., and T. L. Holzer (1982), Differential compaction mechanism for earth fissures near Casa Grande, Arizona., *Geol. Soc. Am. Bull.*, *93*(10), 998–1012, doi:10.1130/0016-7606(1982)93<998:DCMFEF>2.0.CO;2.

Jacob, C. E. (1940), On the flow of water in an elastic artesian aquifer, *Eos, Trans. Am. Geophys. Union*, *21*(2), 574–586, doi:10.1029/TR021i002p00574.

Jacobs, K. L., and J. M. Holway (2004), Managing for sustainability in an arid climate: Lessons learned from 20 years of groundwater management in Arizona, USA, *Hydrogeol. J.*, *12*(1), 52–65, doi:10.1007/s10040-003-0308-y.

Jamero, M. L., M. Onuki, M. Esteban, X. K. Billones-Sensano, N. Tan, A. Nellas, H. Takagi, N. D. Thao, and V. P. Valenzuela (2017), Small-island communities in the Philippines prefer local measures to relocation in response to sea-level rise, *Nat. Clim. Chang.*, *7*(8), 581–586, doi:10.1038/NCLIMATE3344.

Jang, C. S., C. W. Liu, Y. Chia, L. H. Cheng, and Y. C. Chen (2008), Changes in hydrogeological properties of the River Choushui alluvial fan aquifer due to the 1999

Chi-Chi earthquake, Taiwan, *Hydrogeol. J.*, *16*(2), 389–397, doi:10.1007/s10040-007-0233-6.

Jenny, J. P., and S. J. Reynolds (Eds.) (1989), *Geologic evolution of Arizona*, Digest 17., Arizona Geological Society, Tuscon, AZ.

Jongens, R., D. J. A. Barrell, J. K. Campbell, and J. R. Pettinga (2012), Faulting and folding beneath the Canterbury Plains identified prior to the 2010 emergence of the Greendale Fault, *New Zeal. J. Geol. Geophys.*, *55*(3), 169–176, doi:10.1080/00288306.2012.674050.

Jongman, B., S. Hochrainer-Stigler, L. Feyen, J. C. J. H. Aerts, R. Mechler, W. J. W. Botzen, L. M. Bouwer, G. Pflug, R. Rojas, and P. J. Ward (2014), Increasing stress on disaster-risk finance due to large floods, *Nat. Clim. Chang.*, *4*(4), 264–268, doi:10.1038/nclimate2124.

Jónsson, S., P. Segall, R. Pedersen, and G. Björnsson (2003), Post-earthquake ground movements correlated to pore-pressure transients, *Nature*, *424*(6945), 179–183, doi:10.1038/nature01776.

K. Terzaghi (1925), Principles of soil mechanics. IV. Settlement and consolidation of clay, *eering News-Record*, *95*(95), 874–878.

Kearns, T. J., G. Wang, Y. Bao, J. Jiang, and D. Lee (2015), Current Land Subsidence and Groundwater Level Changes in the Houston Metropolitan Area (2005–2012), *J. Surv. Eng.*, *141(4)*(4), 46–62, doi:10.1061/(ASCE)SU.1943-5428.0000147.

Khan, S. D. (2005), Urban development and flooding in Houston, Texas, inferences from remote sensing data using neural network technique, *Environ. Geol.*, *47*(8), 1120–1127, doi:DOI 10.1007/s00254-005-1246-x.

Kim, J. W., Z. Lu, Y. Jia, and C. K. Shum (2015), Ground subsidence in Tucson, Arizona, monitored by time-series analysis using multi-sensor InSAR datasets from 1993 to 2011, *ISPRS J. Photogramm. Remote Sens.*, *107*, 126–141, doi:10.1016/j.isprsjprs.2015.03.013.

Knutson, T. R., J. L. McBride, J. Chan, K. Emanuel, G. Holland, C. Landsea, I. Held, J. P. Kossin, A. K. Srivastava, and M. Sugi (2010), Tropical cyclones and climate change, *Nat. Geosci.*, *3*(3), 157–163, doi:10.1038/ngeo779.

Konikow, L. F., and E. Kendy (2005), Groundwater depletion: A global problem, *Hydrogeol. J.*, *13*(1), 317–320, doi:10.1007/s10040-004-0411-8.

Lin, N., K. Emanuel, M. Oppenheimer, and E. Vanmarcke (2012), Physically based assessment of hurricane surge threat under climate change, *Nat. Clim. Chang.*, *2*(6), 462–467, doi:10.1038/nclimate1389.

Liscum, F. (2001), Effects of urban development on stormwater runoff characteristics for the Houston, Texas, metropolitan area, *USGS Numbered Ser. Water-Resources Investig. Rep. 01-4071*, 1–35.

Liu, W., and M. Manga (2009), Changes in permeability caused by dynamic stresses in fractured sandstone, *Geophys. Res. Lett.*, *36*(20), L20307, doi:10.1029/2009GL039852.

Liu, Y., and D. C. Helm (2008), Inverse procedure for calibrating parameters that control land subsidence caused by subsurface fluid withdrawal: 1. Methods, *Water Resour. Res.*, *44*(7), n/a-n/a, doi:10.1029/2007WR006605.

Long, S., T. E. Fatoyinbo, and F. Policelli (2014), Flood extent mapping for Namibia using change detection and thresholding with SAR, *Environ. Res. Lett.*, *9*(3), 035002, doi:10.1088/1748-9326/9/3/035002.

Manga, M., and E. Brodsky (2006), SEISMIC TRIGGERING OF ERUPTIONS IN THE FAR FIELD: Volcanoes and Geysers, *Annu. Rev. Earth Planet. Sci.*, *34*(1), 263–291, doi:10.1146/annurev.earth.34.031405.125125.

Manga, M., and C. Y. Wang (2007), Earthquake Hydrology, in *Treatise on Geophysics*, vol. 4, pp. 293–320.

Manga, M., I. Beresnev, E. E. Brodsky, J. E. Elkhoury, D. Elsworth, S. E. Ingebritsen, D. C. Mays, and C. Y. Wang (2012), Changes in permeability caused by transient stresses: Field observations, experiments, and mechanisms, *Rev. Geophys.*, *50*(2), doi:10.1029/2011RG000382.

Manga, M., C. Y. Wang, and M. Shirzaei (2016), Increased stream discharge after the 3 September 2016 Mw 5.8 Pawnee, Oklahoma earthquake, *Geophys. Res. Lett.*, *43*(22), 11,588-11,594, doi:10.1002/2016GL071268.

Mason, D., and L. Bota (2006), Regional groundwater flow model of the Tucson Active Management Area Tucson, Arizona: simulation and application, *Arizona Dep. Water Resour. Model. Rep. No. 24*, 159.

Megdal, S. B. (2007), Arizona's recharge and recovery programs, in *Arizona Water Policy: Management Innovations in an Urbanizing, Arid Region*, edited by B. G. Colby and K. L. Jacobs, pp. 188–203, Resources for the Future, Washington DC.

Megdal, S. B., and A. Forrest (2015), How a drought-resilient water delivery system rose out of the desert: The case of Tucson Water, *J. Am. Water Works Assoc.*, *107*(9), 46–52, doi:10.5942/jawwa.2015.107.0136.

Meyer, P. L. (1970), *Introductory probability and statistical applications*, Addison-Wesley Pub. Co.

Mikhail, E. M., F. Ackermann, and F. Leberl (1978), *Observations and Least Squares*, University Press of America, University of Michigan, Ann Arbor, MI.

Miller, M. M., and M. Shirzaei (2015), Spatiotemporal characterization of land subsidence and uplift in Phoenix using InSAR time series and wavelet transforms, *J. Geophys. Res. B Solid Earth*, *120*(8), 5822–5842, doi:10.1002/2015JB012017.

Miller, M. M., M. Shirzaei, and D. Argus (2017), Aquifer Mechanical Properties and Decelerated Compaction in Tucson, Arizona, *J. Geophys. Res. Solid Earth*, doi:10.1002/2017JB014531.

Morehouse, B. J., R. H. Carter, and P. Tschakert (2002), Sensitivity of urban water resources in Phoenix, Tucson, and Sierra Vista, Arizona, to severe drought, *Clim. Res.*, *21*(3), 283–297, doi:10.3354/cr021283.

Morton, R. A., J. C. Bernier, and J. A. Barras (2006), Evidence of regional subsidence and associated interior wetland loss induced by hydrocarbon production, Gulf Coast region, USA, *Environ. Geol.*, *50*(2), 261–274, doi:10.1007/s00254-006-0207-3.

Mossop, A., and P. Segall (1997), Subsidence at the Geysers geothermal field, N. California from a comparison of GPS and leveling surveys, *Geophys. Res. Lett.*, *24*(14), 1839–1842, doi:10.1029/97GL51792.

Mossop, A., and P. Segall (1999), Volume strain within The Geysers geothermal field, *J. Geophys. Res.*, *104*(B12), 29113, doi:10.1029/1999JB900284.

Mousavi, M. E., J. L. Irish, A. E. Frey, F. Olivera, and B. L. Edge (2011), Global warming and hurricanes: the potential impact of hurricane intensification and sea level rise on coastal flooding, *Clim. Change*, *104*(3–4), 575–597, doi:10.1007/s10584-009-9790-0.

Muir-Wood, R., and G. C. P. King (1993), Hydrological signatures of earthquake strain, *J. Geophys. Res.*, *98*(B12), 22035, doi:10.1029/93JB02219.

Nicholls, R., and A. Cazenave (2003), Sea-Level Rise and Its Impact on Coastal Zones, *Science*, *328*(August), doi:10.1126/science.1185782.

Okada, Y. (1992), Internal deformation due to shear and tensile faults in a half-space, *Bull. Seismol. Soc. Am.*, *82*(2), 1018–1040.

van Oldenborgh, G. J., K. van der Wiel, A. Sebastian, R. Singh, J. Arrighi, F. Otto, K. Haustein, S. Li, G. Vecchi, and H. Cullen (2017), Attribution of extreme rainfall from Hurricane Harvey, August 2017, *Environ. Res. Lett.*, *12*(12), 124009, doi:10.1088/1748-9326/aa9ef2.

Papadopoulos, G., and G. Lefkopoulos (1993), Magnitude-distance relations for liquefaction in soil from earthquakes, *Bull. Seismol. Soc. Am.*, *83*(3), 925–938, doi:10.1016/0148-9062(94)92335-3.

Pavelko, M. T. (2004), Estimates of hydraulic properties from a one-dimensional numerical model of vertical aquifer-system deformation, Lorenzi site, Las Vegas, Nevada, *USGS Water-Resources Investig. Rep.*, *03*(4083), 45.

Poland, J. F., and G. H. Davis (1969), Land Subsidence Due To Withdrawal of Fluids, *Rev. Eng. Geol.*, *2*, 187–270, doi:10.1130/REG2-p187.

Poland, J. F., and R. L. Ireland (1988), *Land subsidence in the Santa Clara Valley, California, as of 1982, USGS Numbered Series 497-F*, Washington DC.

Preisig, G., F. J. Cornaton, and P. Perrochet (2014), Regional flow and deformation analysis of basin-fill aquifer systems using stress-dependent parameters, *Groundwater*, *52*(1), 125–135, doi:10.1111/gwat.12034.

Qu, F., Z. Lu, Q. Zhang, G. W. Bawden, J. W. Kim, C. Zhao, and W. Qu (2015), Mapping ground deformation over Houston-Galveston, Texas using multi-temporal InSAR, *Remote Sens. Environ.*, *169*, 290–306, doi:10.1016/j.rse.2015.08.027.

Quigley, M., R. Van Dissen, N. Litchfield, P. Villamor, B. Duffy, D. Barrell, K. Furlong, T. Stahl, E. Bilderback, and D. Noble (2012), Surface rupture during the 2010 Mw 7.1 darfield(canterbury) earthquake: Implications for fault rupture dynamics and seismic-hazard analysis, *Geology*, *40*(1), 55–58, doi:10.1130/G32528.1.

Quigley, M. C., S. Bastin, and B. A. Bradley (2013), Recurrent liquefaction in Christchurch, New Zealand, during the Canterbury earthquake sequence, *Geology*, *41*(4), 419–422, doi:10.1130/G33944.1.

Reeves, J. A., R. Knight, H. A. Zebker, P. K. Kitanidis, and W. A. Schreüder (2014), Estimating temporal changes in hydraulic head using InSAR data in the San Luis Valley, Colorado, *Water Resour. Res.*, *50*(5), 4459–4473, doi:10.1002/2013WR014938.

Rehrl, T., and R. Friedrich (2006), Modelling long-term oil price and extraction with a Hubbert approach: The LOPEX model, *Energy Policy*, *34*(15), 2413–2428, doi:10.1016/j.enpol.2005.03.021.

Rencher, A. C. (2002), Principal Component Analysis, *Methods Multivar. Anal.*, *98*, 380–407, doi:10.1002/0471271357.ch12.

Reynolds, S. J., and R. D. Bartlett (2002), *Subsurface geology of the easternmost Phoenix basin, Arizona: Implications for groundwater flow*, Arizona Geological Survey Contributed Report CR-02-A, AZGS, Tuscon, AZ.

Rice, J. R., and M. P. Cleary (1976), Some basic stress diffusion solutions for fluid-saturated elastic porous media with compressible constituents, *Rev. Geophys.*, *14*(2), 227–241, doi:10.1029/RG014i002p00227.

Riley, F. S. (1969), Analysis of Borehole Extensometer Data from Central California, in *Land Subsidence, Volume 2*, edited by L. J. Tison, pp. 423–431, Symposium of Tokyo 1969.

Roeloffs, E. (1996), Poroelastic Techniques in the Study of Earthquake-Related Hydrologic Phenomena, *Adv. Geophys.*, *38*(C), 135–195, doi:10.1016/S0065-2687(08)60270-8.

Roeloffs, E. A. (1998), Persistent water level changes in a well near Parkfield, California, due to local and distant earthquakes, *J. Geophys. Res.*, *103*(B1), 869–889, doi:10.1029/97JB02335.

Rojstaczer, S., and S. Wolf (1992), Permeability changes associated with large earthquakes: an example from Loma Prieta, California, *Geology*, *20*(3), 211–214, doi:10.1130/0091-7613(1992)020<0211:PCAWLE>2.3.CO;2.

Rojstaczer, S., S. Wolft, and R. Michel (1995), Permeability enhancement in the shallow crust as a cause of earthquake-induced hydrological changes, *Nature*, *373*(6511), 237–239, doi:10.1038/373237a0.

Rosen, J. (2017), How an ocean climate cycle favored Harvey, *Science (80-.).*, *357*(6354), 853–855, doi:10.1126/science.357.6354.853.

Rudolph, D. L., and E. O. Frind (1991), Hydraulic response of highly compressible aquitards during consolidation, *Water Resour. Res.*, *27*(1), 17–30, doi:10.1029/90WR01700.

Rutter, H. K., S. C. Cox, N. F. Dudley Ward, and J. J. Weir (2016), Aquifer permeability change caused by a near-field earthquake, Canterbury, New Zealand, *Water Resour. Res.*, *52*(11), 8861–8878, doi:10.1002/2015WR018524.

Samsonov, S., and N. d'Oreye (2012), Multidimensional time-series analysis of ground deformation from multiple InSAR data sets applied to Virunga Volcanic Province, *Geophys. J. Int.*, *191*(3), 1095–1108, doi:10.1111/j.1365-246X.2012.05669.x.

Scanlon, B. R., Z. Zhang, R. C. Reedy, D. R. Pool, H. Save, D. Long, J. Chen, D. M. Wolock, B. D. Conway, and D. Winester (2015), Hydrologic implications of GRACE satellite data in the Colorado River Basin, *Water Resour. Res.*, *51*(12), 9891–9903, doi:10.1002/2015WR018090.

Scanlon, B. R., R. C. Reedy, C. C. Faunt, D. Pool, and K. Uhlman (2016), Enhancing drought resilience with conjunctive use and managed aquifer recharge in California and Arizona, *Environ. Res. Lett.*, *11*(3), 035013, doi:10.1088/1748-9326/11/3/035013.

Schmid, R., P. Steigenberger, G. Gendt, M. Ge, and M. Rothacher (2007), Generation of a consistent absolute phase-center correction model for GPS receiver and satellite antennas, *J. Geod.*, *81*(12), 781–798, doi:10.1007/s00190-007-0148-y.

Schmid, R., T. U. München, F. Dilssner, R. Dach, M. Schmitz, and G. Gmbh (2010), Updated phase center corrections for satellite and receiver antennas, in *paper presented at IGS workshop, Int. GNSS Serv., Newcastle, U.K.*

Schmidt, D. A., and R. Bürgmann (2003), Time-dependent land uplift and subsidence in the Santa Clara valley, California, from a large interferometric synthetic aperture radar data set, *J. Geophys. Res. Solid Earth*, *108*(B9), 2416, doi:10.1029/2002JB002267.

Schumann, H. H., and S. R. Andserson (1988), *Land-subsidence measurements and aquifer-compaction monitoring in Tucson Basin and Avra Valley, Arizona*, USGS Numbered Series: Water-Resources Investigations Report 86-4167, Tuscon, AZ.

Sheng, Z., D. C. Helm, and J. Li (2003), Mechanisms of earth fissuring caused by groundwater withdrawal, *Environ. Eng. Geosci.*, *9*(4), 351–362, doi:10.2113/9.4.351.

Shirzaei, M. (2013), A wavelet-based multitemporal DInSAR algorithm for monitoring ground surface motion, *IEEE Geosci. Remote Sens. Lett.*, *10*(3), 456–460, doi:10.1109/LGRS.2012.2208935.

Shirzaei, M., and R. Bürgmann (2012), Topography correlated atmospheric delay correction in radar interferometry using wavelet transforms, *Geophys. Res. Lett.*, *39*(1), L01305, doi:10.1029/2011GL049971.

Shirzaei, M., and R. Bürgmann (2013), Time-dependent model of creep on the Hayward fault from joint inversion of 18 years of InSAR and surface creep data, *J. Geophys. Res. Solid Earth*, *118*(4), 1733–1746, doi:10.1002/jgrb.50149.

Shirzaei, M., and T. R. Walter (2009), Randomly iterated search and statistical competency as powerful inversion tools for deformation source modeling: Application to volcano interferometric synthetic aperture radar data, *J. Geophys. Res. Solid Earth*, *114*(10), B10401, doi:10.1029/2008JB006071.

Shirzaei, M., and T. R. Walter (2011), Estimating the effect of satellite orbital error using wavelet-based robust regression applied to InSAR deformation data, *IEEE Trans. Geosci. Remote Sens.*, *49*(11 PART 2), 4600–4605, doi:10.1109/TGRS.2011.2143419.

Shirzaei, M., R. Bürgmann, J. Foster, T. R. Walter, and B. A. Brooks (2013a), Aseismic deformation across the Hilina fault system, Hawaii, revealed by wavelet analysis of InSAR and GPS time series, *Earth Planet. Sci. Lett.*, *376*, 12–19, doi:10.1016/j.epsl.2013.06.011.

Shirzaei, M., T. R. Walter, and R. Bürgmann (2013b), Coupling of Hawaiian volcanoes only during overpressure condition, *Geophys. Res. Lett.*, *40*(10), 1994–1999, doi:10.1002/grl.50470.

Shirzaei, M., W. L. Ellsworth, K. F. Tiampo, P. J. Gonzalez, and M. Manga (2016), Surface uplift and time-dependent seismic hazard due to fluid injection in eastern Texas, *Science (80-.).*, *353*(6306), 1416–1419, doi:10.1126/science.aag0262.

Shirzaei, M., R. Bürgmann, and E. J. Fielding (2017), Applicability of Sentinel-1 Terrain Observation by Progressive Scans multitemporal interferometry for monitoring slow ground motions in the San Francisco Bay Area, *Geophys. Res. Lett.*, *44*(6), 2733–2742, doi:10.1002/2017GL072663.

Shultz, J. M., S. Galea, N. F, and C. SF (2017), Mitigating the Mental and Physical Health Consequences of Hurricane Harvey, *Jama*, *21*(4), 357–368, doi:10.1001/jama.2017.14618.

Sibson, R., F. Ghisetti, and J. Ristau (2011), Stress Control of an Evolving Strike-Slip Fault System during the 2010-2011 Canterbury, New Zealand, Earthquake Sequence, *Seismol. Res. Lett.*, *82*(6), 824–832, doi:10.1785/gssrl.82.6.824.

Sibthorpe, A., J. Weiss, N. Harvey, D. Kuang, and Y. Bar-Sever (2010), Empirical modeling of solar radiation pressure forces affecting GPS satellites, *AGU Fall Meet.*, 16.

Skopp, J. (1999), *Physical and Chemical Hydrogeology, 2nd edition*, 2nd ed., Elsevier Science B.V., Amsterdam.

Smith, R. G., R. Knight, J. Chen, J. A. Reeves, H. A. Zebker, T. Farr, and Z. Liu (2017), Estimating the permanent loss of groundwater storage in the southern San Joaquin Valley, California, *Water Resour. Res.*, *53*(3), 2133–2148, doi:10.1002/2016WR019861.

Sneed, B. M. (2001), Hydraulic and Mechanical Properties Affecting Ground-Water Flow and Aquifer- System Compaction , San Joaquin Valley , California, *Director*, *1*, 26.

Sun, H., D. Grandstaff, and R. Shagam (1999), Land subsidence due to groundwater withdrawal: Potential damage of subsidence and sea level rise in southern New Jersey, USA, *Environ. Geol.*, *37*(4), 290–296, doi:10.1007/s002540050386.

Svoboda, M. et al. (2002), The drought monitor, *Bull. Am. Meteorol. Soc.*, *83*(8), 1181–1190, doi:10.1175/1520-0477(2002)083<1181:TDM>2.3.CO;2.

Theis, C. V. (1935), The relation between the lowering of the Piezometric surface and the rate and duration of discharge of a well using ground???water storage, *Eos, Trans. Am. Geophys. Union*, *16*(2), 519–524, doi:10.1029/TR016i002p00519.

Tillman, F. D., and S. A. Leake (2010), Trends in groundwater levels in wells in the active management areas of Arizona, USA, *Hydrogeol. J.*, *18*(6), 1515–1524, doi:DOI 10.1007/s10040-010-0603-3.

Townsend, D. et al. (2016), Mapping surface liquefaction caused by the September 2010 and February 2011 Canterbury earthquakes: a digital dataset, *New Zeal. J. Geol. Geophys.*, *59*(4), 496–513, doi:10.1080/00288306.2016.1182929.

Vörösmarty, C. J., P. Green, J. Salisbury, and R. B. Lammers (2000), Global water resources: vulnerability from climate change and population growth., *Science*, *289*(5477), 284–8, doi:10.1126/SCIENCE.289.5477.284.

Wallace, L. M., J. Beavan, R. McCaffrey, K. Berryman, and P. Denys (2007), Balancing the plate motion budget in the South Island, New Zealand using GPS, geological and seismological datas, *Geophys. J. Int.*, *168*(1), 332–352, doi:10.1111/j.1365-246X.2006.03183.x.

Wang, C., Wang, C. and M. M. (2004), Coseismic release of water from mountains evidence from the (M=7.5) Chi Chi, Taiwan., *Earthq. Geol.*, *32*(9), 769–772.

Wang, C., M. Manga, M. Shirzaei, M. Weingarten, and L. Wang (2017), Induced Seismicity in Oklahoma Affects Shallow Groundwater, *Seismol. Res. Lett.*, *88*(4), 956–962, doi:10.1785/0220170017.

Wang, C. Y., X. Liao, L. P. Wang, C. H. Wang, and M. Manga (2016), Large earthquakes create vertical permeability by breaching aquitards, *Water Resour. Res.*, *52*(8), 5923–5937, doi:10.1002/2016WR018893.

Wang, J., W. Gao, S. Xu, and L. Yu (2012), Evaluation of the combined risk of sea level rise, land subsidence, and storm surges on the coastal areas of Shanghai, China, *Clim. Change*, *115*(3–4), 537–558, doi:10.1007/s10584-012-0468-7.

Wang, R., and H. Kümpel (2003), Poroelasticity: Efficient modeling of strongly coupled, slow deformation processes in a multilayered half-space, *Geophysics*, *68*(2), 705–717, doi:10.1190/1.1567241.

Warner, N. N., and P. E. Tissot (2012), Storm flooding sensitivity to sea level rise for Galveston Bay, Texas, *Ocean Eng.*, *44*, 23–32, doi:10.1016/J.OCEANENG.2012.01.011.

Williamson, A. K., D. E. Prudic, and L. A. Swain (1989), Ground-water flow in the Central Valley, California, *J. Name United States Geol. Surv. Prof. Pap. (USA); J. Vol. 1401-D*, Medium: X; Size: Pages: D1-D127.

Wilson, D. D. (1973), Significance of Geology in Some Current Water Resource Problems, Canterbury Plains, New Zealand., *J. Hydrol. New Zeal.*, *12*(2), 103–118.

Woodruff, J. D., J. L. Irish, and S. J. Camargo (2013), Coastal flooding by tropical cyclones and sea-level rise, *Nature*, *504*(7478), 44–52, doi:10.1038/nature12855.

Zhang, Y., J. Yu, X. Gong, J. Wu, and Z. Wang (2017), Pumping-induced stress and strain in aquifer systems in Wuxi, China, *Hydrogeol. J.*, doi:10.1007/s10040-017-1697-7.

Zhou, X., and T. J. Burbey (2014), Pore-pressure response to sudden fault slip for three typical faulting regimes, *Bull. Seismol. Soc. Am.*, *104*(2), 793–808, doi:10.1785/0120130139.

Zumberge, J. F., M. B. Heflin, D. C. Jefferson, M. M. Watkins, and F. H. Webb (1997), Precise point positioning for the efficient and robust analysis of GPS data from large networks, *J. Geophys. Res. Solid Earth*, *102*(B3), 5005–5017, doi:10.1029/96JB03860.

APPENDIX A

HOUSTON DATA

Table S1) Frame ID and dates of ALOS L-band SAR images. Used for estimating pre-cyclone vertical land motion

ALOS Frame	Year	Month	Date
F560P176	2007	7	13
	2007	10	13
	2008	1	13
	2008	4	14
	2008	5	30
	2009	1	15
	2010	6	5
	2010	7	21
	2010	9	5
	2010	12	6
	2011	1	21
F570P175	2006	12	24
	2007	9	26
	2007	12	27
	2008	2	11
	2008	3	28
	2008	6	28
	2008	12	29
	2009	3	31
	2009	10	1
	2010	5	19
	2010	7	4
	2010	11	19
	2011	1	4
F570P176	2007	7	13
	2007	10	13
	2008	1	13
	2008	4	14
	2008	5	30
	2009	1	15
	2010	6	5
	2010	7	21
	2010	9	5
	2010	12	6

ALOS Frame	Year	Month	Date
F570P176	2011	1	21
F580P174	2006	12	7
	2007	6	9
	2007	9	9
	2007	12	10
	2008	1	25
	2008	4	26
	2009	6	14
	2009	9	14
	2009	12	15
	2010	3	17
	2010	5	2
	2010	6	17
	2010	9	17
	2010	12	18
F580P175	2006	12	24
	2007	9	26
	2007	12	27
	2008	2	11
	2008	3	28
	2008	6	28
	2008	12	29
	2009	3	31
	2009	10	1
	2010	5	19
	2010	7	4
	2010	11	19
	2011	1	4
F580P176	2007	7	13
	2007	10	13
	2008	1	13
	2008	4	14
	2008	5	30
	2009	1	15

ALOS Frame	Year	Month	Date
F580P176	2010	6	5
	2010	7	21
	2010	9	5
	2010	12	6
	2011	1	21
F590P174	2006	12	7
	2007	6	9
	2007	9	9
	2007	12	10
	2008	1	25
	2008	4	26
	2009	6	14
	2009	9	14
	2009	12	15
	2010	3	17
	2010	5	2
	2010	6	17

ALOS Frame	Year	Month	Date
F590P174	2010	9	17
	2010	12	18
F590P175	2006	12	24
	2007	5	11
	2007	9	26
	2007	12	27
	2008	2	11
	2008	3	28
	2008	6	28
	2008	12	29
	2009	3	31
	2009	10	1
	2010	5	19
	2010	7	4
	2010	11	19
	2011	1	4

Table S2) ALOS interferometric pairs

ALOS Frame	Number of pairs	Image 1	Image 2	Perpendicular baseline (m)
F560P176	(47)	20070713	20071013	605.9
		20070713	20080113	960.9
		20070713	20080414	1733.4
		20070713	20080530	1501.8
		20070713	20090115	-1387.8
		20070713	20100605	910.9
		20070713	20100721	924.9
		20070713	20100905	1144.0
		20070713	20101206	1293.5
		20070713	20110121	1671.0
		20071013	20080113	355.0
		20071013	20080414	1127.5
		20071013	20080530	895.9
		20071013	20090115	-1993.7
		20071013	20100605	305.0
		20071013	20100721	319.0
		20071013	20100905	538.0
		20071013	20101206	687.5
		20071013	20110121	1065.0
		20080113	20080414	772.5
		20080113	20080530	540.9
		20080113	20100605	-50.0
		20080113	20100721	-36.0
		20080113	20100905	183.0
		20080113	20101206	332.5
		20080113	20110121	710.0
		20080414	20080530	-231.6
		20080414	20100605	-822.5
		20080414	20100721	-808.4
		20080414	20100905	-589.4
		20080414	20101206	-439.9
		20080414	20110121	-62.4
		20080530	20100605	-590.9
		20080530	20100721	-576.9
		20080530	20100905	-357.9
		20080530	20101206	-208.4
		20080530	20110121	169.1

		20100605	20100721	14.1
		20100605	20100905	233.1
		20100605	20101206	382.6
		20100605	20110121	760.1
		20100721	20100905	219.0
		20100721	20101206	368.5
		20100721	20110121	746.0
		20100905	20101206	149.5
		20100905	20110121	527.0
		20101206	20110121	377.5
F570P175	60	20061224	20070926	1607.1
		20061224	20071227	1915.3
		20061224	20080628	1022.9
		20061224	20081229	-285.0
		20061224	20090331	611.5
		20061224	20091001	1109.3
		20070926	20071227	308.2
		20070926	20080211	1175.4
		20070926	20080328	1175.4
		20070926	20080628	-584.2
		20070926	20081229	-1892.1
		20070926	20090331	-995.6
		20070926	20091001	-497.8
		20070926	20100519	622.2
		20070926	20100704	889.7
		20070926	20101119	1040.7
		20070926	20110104	1449.6
		20071227	20080211	867.2
		20071227	20080328	867.2
		20071227	20080628	-892.4
		20071227	20090331	-1303.8
		20071227	20091001	-806.0
		20071227	20100519	314.0
		20071227	20100704	581.5
		20071227	20101119	732.5
		20071227	20110104	1141.4
		20080211	20080328	0.0
		20080211	20080628	-1759.6
		20080211	20091001	-1673.2
		20080211	20100519	-553.2

		20080211	20100704	-285.6
		20080211	20101119	-134.6
		20080211	20110104	274.2
		20080328	20080628	-1759.6
		20080328	20091001	-1673.2
		20080328	20100519	-553.3
		20080328	20100704	-285.7
		20080328	20101119	-134.7
		20080328	20110104	274.2
		20080628	20081229	-1307.9
		20080628	20090331	-411.4
		20080628	20091001	86.4
		20080628	20100519	1206.4
		20080628	20100704	1474.0
		20080628	20101119	1625.0
		20081229	20090331	896.5
		20081229	20091001	1394.3
		20090331	20091001	497.8
		20090331	20100519	1617.8
		20090331	20100704	1885.3
		20091001	20100519	1120.0
		20091001	20100704	1387.5
		20091001	20101119	1538.6
		20091001	20110104	1947.4
		20100519	20100704	267.6
		20100519	20101119	418.6
		20100519	20110104	827.5
		20100704	20101119	151.0
		20100704	20110104	559.9
		20101119	20110104	408.9
F570P176	46	20070713	20071013	612.8
		20070713	20080113	977.1
		20070713	20080414	1760.6
		20070713	20080530	1531.9
		20070713	20090115	-1415.1
		20070713	20100605	925.3
		20070713	20100721	940.3
		20070713	20100905	1162.8
		20070713	20101206	1321.7
		20070713	20110121	1705.1

		20071013	20080113	364.3
		20071013	20080414	1147.8
		20071013	20080530	919.1
		20071013	20100605	312.4
		20071013	20100721	327.5
		20071013	20100905	550.0
		20071013	20101206	708.9
		20071013	20110121	1092.3
		20080113	20080414	783.5
		20080113	20080530	554.8
		20080113	20100605	-51.8
		20080113	20100721	-36.8
		20080113	20100905	185.7
		20080113	20101206	344.7
		20080113	20110121	728.0
		20080414	20080530	-228.7
		20080414	20100605	-835.3
		20080414	20100721	-820.3
		20080414	20100905	-597.8
		20080414	20101206	-438.8
		20080414	20110121	-55.5
		20080530	20100605	-606.6
		20080530	20100721	-591.6
		20080530	20100905	-369.1
		20080530	20101206	-210.1
		20080530	20110121	173.2
		20100605	20100721	15.1
		20100605	20100905	237.5
		20100605	20101206	396.5
		20100605	20110121	779.8
		20100721	20100905	222.5
		20100721	20101206	381.4
		20100721	20110121	764.7
		20100905	20101206	159.0
		20100905	20110121	542.3
		20101206	20110121	383.3
F580P174	83	20061207	20070609	-115.3
		20061207	20070909	416.8
		20061207	20071210	817.9
		20061207	20080125	1146.6

		20061207	20090614	-936.3
		20061207	20090914	-682.1
		20061207	20091215	-103.9
		20061207	20100317	736.8
		20061207	20100502	854.9
		20061207	20100617	897.0
		20061207	20100917	1030.1
		20061207	20101218	1512.5
		20070609	20070909	532.1
		20070609	20071210	933.2
		20070609	20080125	1261.9
		20070609	20090614	-821.0
		20070609	20090914	-566.8
		20070609	20091215	11.4
		20070609	20100317	852.1
		20070609	20100502	970.2
		20070609	20100617	1012.3
		20070609	20100917	1145.4
		20070609	20101218	1627.9
		20070909	20071210	401.1
		20070909	20080125	729.8
		20070909	20080426	1927.9
		20070909	20090614	-1353.1
		20070909	20090914	-1098.9
		20070909	20091215	-520.7
		20070909	20100317	320.0
		20070909	20100502	438.1
		20070909	20100617	480.1
		20070909	20100917	613.2
		20070909	20101218	1095.7
		20071210	20080125	328.7
		20071210	20080426	1526.8
		20071210	20090614	-1754.2
		20071210	20090914	-1500.0
		20071210	20091215	-921.8
		20071210	20100317	-81.1
		20071210	20100502	37.0
		20071210	20100617	79.1
		20071210	20100917	212.2
		20071210	20101218	694.6

		20080125	20080426	1198.1
		20080125	20090914	-1828.7
		20080125	20091215	-1250.5
		20080125	20100317	-409.8
		20080125	20100502	-291.7
		20080125	20100617	-249.7
		20080125	20100917	-116.6
		20080125	20101218	365.9
		20080426	20100317	-1607.9
		20080426	20100502	-1489.8
		20080426	20100617	-1447.7
		20080426	20100917	-1314.6
		20080426	20101218	-832.1
		20090614	20090914	254.2
		20090614	20091215	832.4
		20090614	20100317	1673.1
		20090614	20100502	1791.2
		20090614	20100617	1833.3
		20090614	20100917	1966.4
		20090914	20091215	578.2
		20090914	20100317	1418.9
		20090914	20100502	1537.0
		20090914	20100617	1579.1
		20090914	20100917	1712.2
		20091215	20100317	840.7
		20091215	20100502	958.8
		20091215	20100617	1000.9
		20091215	20100917	1134.0
		20091215	20101218	1616.5
		20100317	20100502	118.1
		20100317	20100617	160.2
		20100317	20100917	293.3
		20100317	20101218	775.7
		20100502	20100617	42.0
		20100502	20100917	175.1
		20100502	20101218	657.6
		20100617	20100917	133.1
		20100617	20101218	615.6
		20100917	20101218	482.5
F580P175	60	20061224	20070926	1624.2

		20061224	20071227	1941.6
		20061224	20080628	1022.8
		20061224	20081229	-300.6
		20061224	20090331	607.2
		20061224	20091001	1113.4
		20070926	20071227	317.4
		20070926	20080211	1189.2
		20070926	20080328	1196.4
		20070926	20080628	-601.4
		20070926	20081229	-1924.8
		20070926	20090331	-1017.0
		20070926	20091001	-510.8
		20070926	20100519	631.1
		20070926	20100704	898.1
		20070926	20101119	1060.3
		20070926	20110104	1473.4
		20071227	20080211	871.7
		20071227	20080328	879.0
		20071227	20080628	-918.8
		20071227	20090331	-1334.4
		20071227	20091001	-828.2
		20071227	20100519	313.7
		20071227	20100704	580.7
		20071227	20101119	742.9
		20071227	20110104	1156.0
		20080211	20080328	7.2
		20080211	20080628	-1790.6
		20080211	20091001	-1699.9
		20080211	20100519	-558.0
		20080211	20100704	-291.1
		20080211	20101119	-128.8
		20080211	20110104	284.3
		20080328	20080628	-1797.8
		20080328	20091001	-1707.2
		20080328	20100519	-565.3
		20080328	20100704	-298.3
		20080328	20101119	-136.1
		20080328	20110104	277.0
		20080628	20081229	-1323.4
		20080628	20090331	-415.6

		20080628	20091001	90.7
		20080628	20100519	1232.6
		20080628	20100704	1499.5
		20080628	20101119	1661.8
		20081229	20090331	907.8
		20081229	20091001	1414.1
		20090331	20091001	506.2
		20090331	20100519	1648.1
		20090331	20100704	1915.1
		20091001	20100519	1141.9
		20091001	20100704	1408.8
		20091001	20101119	1571.1
		20091001	20110104	1984.2
		20100519	20100704	266.9
		20100519	20101119	429.2
		20100519	20110104	842.3
		20100704	20101119	162.3
		20100704	20110104	575.3
		20101119	20110104	413.1
F580P176	46	20070713	20071013	618.9
		20070713	20080113	991.4
		20070713	20080414	1784.6
		20070713	20080530	1558.5
		20070713	20090115	-1439.2
		20070713	20100605	937.9
		20070713	20100721	953.9
		20070713	20100905	1179.4
		20070713	20101206	1346.8
		20070713	20110121	1735.2
		20071013	20080113	372.5
		20071013	20080414	1165.7
		20071013	20080530	939.6
		20071013	20100605	319.1
		20071013	20100721	335.0
		20071013	20100905	560.5
		20071013	20101206	727.9
		20071013	20110121	1116.3
		20080113	20080414	793.2
		20080113	20080530	567.1
		20080113	20100605	-53.4

		20080113	20100721	-37.4
		20080113	20100905	188.1
		20080113	20101206	355.4
		20080113	20110121	743.9
		20080414	20080530	-226.1
		20080414	20100605	-846.6
		20080414	20100721	-830.7
		20080414	20100905	-605.2
		20080414	20101206	-437.8
		20080414	20110121	-49.4
		20080530	20100605	-620.5
		20080530	20100721	-604.5
		20080530	20100905	-379.0
		20080530	20101206	-211.7
		20080530	20110121	176.8
		20100605	20100721	16.0
		20100605	20100905	241.5
		20100605	20101206	408.8
		20100605	20110121	797.3
		20100721	20100905	225.5
		20100721	20101206	392.8
		20100721	20110121	781.3
		20100905	20101206	167.3
		20100905	20110121	555.8
		20101206	20110121	388.5
F590P174	83	20061207	20070609	-95.0
		20061207	20070909	438.9
		20061207	20071210	847.9
		20061207	20080125	1182.6
		20061207	20090614	-928.2
		20061207	20090914	-668.8
		20061207	20091215	-85.4
		20061207	20100317	766.5
		20061207	20100502	888.1
		20061207	20100617	930.7
		20061207	20100917	1069.7
		20061207	20101218	1558.7
		20070609	20070909	533.8
		20070609	20071210	942.9
		20070609	20080125	1277.6

		20070609	20090614	-833.2
		20070609	20090914	-573.8
		20070609	20091215	9.6
		20070609	20100317	861.5
		20070609	20100502	983.1
		20070609	20100617	1025.7
		20070609	20100917	1164.7
		20070609	20101218	1653.6
		20070909	20071210	409.1
		20070909	20080125	743.8
		20070909	20080426	1949.1
		20070909	20090614	-1367.1
		20070909	20090914	-1107.6
		20070909	20091215	-524.2
		20070909	20100317	327.6
		20070909	20100502	449.3
		20070909	20100617	491.9
		20070909	20100917	630.9
		20070909	20101218	1119.8
		20071210	20080125	334.7
		20071210	20080426	1540.0
		20071210	20090614	-1776.1
		20071210	20090914	-1516.7
		20071210	20091215	-933.3
		20071210	20100317	-81.4
		20071210	20100502	40.2
		20071210	20100617	82.8
		20071210	20100917	221.8
		20071210	20101218	710.7
		20080125	20080426	1205.3
		20080125	20090914	-1851.4
		20080125	20091215	-1268.0
		20080125	20100317	-416.2
		20080125	20100502	-294.5
		20080125	20100617	-251.9
		20080125	20100917	-112.9
		20080125	20101218	376.0
		20080426	20100317	-1621.5
		20080426	20100502	-1499.8
		20080426	20100617	-1457.2

		20080426	20100917	-1318.2
		20080426	20101218	-829.3
		20090614	20090914	259.5
		20090614	20091215	842.9
		20090614	20100317	1694.7
		20090614	20100502	1816.4
		20090614	20100617	1858.9
		20090614	20100917	1998.0
		20090914	20091215	583.4
		20090914	20100317	1435.2
		20090914	20100502	1556.9
		20090914	20100617	1599.5
		20090914	20100917	1738.5
		20091215	20100317	851.8
		20091215	20100502	973.5
		20091215	20100617	1016.1
		20091215	20100917	1155.1
		20091215	20101218	1644.0
		20100317	20100502	121.7
		20100317	20100617	164.2
		20100317	20100917	303.3
		20100317	20101218	792.2
		20100502	20100617	42.6
		20100502	20100917	181.6
		20100502	20101218	670.5
		20100617	20100917	139.0
		20100617	20101218	627.9
		20100917	20101218	488.9
F590P175	71	20061224	20070511	1811.9
		20061224	20070926	1641.1
		20061224	20071227	1967.4
		20061224	20080628	1022.9
		20061224	20081229	-315.7
		20061224	20090331	603.2
		20061224	20091001	1117.7
		20070511	20070926	-170.8
		20070511	20071227	155.5
		20070511	20080211	1031.8
		20070511	20080328	1046.0
		20070511	20080628	-789.0

		20070511	20090331	-1208.7
		20070511	20091001	-694.3
		20070511	20100519	469.1
		20070511	20100704	735.4
		20070511	20101119	908.6
		20070511	20110104	1325.7
		20070926	20071227	326.3
		20070926	20080211	1202.6
		20070926	20080328	1216.8
		20070926	20080628	-618.1
		20070926	20081229	-1956.8
		20070926	20090331	-1037.9
		20070926	20091001	-523.4
		20070926	20100519	639.9
		20070926	20100704	906.2
		20070926	20101119	1079.4
		20070926	20110104	1496.6
		20071227	20080211	876.3
		20071227	20080328	890.5
		20071227	20080628	-944.5
		20071227	20090331	-1364.2
		20071227	20091001	-849.8
		20071227	20100519	313.6
		20071227	20100704	579.9
		20071227	20101119	753.1
		20071227	20110104	1170.2
		20080211	20080328	14.2
		20080211	20080628	-1820.8
		20080211	20091001	-1726.0
		20080211	20100519	-562.7
		20080211	20100704	-296.4
		20080211	20101119	-123.2
		20080211	20110104	294.0
		20080328	20080628	-1834.9
		20080328	20091001	-1740.2
		20080328	20100519	-576.9
		20080328	20100704	-310.5
		20080328	20101119	-137.4
		20080328	20110104	279.8
		20080628	20081229	-1338.6

		20080628	20090331	-419.7
		20080628	20091001	94.7
		20080628	20100519	1258.0
		20080628	20100704	1524.4
		20080628	20101119	1697.5
		20081229	20090331	918.9
		20081229	20091001	1433.3
		20090331	20091001	514.5
		20090331	20100519	1677.8
		20090331	20100704	1944.1
		20091001	20100519	1163.3
		20091001	20100704	1429.7
		20091001	20101119	1602.8
		20100519	20100704	266.4
		20100519	20101119	439.5
		20100519	20110104	856.7
		20100704	20101119	173.1
		20100704	20110104	590.3
		20101119	20110104	417.2

Table S3: Dates of Sentinel1-A/B C-band SAR images used for estimating pre-cyclone vertical land motion, as well as flood mapping via a flood-free reference SAR amplitude image and post-cyclone amplitude image.

Year	Month	Date
20151221	2015	12
20160114	2016	1
20160126	2016	1
20160326	2016	3
20160419	2016	4
20160630	2016	6
20160712	2016	7
20160724	2016	7
20160928	2016	9
20161004	2016	10
20161016	2016	10
20161022	2016	10
20161103	2016	11
20161109	2016	11
20161203	2016	12
20161215	2016	12
20161221	2016	12
20170108	2017	1
20170114	2017	1
20170213	2017	2
20170219	2017	2
20170225	2017	2
20170303	2017	3

Year	Month	Date
20170315	2017	3
20170321	2017	3
20170327	2017	3
20170402	2017	4
20170408	2017	4
20170420	2017	4
20170426	2017	4
20170502	2017	5
20170508	2017	5
20170526	2017	5
20170607	2017	6
20170613	2017	6
20170619	2017	6
20170625	2017	6
20170701	2017	7
20170713	2017	7
20170725	2017	7
20170806	2017	8
20170812	2017	8
20170818	2017	8
20170824	2017	8
20170830	2017	8